

Comparison of generative algorithms for conceptual groundwater modeling of coastal volcanic aquifer features with disparate, sparse and extremely imbalanced data

Michael J. Friedel^{1,2,3}

¹ Department of Physics, University of Colorado – Denver, USA

² Earthquest Consulting Ltd, Auckland, NZ

³ Semeion Institute, Rome, IT

michael.friedel@ucdenver.edu

ABSTRACT

In coastal volcanic aquifers, the reliability of freshwater–seawater exchange simulations are governed by accuracy of the conceptual groundwater model (CGM). Traditional CGMs are constructed by qualitatively combining independent hydrogeophysical features, limiting their ability to capture the complexity of volcanic terrains. To integrate these disparate, sparse, and imbalanced features, we propose an AI-assisted workflow. First, the self-organizing map (SOM) is applied to estimate a deterministic set of transdisciplinary features called the *reference model*. Second, generative algorithms are applied to the reference model and empirical distributions constructed to obtain sets of stochastic point clouds called the *site model*. Data quality metrics identify the preferred generative algorithm whose set of stochastic features are mapped using SOM to the groundwater model grid and assigned as the *stochastic CGM*. The proposed algorithm is applied to extremely imbalanced multiclass features and multiple discrete numerical features observed at the Hālawa-Moanalua (H-M) aquifer, O’ahu, Hawai’i. At this stie, the Copula Generative Adversarial Network is deemed as the preferred generative algorithm whose set of stochastic transdisciplinary features represent the H-M CGM. The simulated spatial geologic units correspond to published surface maps; and the simulated conductance, temperature, and barometric pressure profiles correlate with those measured at deep monitoring wells. Inspecting the 3D conductance models reveal groundwater flow and discharge driven by the aquifer’s hydraulic gradient, freshwater pumping, seawater intrusion induced by onshore withdrawals, and preferred pathways for freshwater–seawater exchange, such as landward intrusion of seawater and seaward discharge of freshwater.

Keywords: Conditional tabular generative adversarial network - CTGAN, Copula generative adversarial network – CopulaGAN, Extremely-imbalanced data, Tabular Gaussian copula – TGC, Tabular variational autoencoder - TVAE, Transdisciplinary reference model, Stochastic transdisciplinary conceptual groundwater model.

Highlights

- AI-assisted CGM integrates sparse and highly imbalanced hydrogeophysical data.
- SOM and generative AI resolve complexity in coastal volcanic aquifers.
- CopulaGAN is statistically preferred for stochastic CGM development.
- 3D models reproduce surface geology and deep monitoring well feature profiles.
- Models reveal freshwater–seawater exchange and intrusion pathways.

1. Introduction

Volcanic islands are critical sources of freshwater for millions of people, yet their complex geology and topography pose significant challenges for groundwater exploration and management (Jenson et al., 2006; Gingerich and Engott, 2012; White et al., 2020). Freshwater in these environments is often stored in highly heterogeneous aquifers, including perched layers, basal lenses, and dike-impounded reservoirs, which are strongly influenced by lava flows, fractures, and volcanic structures (Stearns and Macdonald, 1946; Hunt, 1996; Thomas et al., 2019). Understanding the structure, storage, and dynamics of these aquifers is essential for sustainable water supply, especially in the context of climate change, sea-level rise, and increasing water demand across the Pacific region (Oki, 2004; Terry and Falkland, 2010; Rotzoll and Fletcher, 2013). Despite their importance, volcanic aquifers remain poorly characterized in many island settings due to the limited availability of subsurface data and the high variability of volcanic terrain (Custodio, 2010; Violette et al., 2012; Ingebritsen et al., 2015).

Traditionally, volcanic aquifer studies rely on borehole data, spring discharge measurements, and basic hydrological modeling to infer aquifer geometry, recharge rates, and freshwater–saltwater distribution (Stearns & Macdonald, 1946; Hunt, 1996; Custodio, 2010; Ahmed et al., 2018). While these approaches provide foundational insights, they are spatially limited and often unable to resolve the complex internal structure of volcanic formations (Thomas et al., 2019). Over the past couple decades, the application of geophysical methods transforms how to investigate and conceptualize volcanic aquifers (Violette et al., 2012; Baud et al., 2025). Common surface geophysical methods include time-domain electromagnetic (Alshehri and Abdelrahman, 2022; Carrasco-García et al., 2022), magnetotelluric (Hogg et al., 2018; Liu et al., 2022; Isaia et al., 2025), and magnetic resonance sounding (Legchenko et al., 2019).

Other researchers combine geophysical methods with the aim of reducing ambiguities in conceptual models of volcanic aquifers. Examples include combining electrical resistivity tomography and self-potential (Revil et al., 2008), airborne electromagnetic and magnetic data (Dumont et al., 2021), and electrical resistivity tomography and gravity (Khattach et al., 2025). Despite the growing number of geophysical studies in volcanic rock, few studies attempt to conceptualize subsurface systems from the mountains to the sea (Billy et al., 2022). Recently, Miller and Tontini (2025) developed a land-to-sea volcanic facies model by spatial clustering of density, susceptibility, and resistivity models derived through separate gravity, magnetic and airborne electromagnetic inversions.

In Hawai'i, sparse borehole sampling and disparate surface geophysical investigations infer the structural and hydrological complexity of volcanic aquifers. Geophysical methods, such as gravity, electrical resistivity, electromagnetic, magnetic, and seismic methods, identify dike-impounded groundwater systems, perched aquifers, and extensive basal freshwater lenses (Zohdy and Jackson, 1969; Gingerich and Engott, 2012; Izuka et al., 2015; Izuka et al., 2018; Thomas et al., 2019; Izuka and Rotzoll, 2023). On Hawai'i Island, marine controlled source electromagnetic and seismic studies reveal freshwater that extends offshore beneath the seafloor, possibly forming submarine groundwater reservoirs (Attias, et al., 2020). Other geophysical studies on the east side of Hawai'i Island use induced polarization measurements to determine surface temperature at the Kilauea shield volcano (Revil et al., 2021), and magnetotelluric measurements to image Kilauea's internal structure in terms of electrical resistivity (Hoversten et al., 2022).

On the island of O'ahu, surface geophysical studies are undertaken to conceptualize subsurface structures that may control flow through volcanic rocks in subregional aquifers at the Kaiwi Coastal and

Hālawa-Moanalua areas. In the Kaiwi coastal area, seismic ambient noise surface wave tomography and self-potential results are independently used to infer groundwater flow in paleo-channels and along ridges of the basaltic bedrock (Grobbe et al., 2021). These qualitative inferences are nonunique and uncertain given the lack of direct borehole and/or water well information available to constrain their interpretation. In the Red Hill area, the subregional Hālawa-Moanalua aquifer spans the region from the upland dike complex (Walker, 1986) to low lands at the Pacific Ocean. In the central part of this aquifer, the seismic (Liberty and St. Clair, 2018) and gravity (Ito et al., 2019) survey results describe a plausible, albeit deterministic, and qualitative structural framework that infers the possible direction of groundwater flow. In this part of the aquifer, there also are borehole hydrogeologic observations (e.g., geology, water levels, and water quality) available to potentially constrain conceptualization of this volcanic aquifer. Given the disparate, sparse and imbalanced nature of this multidisciplinary data set, the traditional independent (visual) approach for feature integration is impractical and fraught with technical challenges, such as how to produce an unbiased model, estimate aquifer features and their uncertainty at nodes across a numerical groundwater model grid.

The lower third of the Hālawa–Moanalua aquifer reflects the coastal system and therefore may be hydraulically connected to secondary high-permeability pahoehoe layers with preferential flowpaths influenced by the Pacific Ocean, as on Hawai‘i Island (Geng and Michael, 2020). Aquifer heterogeneity and preferential flow pathways are known to increase the risk of freshwater contamination (Geng and Michael, 2021), as spatial variability in hydraulic conductivity govern seawater intrusion by altering the freshwater–seawater interface through mixing and spreading (Adams and Gelhar, 1992; Dentz et al., 2011). Numerical groundwater models demonstrate that connected heterogeneities can generate complex offshore salinity patterns and enhance seawater intrusion under pumping (Siena and Riva, 2018; Yu and Michael, 2019). In fractured volcanic aquifers, highly permeable conduits, such as those in pahoehoe lava flows, may serve as preferential pathways that exacerbate seawater intrusion threatening freshwater resources (Bonacci and Roje-Bonacci, 1997; Xu et al., 2016). Three-dimensional numerical simulations reveal that conduit geometry and connectivity can strongly influence the extent and variability of seawater intrusion, underscoring the need to represent 3D heterogeneity and preferential flowpaths in coastal groundwater models. Fully resolving these processes in 3D models, however, remains challenging. Primary challenges include poorly resolved conceptual groundwater models, and numerical models that are computationally expensive and prone to numerical instability (Yu and Michael, 2019).

Current trends in Earth, energy and environmental studies use artificial intelligence (AI) to inform problem-solving and decision-making. AI applications in groundwater hydrology include data-driven machine learning, physics-informed machine learning, and multimodal machine learning. Data driven machine learning largely focuses on supervised machine learning methods to map and forecast groundwater levels, as reviewed by De Salvo et al. 2022. Physics-informed machine learning brings together supervised data driven machine learning with differential equations to forecast space-time groundwater flow and/or transport (Yeung et al., 2022; Friedel and Buscema, 2023; Adombi et al., 2024). Multimodal machine learning affords the possibility to incorporate any number of categorical and numerically derived values along with point field measurements to inform the CGM. These features can be derived using numerical model calibrations/inversions, supervised and unsupervised data-driven, physics-informed, and deep learning approaches. Recent work by University of Hawai‘i researchers demonstrates the applicability of multimodal machine learning for developing a CGM reflecting groundwater-geothermal interaction and their features across Lanai and Hawai‘i Islands (Friedel et al., 2023).

The aim of this study is to develop and evaluate an AI-assisted workflow for developing CGMs of island volcanic aquifers. This study addresses the research question: Can generative statistical and/or generative AI algorithms be used to characterize Pacific volcanic groundwater system features using disparate, sparse and extremely imbalanced data? Answering this question is important given that the quality of a numerical groundwater model is limited by adequacy of the CGM. To answer this question, we hypothesize that mutual information (Shannon, 1948) among hydrogeophysical (geologic, geophysical, engineering, and water quality) observations can be computationally assimilated and used to produce a valid stochastic transdisciplinary set of aquifer features representing the CGM. In testing this hypothesis, an AI-assisted workflow is proposed for application to volcanic aquifers. The AI-assisted workflow is tested to achieve three objectives at the sub-regional Hālawa-Moanalua (H–M) aquifer on O‘ahu, Hawai‘i: (1) compare performance of the unsupervised machine learning to provide deterministic estimates of transdisciplinary features; (2) compare performance of the different generative algorithms in predicting alternate transdisciplinary feature sets; and (3) use the preferred generative algorithm to quantify, map, and interpret the 3D stochastic distribution of geological, geophysical, engineering, and water-quality features. This study extends the work of Friedel et al. (2023), who developed a deterministic transdisciplinary data-driven model of freshwater-geothermal system features at selected locations in actual and synthetic boreholes on Lanai and Hawai‘i Islands. This study also expands the work of researchers who applied the Gaussian Copula to generate groundwater quality parameters for training a deep neural network for estimation and uncertainty analysis of a coastal aquifer experiencing seawater intrusion (Taşan et al., 2023; Zhang et al., 2024).

2. Methods

The reliability of freshwater–seawater exchange simulations are governed by accuracy of the conceptual groundwater model (CGM). Traditional CGMs are constructed by qualitatively combining independent hydrogeophysical features, limiting their ability to capture the complexity of volcanic aquifers. Integrating features using this ad-hoc approach is difficult because categorical and numerical observations oftentimes are disparate, sparse, skewed, and extremely imbalanced. To overcome these limitations, we propose the following quantitative AI-assisted workflow: the Data cube, the Reference Model, the Site Model, and the Conceptual Groundwater Model (Fig. 1). Each of these steps are briefly described next.

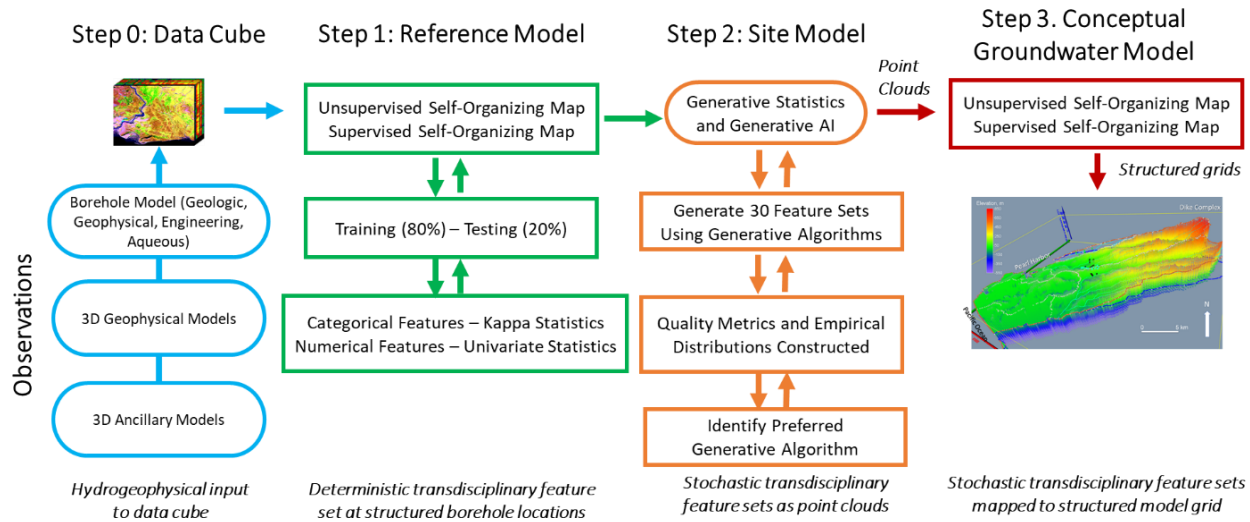


Fig. 1. Proposed AI-assisted workflow to improve reliability of Conceptual Groundwater Models across Pacific Island volcanic aquifers.

2.1. Data cube

Development of the AI-assisted workflow begins with selecting a Pacific Island volcanic aquifer where diverse hydrogeophysical observations exist and/or will be gathered. To enable system-wide analysis, all of the available and future observations are compiled into an unstructured data cube. The data cube provides a unified framework for aggregating categorical and numerical features across spatial location, depth, and data type. This structured framework supports the joint analysis of direct and indirect observations.

Direct observations can include physical, chemical, and physicochemical measurements collected from wells, boreholes, and ocean stations. Indirect observations are derived primarily from geophysical methods—such as electrical resistivity, electromagnetic, gravity, and seismic surveys—as well as drilling-based interpretations, equations, and published datasets. These hydrogeophysical observations can be represented as categorical (discrete) and numerical (continuous) features distributed across heterogeneous and unstructured grid nodes. Integration across data sources is achieved through self-organization of mutual information (Shannon, 1948; Kraskov et al., 2004) in hydrogeophysical features.

Categorical features may include geologic units, aquifer confinement, and open-ocean. These variables will be identified using one-hot encoding (present = 1, absent = 0, unknown = blank), converting categorical labels into a numerical format suitable for machine learning (Google Developers, 2025). Continuous features consist of both direct measurements and indirectly derived parameter estimates, including geophysical properties and engineering metrics. All categorical and continuous variables incorporated into the data cube are treated as soft priors, with uncertainty evaluated during generative AI-based inference through shared information among reference model features (Kraskov et al., 2004). The combined dataset may exhibit class imbalance in geologic units and spatial skewness in numerical variables due to uneven sampling and heterogeneous hydrogeologic conditions. To mitigate these effects, preprocessing steps will include sample augmentation and logarithmic transformation of selected numerical variables, providing the foundation for the information-driven generative modeling framework described in the following section.

2.2. Reference model

2.2.1 Self organizing map

The reference model is constructed using a two-stage self-organizing map (SOM) framework that combines unsupervised pattern discovery with supervised estimation of aquifer features. SOMs are neural network-based, unsupervised learning algorithms that project high-dimensional data onto a low-dimensional (typically two-dimensional) lattice while preserving the topological relationships of the input space (Kohonen, 2001, 2013). This property makes SOMs well suited for exploratory analysis and dimensionality reduction of complex hydrogeological datasets, where nonlinear dependencies and multivariate correlations are common.

In the first stage, an unsupervised SOM is trained to learn the intrinsic structure of the multivariate aquifer data extracted from the data cube (after Friedel et al., 2020). Training follows a competitive learning procedure in which input vectors are iteratively presented to the network and mapped to the

best-matching unit (BMU), defined as the node whose weight vector minimizes the Euclidean distance to the input vector,

$$D = \sqrt{\sum_{i=0}^N (V_i - W_i)^2}$$

where \mathbf{V} is the input vector and \mathbf{W} is the weight vector. A neighborhood of nodes surrounding the BMU is identified using a Gaussian kernel with a time-dependent radius,

$$\sigma = \sigma_0 \exp\left(-\frac{1}{\lambda}\right), t = 1, 2, 3, \dots,$$

where σ_0 is radius at t_0 , λ is a decay constant, and t denotes the iteration. The weights of the BMU and its neighbors are updated according to

$$\mathbf{W}(t+1) = \mathbf{W}(t) + L(t)(\mathbf{V}(t) - \mathbf{W}(t)),$$

where the learning rate $L(t) = L_0 \exp\left(-\frac{1}{\lambda}\right)$, $t = 1, 2, 3, \dots$, decays exponentially over time, and the neighborhood influence function is given by

$$\Theta(t) = \exp\left(-\frac{dist^2}{2\sigma^2(t)}\right), t = 1, 2, 3, \dots,$$

Here, $dist$ denotes the distance between a node and the BMU on the SOM grid. Competitive training proceeds iteratively until changes in the weight vectors converge, yielding a topologically ordered representation of the aquifer feature space.

In the second stage, a supervised SOM is applied to associate the trained SOM nodes with target variables representing aquifer properties of interest (Riese et al., 2020). Continuous variables are predicted using node-based regression, while categorical variables are assigned probabilistic class memberships based on the distribution of labeled samples mapped to each node. The combined regression and classification outputs define a deterministic, data-driven reference model that captures the dominant multivariate structure of the aquifer system and serves as a baseline for subsequent uncertainty quantification and synthetic data generation analyses.

2.2.2. Training and testing

Model training and evaluation are conducted using k-fold cross-validation (Hastie et al., 2009), in which the dataset is randomly shuffled and divided into training (typically 80%) and testing (20%) subsets that are repeated N times for assessing model generalizability to independent field data. Model performance is evaluated using metrics appropriate for continuous and categorical features, e.g., the coefficient of determination (R^2) and mean squared error (MSE) for continuous variables, and overall accuracy and Cohen's kappa statistic (Cohen, 1960) for categorical variables. In k-fold cross-validation, the dataset is partitioned into k equal subsets, with the model trained on $k - 1$ folds and validated on the remaining fold, repeated until each fold is used once for validation, and performance metrics averaged to reduce bias and maximize data use. Cohen's kappa measures agreement beyond chance and is interpreted as ≤ 0 (no agreement), 0.01–0.20 (none to slight), 0.21–0.40 (fair), 0.41–0.60 (moderate), 0.61–0.80 (substantial), and 0.81–1.00 (almost perfect), providing a robust assessment of classification reliability in ML-based digital geologic mapping.

2.2.3. Grouping features

Statistically meaningful feature grouping of self-organized information is performed through k-means clustering (Vesanto and Alhoniemi, 2000) applied to the SOM codebook vectors across the trained network. Optimal partitioning for each candidate number of clusters is determined using the Euclidean distance criterion, with cluster validity evaluated using the Davies–Bouldin index (Davies and

Bouldin, 1979). To reduce sensitivity to local minima, the k-means algorithm is repeated multiple times for each clustering configuration. Although the Davies–Bouldin index is used here for convenience, other cluster validity measures could be applied. The final reference model is constructed by retraining the SOM with optimized parameters using the complete dataset (combined training and testing observations) from the data cube.

2.3 Site model

2.3.1. Synthetic data generation methods

The *site model* is constructed through application of synthetic data generation methods to the reference model. Synthetic data generation is employed to produce stochastic ensembles of transdisciplinary aquifer features for use in conceptual groundwater modeling and uncertainty quantification. Four complementary methods are evaluated representing a range of statistical assumptions and modeling capacities: a Tabular Gaussian Copula (TGC), a Tabular Variational Autoencoder (TVAE), a Conditional Tabular Generative Adversarial Network (CTGAN), and a Copula Generative Adversarial Network (CopulaGAN). These approaches span classical statistical, variational, and adversarial learning frameworks, each offering distinct trade-offs in interpretability, computational efficiency, and ability to capture complex dependencies in heterogeneous hydrogeological datasets.

The TGC models the joint distribution of a multivariate dataset by separating marginal behavior from dependence structure (Nelsen, 2006). Each variable X_j is transformed to uniform space using its marginal cumulative distribution function (CDF), $U_j = F_j(X_j)$, and mapped to a Gaussian latent space via $Z_j = \Phi^{-1}(U_j)$, where Φ^{-1} is the inverse standard normal CDF. Dependence is captured through a correlation matrix Σ estimated from $\mathbf{Z} \sim \mathcal{N}(0, \Sigma)$, and synthetic samples are generated by sampling $\mathbf{Z}^* \sim \mathcal{N}(0, \Sigma)$ and applying inverse marginal transformations $X_j^* = F_j^{-1}(\Phi(Z_j^*))$. This approach is computationally efficient and transparent, making it well suited for baseline uncertainty characterization, though it is limited to linear dependence structures.

The TVAE extends variational autoencoders to mixed continuous–categorical tabular data by learning a probabilistic latent representation through an encoder–decoder architecture (Kingma and Welling, 2014; Xu et al., 2019). The encoder defines an approximate posterior $q_\phi(\mathbf{z} \mid \mathbf{x}) = \mathcal{N}(\mu_\phi(\mathbf{x}), \text{diag}(\sigma_\phi^2(\mathbf{x})))$, while the decoder models $p_\theta(\mathbf{x} \mid \mathbf{z})$ using variable-specific likelihoods. Model training maximizes the evidence lower bound,

$$\mathcal{L}_{ELBO} = \mathbb{E}_{q_\phi(\mathbf{z} \mid \mathbf{x})} [\log p_\theta(\mathbf{x} \mid \mathbf{z})] - KL(q_\phi(\mathbf{z} \mid \mathbf{x}) \parallel p(\mathbf{z})),$$

with $p(\mathbf{z}) = \mathcal{N}(0, I)$. TVAE enables modeling of nonlinear multivariate relationships but may struggle with rare events and sharp distributional features.

The CTGAN addresses limitations of conventional GANs for tabular data by introducing conditional sampling and specialized preprocessing for mixed data types and imbalanced categories (Goodfellow et al., 2014; Xu et al., 2019). The generator produces synthetic samples conditioned on a categorical vector \mathbf{c} , $\mathbf{x}^* = G_\theta(\mathbf{z}, \mathbf{c})$, where $\mathbf{z} \sim \mathcal{N}(0, I)$. Training commonly adopts a Wasserstein GAN with gradient penalty (WGAN-GP), with discriminator loss

$$\mathcal{L}_D = \mathbb{E}_{\mathbf{x} \sim p_{data}} [D_\phi(\mathbf{x}, \mathbf{c})] - \mathbb{E}_{\tilde{\mathbf{x}} \sim p_G} [D_\phi(\tilde{\mathbf{x}}, \mathbf{c})] + \lambda \mathbb{E}_{\hat{\mathbf{x}}} [\|\nabla_{\hat{\mathbf{x}}} D_\phi(\hat{\mathbf{x}}, \mathbf{c})\|_2 - 1]^2,$$

and generator loss $\mathcal{L}_G = -\mathbb{E}_{\tilde{\mathbf{x}} \sim p_G} [D_\phi(\tilde{\mathbf{x}}, \mathbf{c})]$. CTGAN is well suited for large, heterogeneous datasets but is computationally intensive and sensitive to hyperparameter choices.

The CopulaGAN combines copula-based marginal transformation with adversarial learning in copula space to preserve marginal distributions while learning nonlinear dependence structures (Torbenson et al., 2020). Observations are first mapped to copula space via $u_j = F_j(x_j)$, and a GAN is trained to generate synthetic copula samples $\tilde{\mathbf{u}} = G_\theta(\mathbf{z})$. These samples are mapped back to the original data space using inverse marginals, $x_j^* = F_j^{-1}(\tilde{u}_j)$. This hybrid approach improves marginal fidelity and training stability relative to raw GANs, though it remains less mature than alternative tabular methods.

The comparison of these four generative methods is motivated by the need to support data assimilation and uncertainty quantification in groundwater modeling, where accurate representation of subsurface variability and inter-parameter dependence strongly influences predictive uncertainty. Copula-based models provide statistically grounded baselines for uncertainty propagation, while variational and adversarial models offer greater flexibility for capturing nonlinear hydrogeological relationships. Evaluating multiple generative paradigms allows assessment of how structural modeling assumptions affect stochastic aquifer feature ensembles, reducing reliance on a single representation of subsurface heterogeneity and strengthening the robustness of uncertainty estimates in subsequent groundwater simulations.

2.3.2. Validation of tabular generative algorithms

The performance of synthetic data generation models is evaluated using the standardized, model-agnostic metric framework provided by the Synthetic Data Vault (SDV), which enables consistent comparison of generative algorithms based on statistical fidelity and preservation of multivariate dependencies (Patki et al., 2016). These quality metrics quantify similarity between real and synthetic data by comparing univariate distributions—using nonparametric measures such as the Kolmogorov–Smirnov (KS) statistic for continuous variables and total variation distance for categorical variables—and by assessing the preservation of pairwise relationships between variables. These metrics are well suited to groundwater modeling studies affected by seawater intrusion, where maintaining realistic concentration distributions and dependencies among salinity, major ions, and hydrochemical indicators is critical. Unlike GAN-specific or low-dimensional goodness-of-fit metrics, the SDV metrics scale efficiently to high-dimensional datasets and support transparent, reproducible evaluation across statistical, machine-learning, and deep-learning models, consistent with established hydrological practice (Wilcox, 2017; Arndt et al., 2020).

The SDV framework organizes evaluation metrics into different types: Diagnostic, Quality, and Privacy. Diagnostic metrics verify data validity and structural integrity by checking data types, value ranges, categorical levels, table structure, and completeness, helping to identify invalid or failed synthetic outputs. Quality metrics form the primary basis for model comparison and measure both column-level distribution similarity and the preservation of relationships between variable pairs, including numerical, categorical, and mixed-variable interactions. These metrics are normalized between 0 and 1 and aggregated into an overall Quality Score. The SDV framework does not, by default, include downstream predictive performance metrics, domain-specific physical constraints, or coverage diagnostics; such measures must be defined separately when required. In this study, generative models

are compared primarily using SDV Quality Scores, while privacy metrics are reported independently and are not used for ranking herein.

To evaluate the fidelity of synthetic tabular datasets generated using TGC, TVAE, CTGAN, and CopulaGAN models, the KS Complement metric is employed to quantify agreement between the marginal distributions of real and synthetic variables (Dankar, et al., 2025). The metric is derived from the Kolmogorov–Smirnov (KS) statistic, which measures the maximum absolute difference between the empirical cumulative distribution functions (CDFs) of observed data $F_{\text{obs}}(x)$ and synthetic data $F_{\text{syn}}(x)$, defined as $KS = \sup_x |F_{\text{obs}}(x) - F_{\text{syn}}(x)|$. The KS Complement is computed as $1 - KS$, yielding a normalized similarity score ranging from 0 to 1, with higher values indicating closer correspondence between observed and synthetic distributions. This transformation facilitates direct comparison across models and variables.

The KS Complement is calculated for each continuous hydrological variable independently and subsequently aggregated across variables to provide an overall measure of distributional fidelity. As a non-parametric statistic, the metric does not impose assumptions on the underlying data distributions and is therefore well suited for the heterogeneous and often non-Gaussian characteristics of hydrological variables. However, because the KS statistic evaluates marginal distributions only and does not capture inter-variable dependence structures, it is interpreted alongside complementary metrics assessing correlation preservation and multivariate dependence to provide a comprehensive evaluation of synthetic data quality.

3. Results and discussion

3.1 Data cube

The first step in building an AI-assisted conceptual groundwater model (CGM) involves the selection of a study site from where geologic, geophysical, engineering, and water quality (referred to as hydrogeophysical) observations can be acquired and aggregated into the data cube. For this purpose, the Hālawa–Moanalua (H-M) sub-regional aquifer on the island of O’ahu, Hawai’i, is selected (Fig. 2). The H-M aquifer spans six surface catchments: Aiea (5.30 km²), Hālawa (25.4 km²), Moanalua (27.2 km²), Salt Lake (19.0 km²), unnamed catchment #33030 (11.4 km²), and unnamed catchment #34030 (6.14 km²). This aquifer is bounded to the north by the upland dike complex (Walker, 1986) and to the south by the Pacific Ocean. The lower third of the study area is bounded by Pearl Harbor to the west, the Pacific Ocean to the south, and an unnamed harbor to the east (referred hereafter as the East Harbor). Under these conditions, precipitation entering at the dike complex is hypothesized to flow under hydraulic gradient toward the Pacific Ocean.

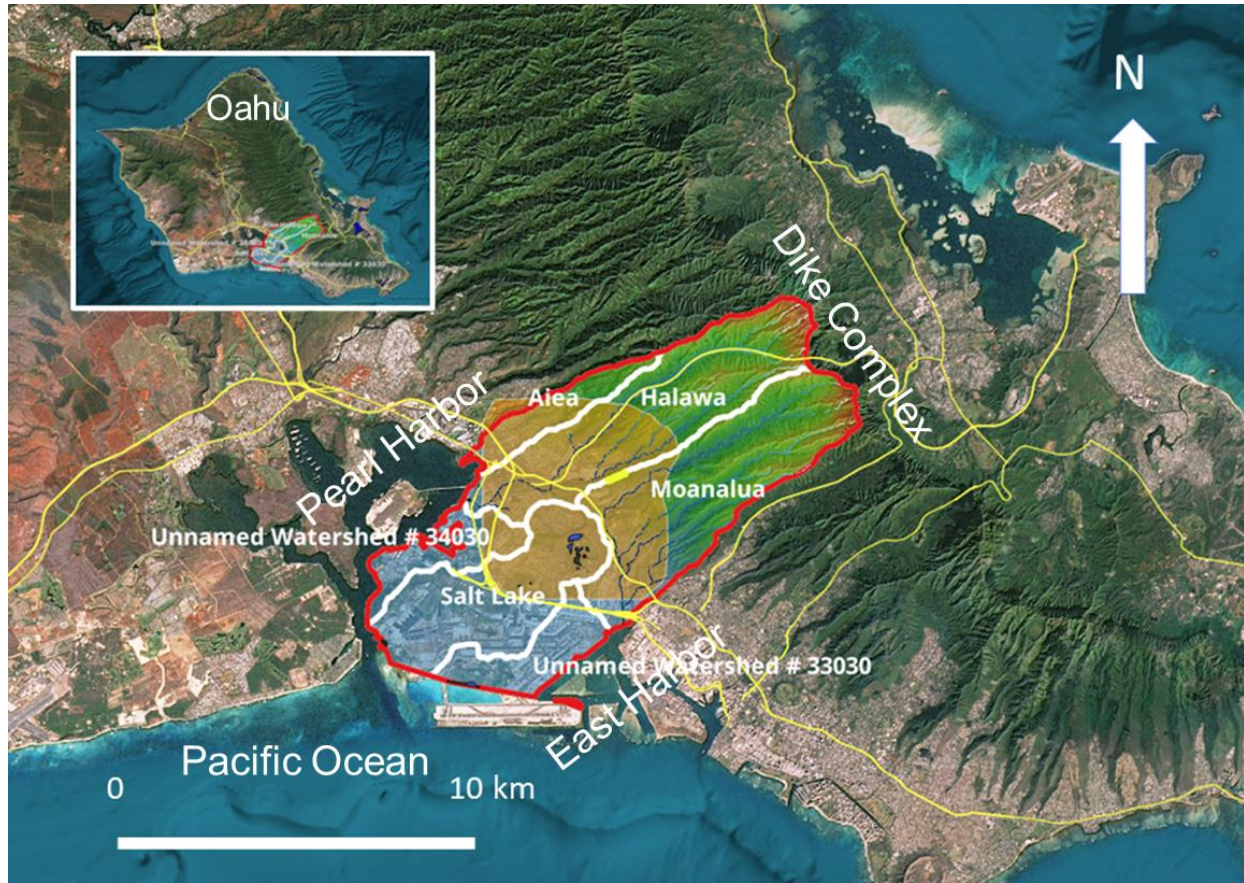


Fig. 2. Map of the study area, O'ahu Hawai'i (inset), and primary catchments (outlined in white) overlying the Hālawa-Moanalua aquifer (outlined in red). Primary catchment areas are: Aiea (5.30 km^2), Hālawa (25.4 km^2), Moanalua (27.2 km^2), Salt Lake (19.0 km^2), unnamed #33030 (11.4 km^2), and unnamed #34030 (6.14 km^2).

Key datasets include borehole logs from Naval Facilities (NavFac, 2018–2021), water wells (Lautze, 2014a, b), deep monitoring wells and water supply wells (Board of Water Supply, 2023; U.S. Geological Survey, 2023), water quality wells (Lautze et al., 2014a, b; Lautze, 2017), harbor seawater profile nodes surrounding the aquifer (Lenntech, 2023; PacIOOS, 2023; PetroWiki, 2023), and synthetic wells generated as part of this study. A reference map summarizing the locations and observation types used to populate the data cube is shown in Fig. 3. Feature assignments integrate multiple complementary data sources, including direct borehole observations (NavFac, 2018–2021), seismic refraction and reflection data delineating subsurface contacts (Liberty and St. Clair, 2018), drilling depths to the caprock–pāhoehoe interface (Hunt, 1997), published surface geologic maps with unit elevations (Sherrod et al., 2021), harbor profile nodes (PacIOOS, 2023), deep well records (Board of Water Supply, 2023), and the synthetic wells developed herein. These key datasets comprise categorical and continuous features described next.

3.1.1. Categorical features

Categorical features, including geologic units ('a'ā, alluvium, caprock, loose and welded clinkers, pāhoehoe, saprolite, and tuff), aquifer confinement (confined, unconfined), and open-ocean (yes, no), are represented using one-hot encoding (Google Developers, 2025). Example categorical encodings presented below include: geologic units (positions 1-8), aquifer confinement (position 9), and open ocean (position 10).

- 'a'ā, confined aquifer, no ocean → [1,0,0,0,0,0,0,1,0]
- alluvium, confined aquifer, no ocean → [0,1,0,0,0,0,0,1,0]
- caprock, confined aquifer, no ocean → [0,0,1,0,0,0,0,1,0]
- clinker loose, unconfined aquifer, no ocean → [0,0,0,1,0,0,0,0,0]
- clinker welded, confined aquifer, no ocean → [0,0,0,0,1,0,0,1,0]
- saprolite, confined aquifer, no ocean → [0,0,0,0,1,0,0,1,0]
- pāhoehoe, confined aquifer, no ocean → [0,0,0,0,0,1,0,1,0]
- tuff, unknown confinement, no ocean → [0,0,0,0,0,0,1, ,0]
- unknown, unknown confinement, no ocean → [, , , , , , ,0]

Other geologic units also are identified indirectly from velocity measurements derived from seismic refraction surveys (Liberty and St. Clair, 2018), which are translated into lithologic units using published velocity ranges summarized in Table 1. Where multiple velocities correspond to a single unit, median values are used. To improve spatial coverage and support data-driven inference, synthetic wells lacking assigned features (empty cells) are incorporated as placeholders within the Data Cube. These synthetic wells are distributed throughout the aquifer (white circles; Fig. 3) to depths of 600 m, with higher densities near key structural features north of the tuff cone and along seismic survey lines.

Table 1.

P-wave velocity values used for assigning geologic units for incorporation into the Reference Model.

Geology		Velocity, m/s					References
Type	Unit	Minimum	Median	Maximum	Comment		
Alluvium	alluvium	0	1000		Unconsolidated sediment deposited		Von Voigtlander et al., 2017
	caprock	3000	3100	3200	Marine and terrestrial sediments		Von Voigtlander et al., 2017; Souza and Voss, 1987
	pāhoehoe	>3400	5000	<=5300	Lava flow		Bücker, 1999; Von Voigtlander et al., 2017
	aa	>5500	5750	<6000	lava flow		Brandes et al., 2011; Von Voigtlander et al., 2017
	clinker (loose)	>1900	2175	2450	lava flow		Brandes et al., 2011; Von Voigtlander et al., 2017
	clinker (welded)	2450	2850	<=3000	lava flow		Visher and Mink, 1964; Von Voigtlander et al., 2017
Basalt	saprolite	>=1000	1450	<=1900	Weathered in-place		Miller, 1988; Von Voigtlander et al., 2017
	tuff	>3000	3000	<=3400	volcanic ash and debris		Keller, 1960; Finstick, 1999; Von Voigtlander et al., 2017
Volcanic							

Vertical assignment of geologic units follows a set of systematic rules. Saprolite is assigned to nodes extending 3 m above the saprolite–pāhoehoe contact, while pāhoehoe is assigned to nodes extending 3 m below this contact. Caprock is assigned from the caprock–pāhoehoe contact upward to the land surface, and pāhoehoe is assigned downward from this contact to the base of the model. These assignments assume undifferentiated caprock, saprolite, and pāhoehoe units. Surface occurrences of alluvium and tuff are assigned based on published geologic maps. A summary of categorical feature counts is provided in Table 2.

Categorical observations—including feature type, name, and Data Cube reference—are listed in Table 3. Examination of total counts and fractional representation reveals an extremely imbalanced dataset. For example, saprolite and pāhoehoe together account for more than half of all observations (saprolite: $n = 25,310$, 33%; pāhoehoe: $n = 13,295$, 18%), whereas several units are sparsely represented,

including welded clinker ($n = 2,507$, 3%), ‘a’ā ($n = 2,580$, 3%), tuff ($n = 3,082$, 4%), and ocean ($n = 28$, <0.1%). Caprock ($n = 3,802$, 5%) and alluvium ($n = 12,083$, 16%) occupy intermediate proportions, while hydrogeologic conditions are also unevenly represented (confined: $n = 2,737$, 4%; unconfined: $n = 6,613$, 9%).

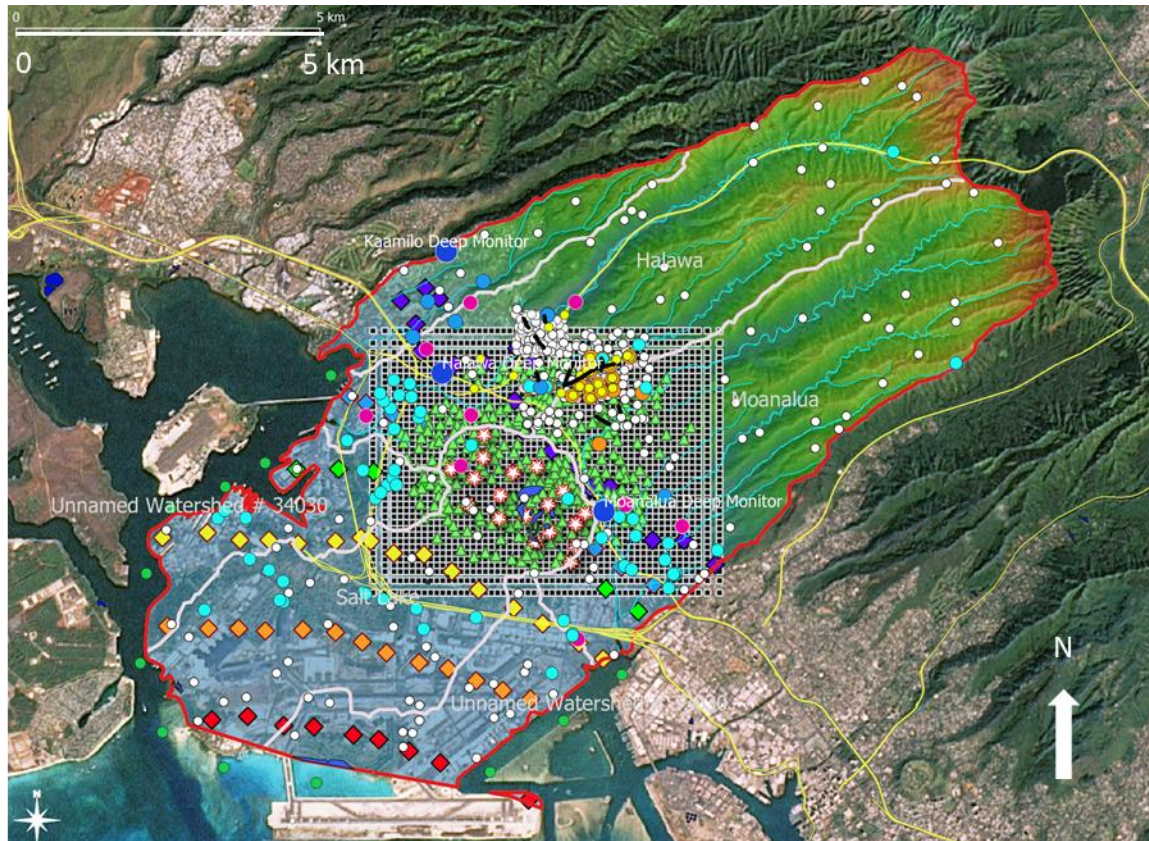


Fig. 3. Spatial distribution of hydrogeophysical observations used to construct the reference model for the Hālawa–Moanalua aquifer. Symbols indicate observation type and depth constraint. Triangles show interpreted depths to the caprock-pāhoehoe contact (red = 304 m, orange = 243 m, yellow = 183 m, green = 122 m, cyan = 61 m, blue = 0 m), and circles denote wells, including water wells (light blue), deep monitoring wells (royal blue), water supply wells (magenta), synthetic wells (white), and harbor nodes (green). Gravity stations are shown as green triangles. The right panel illustrates observation density within the central aquifer, including inverted geophysical properties (density from gravity and velocity from seismic refraction), interpreted seismic reflections marking lithologic contrasts, and hydrogeologic measurements collected at disposal, plume, and monitoring wells. Measured features include lithology, rock quality designation, fracture rate, oxidation-reduction potential, specific conductance, temperature, and water level.

3.1.2. Continuous features

Seismic velocity values within the Data Cube are derived using multiple complementary approaches: (i) conversion from rock quality designation (RQD) using published empirical relationships (Fathani et al., 2018); (ii) assignment of median velocities by geologic unit based on published ranges (Bücker et al., 1999; Miller et al., 2016); and (iii) inversion of seismic refraction data (Liberty and St. Clair, 2023). Depth-

dependent seawater properties to approximately 25 m are obtained from harbor seismic profiles (PacIOOS, 2023). Water-level and water-quality data are sourced from monitoring wells (USGS, 2023) and the Hawai‘i Play Fairway Analysis datasets (Lautze et al., 2014a, b; Lautze, 2017). Temperature, barometric pressure, and specific conductance data are obtained from deep monitoring wells maintained by the Board of Water Supply (2023). A summary of numerical feature counts incorporated into the reference model is provided in Table 3.

Indirect subsurface constraints are incorporated through geophysical models, including a three-dimensional density model derived from gravity data (Ito et al., 2019) and two-dimensional seismic refraction velocity and reflection sections along survey profiles (Liberty and St. Clair, 2018). Seismic reflections are interpreted as impedance contrasts at the saprolite–pāhoehoe contact. Above this interface, saprolite is assumed to be vertically homogeneous extending upward to the base of alluvium (where present), while undifferentiated pāhoehoe extends downward from the contact to the base of the model. The saprolite is further assumed to be homogeneous and impermeable, thereby hydraulically confining the underlying pāhoehoe within the study area.

Additional structural constraints include digitized interpretations of the caprock–pāhoehoe contact derived from drilling records (Hunt, 1997). At these locations, caprock extends from the contact to the aquifer surface, with the underlying undifferentiated pāhoehoe assumed to be confined and laterally continuous. Drill records are grouped into discrete depth intervals (0–304 m; Fig. 3), revealing an impermeable wedge that thickens seaward. A limited number of soft prior constraints are also incorporated from mapped surface occurrences of alluvium and tuff (Sherrod et al., 2021). Finally, additional velocity estimates are assigned to borehole geologic units by applying empirical RQD–velocity relationships to observed borehole RQD values (Fathani et al., 2018).

Table 2.

Summary of categorical feature counts included in the Data cube. The table includes observation (direct or indirect), type (borehole, seismic refraction, drill depth, map, harbor, deep wells, and synthetic wells), name of observation, categorical feature counts (geologic unit and aquifer confinement), and reference.

Observation Type	Name	Categorical Feature Count												Reference	
		Geologic Unit						Aquifer Confinement							
		caprock	alluvium	saprolite	clinker (loose)	clinker (welded)	aa	pahoehoe	tuff	Confined	Unconfined	ocean	Total		
Direct	Borehole	RHP01	0	5	5	5	41	79	25	24	49	135	0	368	NavFac, 2018–2021
Direct	Borehole	RHP02	0	5	0	28	14	99	22	0	49	119	0	336	NavFac, 2018–2021
Direct	Borehole	RHP03	0	5	14	15	24	85	19	0	49	114	0	325	NavFac, 2018–2021
Direct	Borehole	RHP04A	0	24	3	28	33	69	8	0	49	140	0	354	NavFac, 2018–2021
Direct	Borehole	RHMW01R	0	48	6	56	66	138	109	0	258	688	0	1369	NavFac, 2018–2021
Direct	Borehole	RHMW02	0	0	0	15	4	20	64	0	21	478	0	602	NavFac, 2018–2021
Direct	Borehole	RHMW03	0	0	0	20	6	28	34	0	30	520	0	638	NavFac, 2018–2021
Direct	Borehole	RHMW04	0	1	0	0	0	0	35	0	27	294	0	357	NavFac, 2018–2021
Direct	Borehole	RHMW05	0	5	0	22	0	29	0	0	20	363	0	439	NavFac, 2018–2021
Direct	Borehole	RHMW6	0	0	36	8	0	129	0	0	42	239	0	454	NavFac, 2018–2021
Direct	Borehole	RHMW7	0	0	5	34	0	0	0	0	48	193	0	280	NavFac, 2018–2021
Direct	Borehole	RHMW8	0	15	0	78	0	80	89	28	29	291	0	610	NavFac, 2018–2021
Direct	Borehole	RHMW09	0	2	10	40	3	160	168	24	38	376	0	821	NavFac, 2018–2021
Direct	Borehole	RHMW10	0	11	9	59	6	178	230	7	34	476	0	1010	NavFac, 2018–2021
Direct	Borehole	RHMW11	0	68	193	37	6	57	132	0	318	192	0	1003	NavFac, 2018–2021
Direct	Borehole	RHMW12A	0	9	7	15	31	94	284	6	290	220	0	956	NavFac, 2018–2021
Direct	Borehole	RHMW13	0	22	22	92	2	128	263	2	301	230	0	1062	NavFac, 2018–2021
Direct	Borehole	RHMW14	0	41	60	32	10	51	302	0	350	160	0	1006	NavFac, 2018–2021
Direct	Borehole	RHMW15	0	2	3	81	62	177	262	3	300	290	0	1180	NavFac, 2018–2021
Direct	Borehole	RHMW16	0	40	37	42	24	93	263	0	312	198	0	1009	NavFac, 2018–2021
Direct	Borehole	RHMW17	0	0	0	0	0	0	0	0	39	471	0	510	NavFac, 2018–2021
Direct	Borehole	RHMW19	0	15	5	42	23	143	205	17	84	426	0	960	NavFac, 2018–2021
Direct	Borehole	OWD1	0	0	0	0	0	0	0	0	ND	ND	0	0	NavFac, 2018–2021
Direct	Borehole	OWD2A	0	8	14	0	35	64	43	0	ND	ND	0	164	NavFac, 2018–2021
Direct	Borehole	OWD3A	0	20	11	27	0	71	27	7	ND	ND	0	163	NavFac, 2018–2021
Direct	Borehole	OWD4	0	5	0	4	17	135	23	0	ND	ND	0	184	NavFac, 2018–2021
Direct	Borehole	OWD5	0	16	7	26	13	41	32	8	ND	ND	0	143	NavFac, 2018–2021
Direct	Borehole	OWD6	0	20	12	66	1	94	24	0	ND	ND	0	217	NavFac, 2018–2021
Direct	Borehole	OWD7	0	8	45	30	10	105	47	0	ND	ND	0	245	NavFac, 2018–2021
Direct	Borehole	OWD8	0	16	74	52	30	233	73	0	ND	ND	0	478	NavFac, 2018–2021
Indirect	Seismic refraction	Profile A	0	908	4490	336	145	0	2963	84	ND	ND	0	8926	Liberty and St. Clair, 2018
Indirect	Seismic refraction	Profile B	0	781	1032	44	41	0	1269	0	ND	ND	0	3167	Liberty and St. Clair, 2019
Indirect	Seismic refraction	Profile C	0	1135	1822	524	312	0	165	118	ND	ND	0	4076	Liberty and St. Clair, 2020
Indirect	Seismic refraction	Profile D	0	1810	5046	560	79	0	0	0	ND	ND	0	7495	Liberty and St. Clair, 2021
Indirect	Seismic refraction	Profile E	0	891	2766	0	0	0	0	0	ND	ND	0	3657	Liberty and St. Clair, 2022
Indirect	Seismic refraction	Profile F	0	716	1684	366	49	0	0	2	ND	ND	0	2817	Liberty and St. Clair, 2023
Indirect	Seismic refraction	Profile G	0	2172	1678	908	1420	0	1166	1009	ND	ND	0	8353	Liberty and St. Clair, 2024
Indirect	Seismic refraction	Profile H	0	2515	2170	82	0	0	0	0	ND	ND	0	4767	Liberty and St. Clair, 2025
Indirect	Seismic refraction	Profile I	0	650	1050	0	0	0	0	0	ND	ND	0	1700	Liberty and St. Clair, 2026
Indirect	Seismic reflection	saprolite-pahoehoe	0	0	2994	0	0	0	2994	0	ND	ND	0	5988	Liberty and St. Clair, 2027
Indirect	Drilling	caprock-pahoehoe	3692	0	0	0	0	0	776	1653	ND	ND	0	6121	Hunt, 1997
Indirect	Map	Alluvium	0	94	0	0	0	0	0	0	ND	ND	0	94	Sherrod et al., 2021
Indirect	Map	Caprock	110	0	0	0	0	0	0	0	ND	ND	0	110	Sherrod et al., 2022
Indirect	Map	Tuff	0	0	0	0	0	0	0	90	ND	ND	0	90	Sherrod et al., 2023
Indirect	Harbor	Nodes	0	0	0	0	0	0	0	0	ND	ND	0	28	PadOOS, 2023
Indirect	Deep well	Kaamilo	0	0	0	0	0	0	9	0	ND	ND	0	9	Board of Water Supply, 2023
Indirect	Deep well	Halawa	0	0	0	0	0	0	9	0	ND	ND	0	9	Board of Water Supply, 2023
Indirect	Deep well	Moanalua	0	0	0	0	0	0	9	0	ND	ND	0	9	Board of Water Supply, 2023
Indirect	Synthetic	Wells	0	0	0	0	0	0	1152	0	ND	ND	0	1152	This study
		Sum =	3802	12083	25310	3774	2507	2580	13295	3082	2737	6613	28	75811	
		Fraction =	0.05	0.16	0.33	0.05	0.03	0.03	0.18	0.04	0.04	0.09	0.0004	1	

ND = no data.

Table 3.

Summary of numerical feature counts included in the Data cube. The table includes observation (direct or indirect), type (borehole, seismic refraction, gravity, contact depth, map, harbor, deep wells, and synthetic wells), name of observation, and reference.

Observation	Type	Name	Numerical Feature Count											
			Geophysical			Engineering			Water Quality					
			>	<	Rock quality designation ³	Fracture Rate ³	Barometric pressure ⁴	Temperature ⁴	Conductance ⁴	Dissolved oxygen ⁴	Oxygen reduction potential ⁴	pH ⁴	Total	Reference
Indirect	Borehole	RHP01	177	3	154	157	0	25	24	3	1	1	545	See list below.
Indirect	Borehole	RHP02	162	0	137	144	0	7	11	2	1	1	465	See list below.
Indirect	Borehole	RHP03	157	0	141	141	0	14	1	1	1	1	457	See list below.
Indirect	Borehole	RHP04A	141	0	154	165	0	14	14	14	14	14	530	See list below.
Indirect	Borehole	RHMW01R	235	1	264	166	1	25	25	15	15	15	762	See list below.
Indirect	Borehole	RHMW02	100	0	108	5	0	15	15	15	15	15	288	See list below
Indirect	Borehole	RHMW03	84	0	116	20	0	13	13	13	13	13	285	See list below
Indirect	Borehole	RHMW04	35	0	50	50	0	11	11	11	11	11	190	See list below
Indirect	Borehole	RHMW05	51	0	102	5	0	18	18	18	18	18	248	See list below
Indirect	Borehole	RHMW06	160	12	269	12	0	0	0	0	0	0	453	See list below
Indirect	Borehole	RHMW07	39	5	1	1	0	0	0	0	0	0	46	See list below
Indirect	Borehole	RHMW08	275	0	304	309	0	10	10	10	10	10	938	See list below
Indirect	Borehole	RHMW09	405	10	413	411	0	11	11	11	11	11	1294	See list below
Indirect	Borehole	RHMW10	489	9	495	499	0	10	10	10	10	10	1542	See list below
Indirect	Borehole	RHMW11	425	193	488	459	0	0	0	0	0	0	1565	See list below
Indirect	Borehole	RHMW12A	431	1	446	442	0	11	11	11	11	11	1375	See list below
Indirect	Borehole	RHMW13	509	22	529	22	0	0	0	0	0	0	1082	See list below
Indirect	Borehole	RHMW14	422	27	473	41	0	0	0	0	0	0	963	See list below
Indirect	Borehole	RHMW15	588	3	572	2	0	0	0	0	0	0	1165	See list below
Indirect	Borehole	RHMW16	458	36	472	40	0	10	10	10	10	10	1056	See list below
Indirect	Borehole	RHMW17	0	0	0	0	0	10	10	10	10	10	50	See list below
Indirect	Borehole	RHMW19	435	5	445	15	0	11	11	11	11	11	955	See list below
Indirect	Borehole	OWD1	0	0	0	0	0	0	0	0	0	0	0	See list below
Indirect	Borehole	OWD2A	152	0	159	15	0	0	0	0	0	0	326	See list below
Indirect	Borehole	OWD3A	136	0	143	0	0	0	0	0	0	0	279	See list below
Indirect	Borehole	OWD4	179	0	169	0	0	0	0	0	0	0	348	See list below
Indirect	Borehole	OWD5	121	0	126	0	0	0	0	0	0	0	247	See list below
Indirect	Borehole	OWD6	188	0	22	0	0	0	0	0	0	0	210	See list below
Indirect	Borehole	OWD7	237	0	244	0	0	0	0	0	0	0	481	See list below
Indirect	Borehole	OWD8	221	1	84	1	1	1	1	1	1	1	313	See list below
Indirect	Seismic refraction	Profile A	7825	0	0	0	0	0	0	0	0	0	7825	Liberty and St. Clair, 2018
Indirect	Seismic refraction	Profile B	2929	0	0	0	0	0	0	0	0	0	2929	Liberty and St. Clair, 2019
Indirect	Seismic refraction	Profile C	3955	0	0	0	0	0	0	0	0	0	3955	Liberty and St. Clair, 2020
Indirect	Seismic refraction	Profile D	6893	0	0	0	0	0	0	0	0	0	6893	Liberty and St. Clair, 2021
Indirect	Seismic refraction	Profile E	3193	0	0	0	0	0	0	0	0	0	3193	Liberty and St. Clair, 2022
Indirect	Seismic refraction	Profile F	2443	0	0	0	0	0	0	0	0	0	2443	Liberty and St. Clair, 2023
Indirect	Seismic refraction	Profile G	8353	0	0	0	0	0	0	0	0	0	8353	Liberty and St. Clair, 2024
Indirect	Seismic refraction	Profile H	4771	0	0	0	0	0	0	0	0	0	4771	Liberty and St. Clair, 2025
Indirect	Seismic refraction	Profile I	1700	0	0	0	0	0	0	0	0	0	1700	Liberty and St. Clair, 2026
Indirect	Gravity	Density model	0	37027	0	0	0	0	0	0	0	0	37027	Ito et al., 2027
Indirect	Contact depth	Caprock-Pahoehoe	6133	5203	0	0	0	0	0	0	0	0	11336	Hunt, 1997
Indirect	Map	Alluvium	94	0	94	94	0	0	0	0	0	0	282	Sherrod et al., 2021
Indirect	Map	Caprock	110	110	0	0	0	0	0	0	0	0	220	Sherrod et al., 2022
Indirect	Map	Tuff	90	90	0	0	0	0	0	0	0	0	180	Sherrod et al., 2023
Direct	Deep well	Kaamilo profile	0	0	0	0	4919	4919	4919	61	61	61	14940	Board of Water Supply, 2023
Direct	Deep well	Halawa profile	0	0	9	0	4231	4231	4231	395	395	395	13887	Board of Water Supply, 2023
Direct	Deep well	Moanalua profile	0	0	9	0	4741	4741	4741	309	309	309	15159	Board of Water Supply, 2023
Direct	Harbor	Seawater profile	28	28	28	28	28	28	28	28	28	28	280	PacIOOS, 2023
		Sum =	55529	42786	7220	3244	13921	14135	14125	959	956	956	153831	
		Fraction =	0.36	0.28	0.05	0.02	0.09	0.09	0.09	0.01	0.01	0.01	1	

References: ¹Fathani et al., 2018; ²Bücker et al., 1999; Miller et al., 1988; ³NavFAC, 2018-2021; ⁴Hunt, C.D., 2004

3.2 Reference model

3.2.1. Training and testing

Prior to training, continuous input features are normalized by their variance, and input feature vectors are randomly ordered to initialize the map weight vectors. The self-organizing map (SOM) is trained using a fixed number of neurons (map nodes) and predefined topological relationships. A toroidal grid topology—wrapping both vertically and horizontally—is employed, with hexagonally arranged neurons to preserve neighborhood continuity. The initial number of map units (M) is determined using the heuristic proposed by Vesanto and Alhoniemi (2000), where $M = 5V/N$ and N is the total number of training samples. This heuristic, which is based on the ratio of the two largest eigenvalues of the data covariance matrix, is used to define the initial grid dimensions (66 rows \times 60 columns) for the Hālawa–Moanalua aquifer *reference model*.

To assess the influence of map resolution on training quality, two additional SOM grids are constructed and evaluated following the method of Friedel et al. (2020). The second grid is generated by scaling the initial grid dimensions by a factor of 1.5, and the third grid is generated by scaling the second

grid by an additional factor of 1.5. These progressive increases in grid size result in corresponding increases in the total number of nodes (grid 1: 3,690 nodes; grid 2: 9,000 nodes; grid 3: 15,840 nodes) and in the computational cost required for model training and validation (Table 4).

Table 4.

Summary of unsupervised training topologies for each regional model. SOM=the self-organizing map.

Map grid	Data cube	Initialization	Grid shape	Lattice type	Map size		
					Rows	Columns	Nodes
1	Hālawa-Moanalua	Random	Toroid	Hexagonal	66	60	3960
2	Hālawa-Moanalua	Random	Toroid	Hexagonal	100	90	9000
3	Hālawa-Moanalua	Random	Toroid	Hexagonal	132	120	15840

Training of the self-organizing maps is conducted in two sequential phases: an initial rough training phase followed by a fine-tuning phase. A summary of the number of iterations for each phase, the corresponding Gaussian neighborhood radii, and the resulting quantization and topographic errors is provided in Table 5. For all map grids, learning rates decrease linearly from initial and final values of 0.5 and 0.05, respectively, and continue decaying to 10^{-5} . In parallel, the Gaussian neighborhood function decreases exponentially (e.g., decay rate of 10^{-3} iteration $^{-1}$), yielding stable convergence across all network configurations.

Table 5.

Summary of self-organizing map topologies for different size maps.

Map grid	Data cube	Training phase	Neighborhood type	Radius	Radius	Training	Final	Final
				initial	final	length	quantization error	topographic error
1	Hālawa-Moanalua	Rough	Gaussian	90	23	20	0.167	0.065
	Hālawa-Moanalua	Fine	Gaussian	23	1	400		
2	Hālawa-Moanalua	Rough	Gaussian	135	34	20	0.109	0.062
	Hālawa-Moanalua	Fine	Gaussian	34	1	400		
3	Hālawa-Moanalua	Rough	Gaussian	179	45	20	0.077	0.053
	Hālawa-Moanalua	Fine	Gaussian	45	1	400		

Evaluation during the final testing phase indicates that all three grid configurations converge to stable maps, as reflected by similar quantization and topographic error values. Summary statistics from unsupervised training across different network sizes produce comparable Cohen's kappa and overall accuracy values, indicating near-perfect predictability of geologic units (Cohen, 1960) regardless of the testing fold (Table 6). Given this consistency, the final model training is performed by presenting the complete set of Hālawa–Moanalua aquifer features (training and testing combined; 100%) to the smallest map grid (map grid 1). The resulting trained reference map is then used to simultaneously estimate transdisciplinary aquifer features—including geologic, geophysical, engineering, and water-quality attributes—referred to as the deterministic *reference model*.

Table 6.

Summary statistics for unsupervised training (modified self-organized map) applied to Hālawa-Moanalua aquifer features with different network sizes.

Map grid	Selected Fold	Training		Testing		
		Map size	n (80%)	n (20%)	Kappa	Accuracy
1	10	66 x 60	51475	12866	0.84	0.91
2	10	100 x 90	51475	12866	0.84	0.91
3	10	132 x 120	51475	12866	0.87	0.93
1	15	66 x 60	51475	12866	0.82	0.90
2	15	100 x 90	51475	12866	0.85	0.92
3	15	132 x 120	51475	12866	0.87	0.94

3.2.3. Grouping features

A component-planes plot of the Hālawa–Moanalua (H–M) aquifer features is presented in Fig. 4. This plot provides a visual representation of nonlinear relationships among the multivariate input data at the local borehole scale and illustrate how features are organized across the self-organizing map. Patterns and associations among variables are examined by comparing the spatial distribution of values across the component planes (Vesanto and Alhoniemi, 2000). Component values are scaled such that dark red and dark blue represent the highest and lowest values of each input feature, respectively. This color scaling facilitates direct comparison of feature intensity and absence across the map.

For categorical variables—including geologic units (caprock, alluvium, saprolite, loose clinker, welded clinker, ‘āā, pāhoehoe, and tuff), aquifer confinement or saturation state (saturated or unsaturated), and ocean—the red color indicates the presence of a given category, while blue indicates its absence. During categorical training, geologic unit, saturation state, and ocean indicators are treated as mutually exclusive end members. As a result, the presence of any one category produces a red component plane, whereas its absence yields a blue plane. The spatial extent of red regions within each categorical component plane reflects the relative frequency of observations, with smaller regions indicating rarer features (e.g., ocean and ‘āā) and larger regions indicating more abundant units (e.g., pāhoehoe or saprolite). This representation provides an intuitive visualization of class imbalance within the H–M dataset.

Component planes are composed of networks of nodes arranged on a toroidal grid; therefore, the relative positioning of features across planes provides a means to evaluate whether the SOM has assimilated and grouped the input data appropriately. Consistent spatial alignment of features across multiple component planes indicates coherent organization within the trained network. For example, the localized red region associated with the welded clinker unit corresponds, at the same toroidal locations, to low-density values, unsaturated conditions, and low barometric pressure in other component planes. These systematic associations indicate that aquifer features are meaningfully separated and internally consistent across the map. Having confirmed appropriate feature assimilation and separation, principal component analysis is subsequently applied to the median values of the component planes to further evaluate dominant patterns in the data.

Principal component analysis (PCA) of the median component-plane values along the first two principal axes reveals relationships that are both internally consistent and physically intuitive (Fig. 5). The clear separation among aquifer feature vectors (shown as blue vectors) indicates that the associated hydrogeophysical observations contain sufficient and mutually informative structure to support

development of a coherent Hālawa–Moanalua reference model. This separation suggests that the self-organizing map has successfully captured meaningful variability within the multivariate dataset. Moreover, the PCA results demonstrate that dominant patterns in the data align with expected hydrogeologic controls.

The PCA biplot further reveals four distinct groupings of aquifer features, with features within each group exhibiting stronger relationships to one another than to those in other groups. Features located in opposing groupings—for example, confined aquifer conditions (red group) versus unconfined aquifer conditions (brown group)—are antithetically, or negatively, correlated. Within each grouping, feature vectors that are closer together indicate stronger positive associations, whereas greater angular separation reflects weaker relationships. This structure provides a quantitative basis for interpreting how hydrogeologic properties co-vary across the aquifer system.

The confined aquifer grouping (red) indicates that increasing depth is associated with higher pāhoehoe abundance, greater rock quality designation (RQD), elevated barometric pressure, higher seismic velocity, increased density, and specific conductance. The increasing angular separation between density and conductance relative to the confined aquifer vector suggests that these relationships, while positive, are comparatively weaker. In contrast, the shallow unconfined aquifer grouping is characterized by strong associations among alluvium, saprolite, tuff, and temperature, reflecting near-surface conditions influenced by lithology and thermal gradients. Together, these groupings reinforce the physical consistency of the PCA results and their relevance to hydrogeologic interpretation.

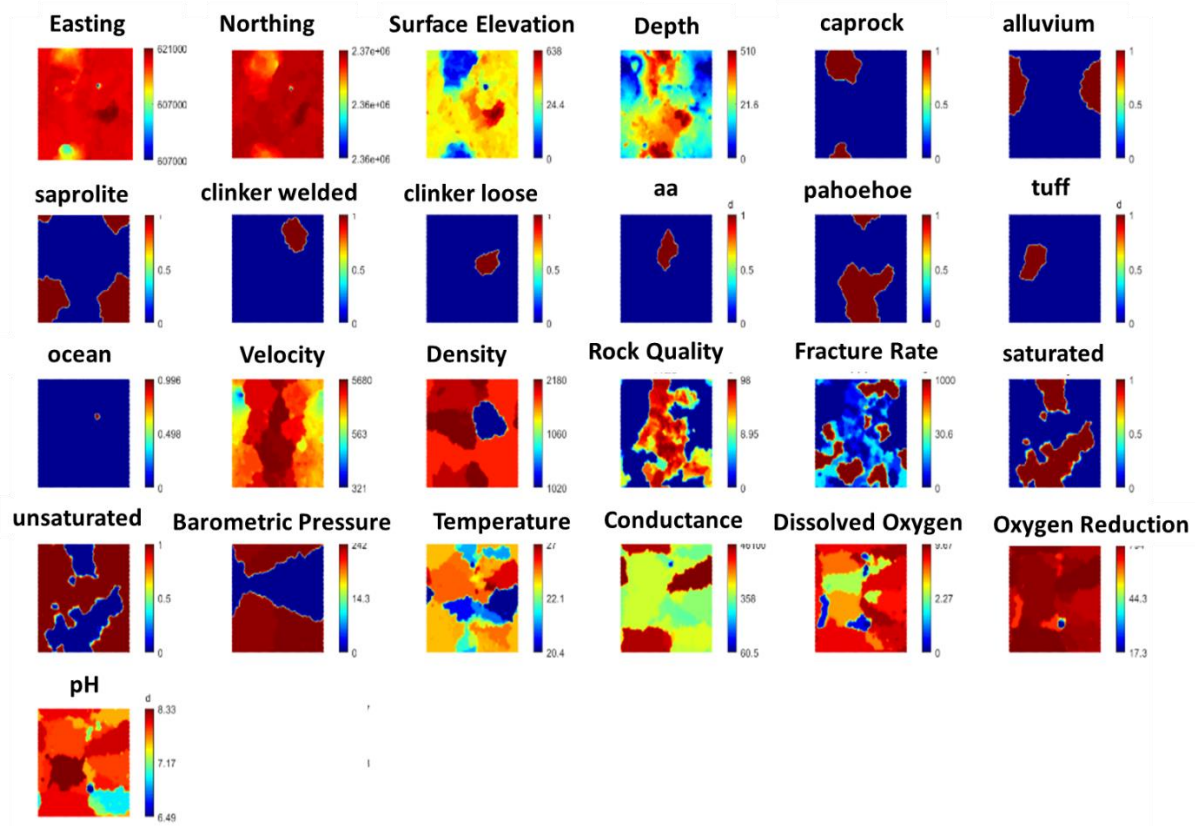


Fig. 4. Component planes of features across the SOM grid (toroid) characterizing the subregional Hālawa-Moanalua aquifer, Oahu, Hawai‘i. Categorical features, e.g., geologic units (‘a‘ā, alluvium, caprock, clinker - loose, clinker - welded, pāhoehoe, saprolite, tuff), aquifer type (basal or unsaturated) and ocean (absent or present) and continuous features, e.g., easting, northing, surface elevation, depth, velocity, density, rock quality designation, fracture rate, barometric pressure, temperature, conductance, dissolved oxygen, oxygen reduction potential, and pH. Component planes are color coded where high values are hot (red) and low values are cool (blue). Same colors at same positions indicate positive correlation, and opposite colors at same positions indicate negative correlation. See Table 7 for feature units.

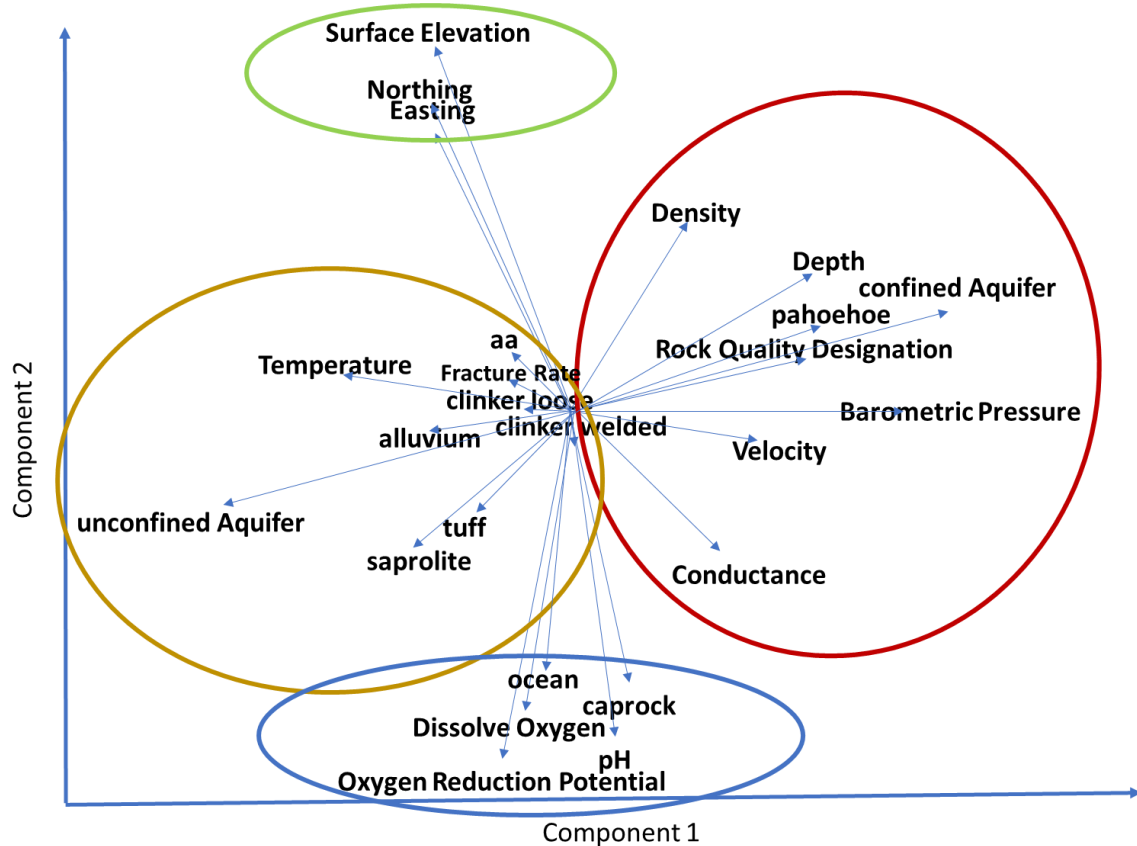


Fig. 5. Principal component analysis of features characterizing the subregional Hālawa-Moanalua aquifer. Categorical features (e.g., geologic units and aquifer confinement) are not capitalized, whereas continuous features are capitalized. Short feature vectors imply relatively few observations whereas long feature vectors reveal relatively many observations. The heterogeneity in vector lengths underscores the extremely imbalanced nature of observations in the data cube. Those features grouped together (e.g., grouped by same color circles) are more positively related whereas those on opposite sides are anti-correlated (e.g., brown and red circle, and green and blue circles). See Table 7 for feature units.

3.3 Site model

3.3.1. Synthetic data generation methods

A fixed number of synthetic observations are estimated using each AI generative algorithm, including the TGC, TVAE, CTGAN, and CopulaGAN. The synthetic datasets comprise both categorical features (e.g., geology and aquifer type) and numerical features (e.g., geophysical, engineering, and water-quality attributes) corresponding to the H-M reference model. For the Hālawa–Moanalua aquifer, nonparametric probability density functions and cumulative distribution functions are constructed from a fixed number of synthetic observations (N=1,000,000) for each feature (Figs. 6 and 7). In these analyses, *real observations* refer to measurements extracted from the data cube, whereas *synthetic observations* denote observations generated by the respective generative models. Metadata common to all four algorithms includes the enforcement of minimum and maximum feature values, no rounding, and 500 epochs.

The full set of aquifer features used in the analysis, including spatial, hydrogeologic, engineering, and water-quality attributes, along with their units and categorical encodings, is summarized in Table 7. By generating an equal number of synthetic observations for each model, distribution-based quality metrics are applied consistently to identify a preferred generative algorithm. The selected model is subsequently used to produce stochastic distributions from which a predetermined number of synthetic records are sampled and integrated with the reference model observations. This procedure is repeated while systematically increasing the number of synthetic point-cloud observations generated by each approach, enabling evaluation of algorithmic performance as a function of synthetic data volume.

Table 7.

Description of features used in the synthetic data generation and evaluation across the Hālawa–Moanalua aquifer.

Feature	Description	Units / Encoding	Type
Easting	Easting coordinate	UTM	Numerical
Northing	Northing coordinate	UTM	Numerical
ELEVsurfm	Surface elevation	m	Numerical
DEPTHmbgs	Depth below ground surface	m	Numerical
VELOCITY	Seismic velocity	m/s	Numerical
DENSITY	Bulk density	kg/m ³	Numerical
RQD	Rock Quality Designation	%	Numerical
FPF	Fracture rate	count/m	Numerical
ConfWLyes	Confined aquifer indicator	1 = yes, 0 = no	Categorical
ConfWLno	Unconfined aquifer indicator	1 = yes, 0 = no	Categorical
PRES	Barometric pressure	psi	Numerical
TEMPC	Temperature	°C	Numerical
COND	Specific conductance	µS/cm	Numerical
DO	Dissolved oxygen	mg/L	Numerical
ORP400	Oxidation–reduction potential	mV	Numerical
PH	pH	–	Numerical
Geology_id	Geological unit	0 = caprock; 1 = alluvium; 2 = saprolite; 3 = clinker–loose; 4 = clinker–welded; 5 = 'a'ā; 6 = pāhoehoe; 7 = tuff	Categorical

Geology is fundamental to groundwater-flow modeling because it controls groundwater pathways, flow velocities, and subsurface interactions. Accordingly, the reliability of a groundwater model depends on the accuracy of its geologic representation. To assess the performance of generative algorithms in reproducing observed geologic variability, bar charts comparing the proportional distributions of observed (real) and estimated (fake) geologic units are presented (Fig. 6). The results indicate that CopulaGAN most accurately reproduces geologic unit proportions under conditions of extreme class imbalance. TGC and TVAE also provide reasonable approximations; however, TGC overestimates the proportion of caprock, the most frequently observed unit, while TVAE overestimates pahoehoe, the second most abundant unit. In contrast, CTGAN exhibits an approximately linear response across categories, leading to underrepresentation of units with large sample sizes and overrepresentation of those with small sample sizes.

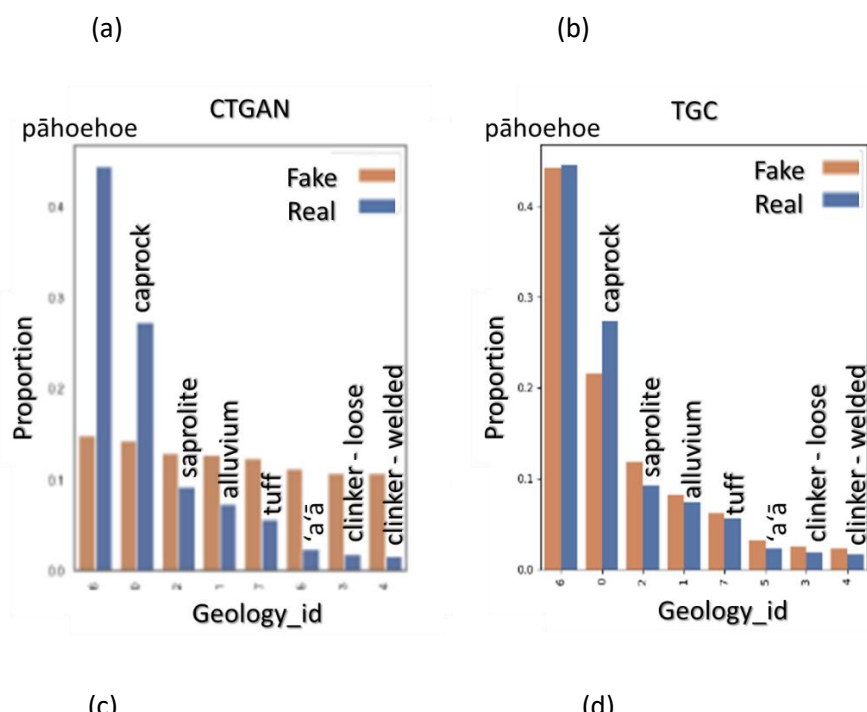
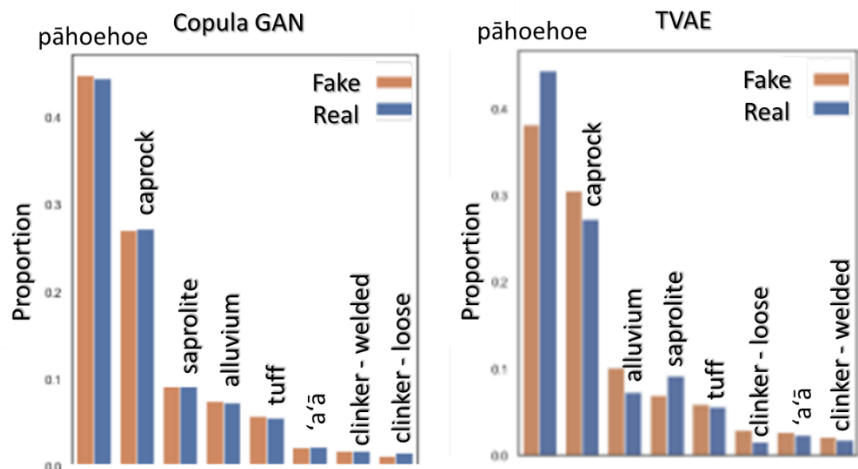
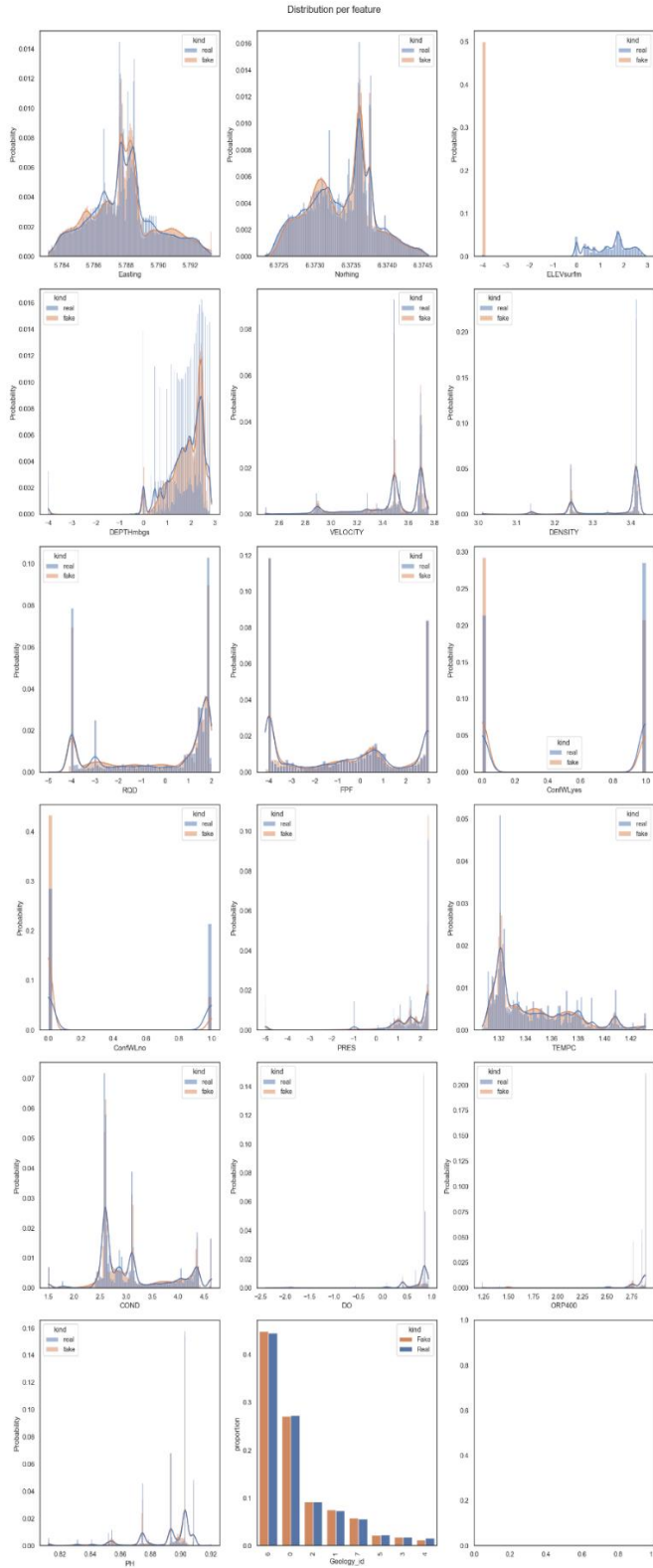
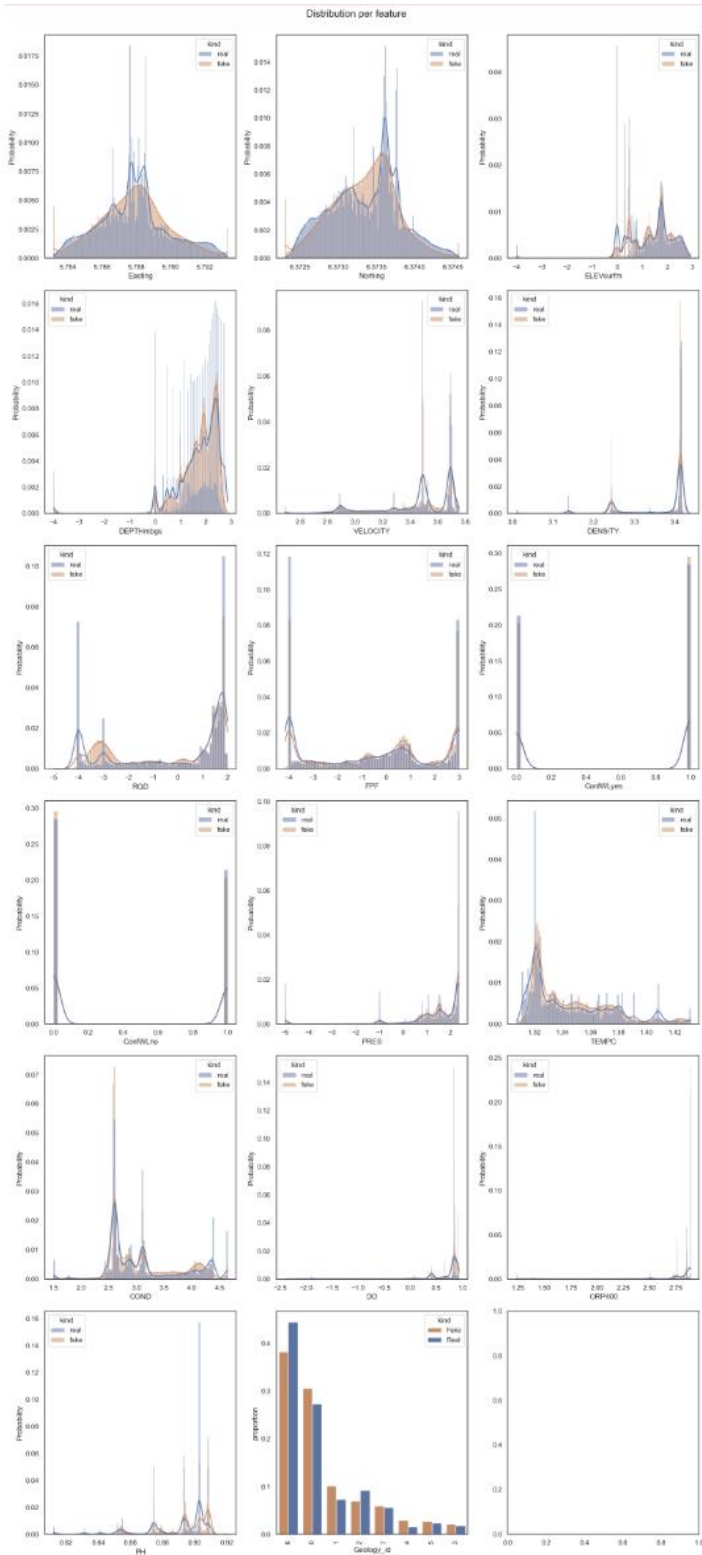


Fig. 6. Comparison of Real and Fake geologic unit proportions. (a) Copula Generative Adversarial Network - Copula GAN, (b) Tabular Variational Autoencoder - TVAE, (c) Constrained Generative Adversarial Network - CTGAN, and (d) Tabular Gaussian Copula - TGC. *Real* denotes observed observations extracted from the data cube, whereas *Fake* denotes synthetic observations generated by the respective algorithms. The order of each bar chart is set according to proportion of fake geologic units.

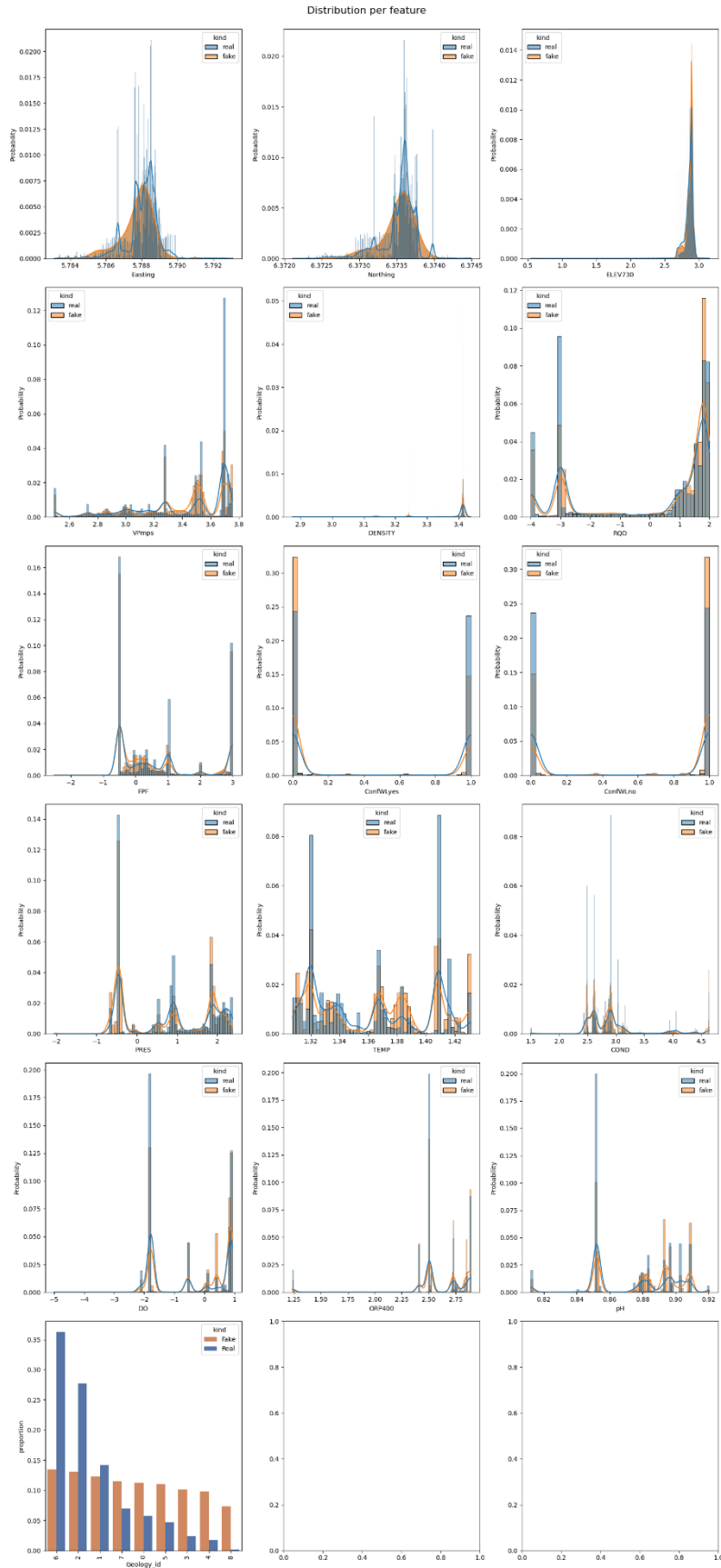
Inspection of the nonparametric probability density functions (Fig. 7) and cumulative distribution functions (Fig. 8) reveals clear differences among the generative algorithms in their ability to reproduce observed (real) distributions for both categorical and numerical features. For the categorical representation of Hālawa–Moanalua geologic units (Geology_id), model performance ranks, from highest to lowest, as CopulaGAN, TVAE, Gaussian Copula, and CTGAN. For numerical variables, the deep generative models generally capture the multimodal structure of the observed distributions, although reproduction of extreme values is less consistent (Fig. 7b–d). In contrast, the TGC model shows limited capacity to reproduce multimodality in the continuous aquifer features, consistent with its assumption of an underlying Gaussian dependence structure (Fig. 7b–d). These observations are further supported by inspecting the cumulative distribution functions for both numerical and categorical AI-generated features (Fig. 8a–d). Given the importance of geologic heterogeneity in groundwater flow and transport simulations, and the comparatively weaker performance of TGC in representing key continuous features, CopulaGAN is selected as the preferred feature generative approach for subsequent analyses. Quantitative performance metrics are then applied to formally evaluate and corroborate the visually inferred differences among models.



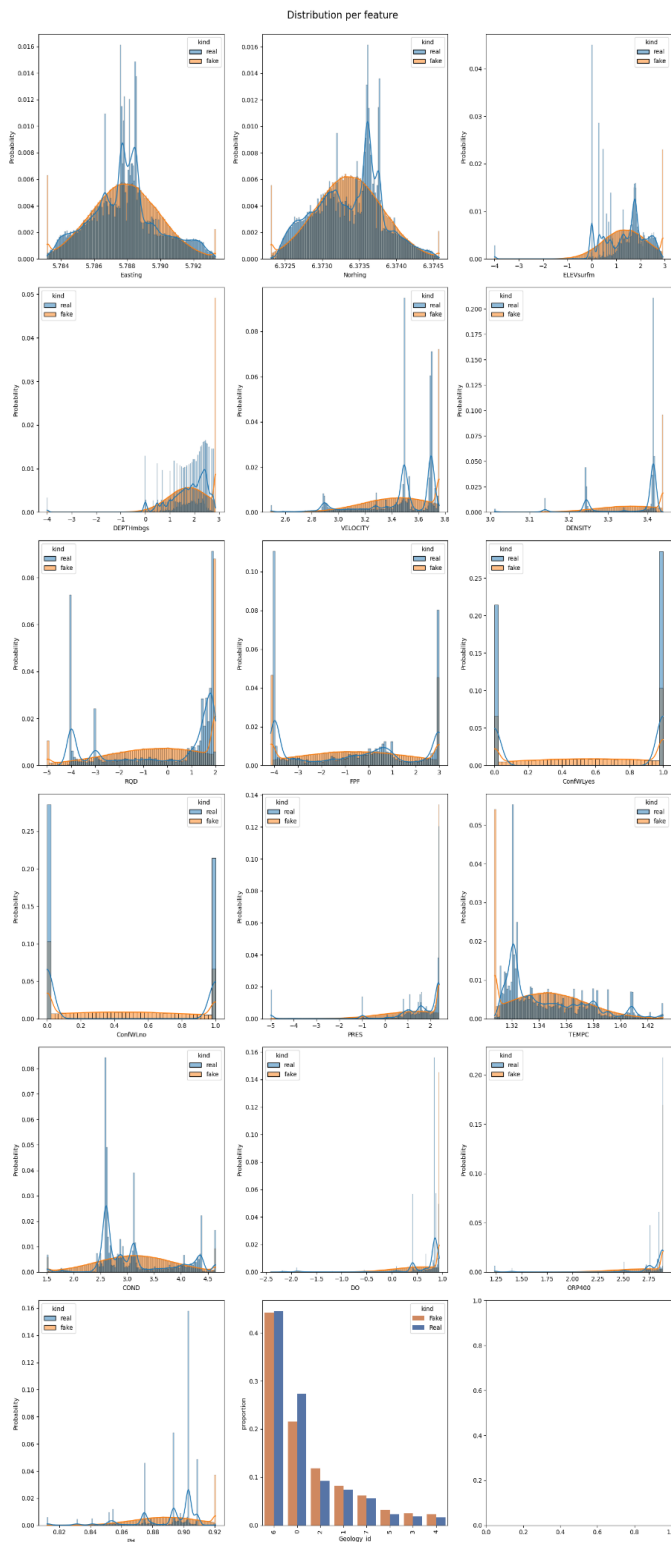
(a) Copula Generative Adversarial Network - Copula GAN



(b) Tabular Variational Autoencoder – TVAE

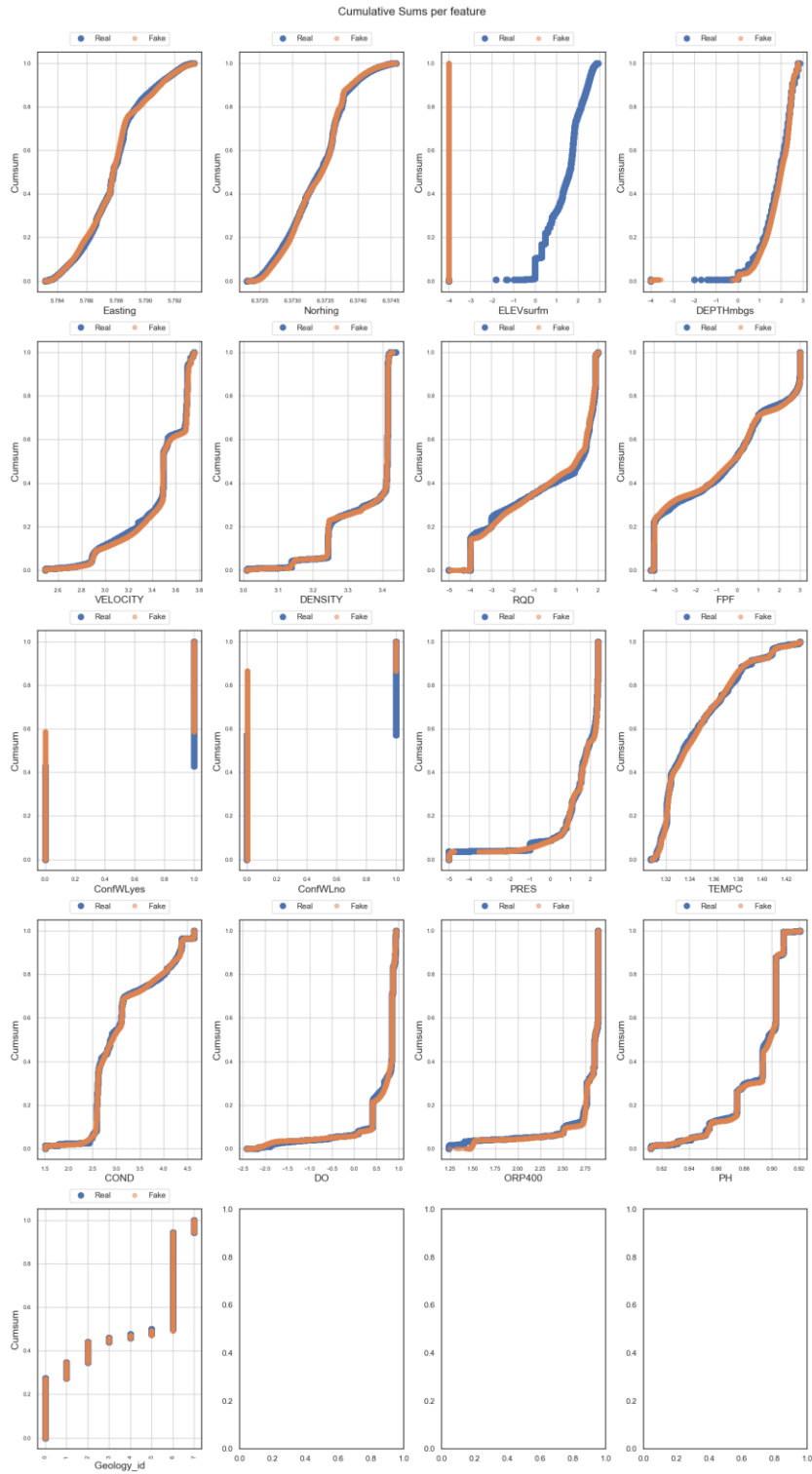


(c) Constrained Tabular Generative Adversarial Network - CTGAN

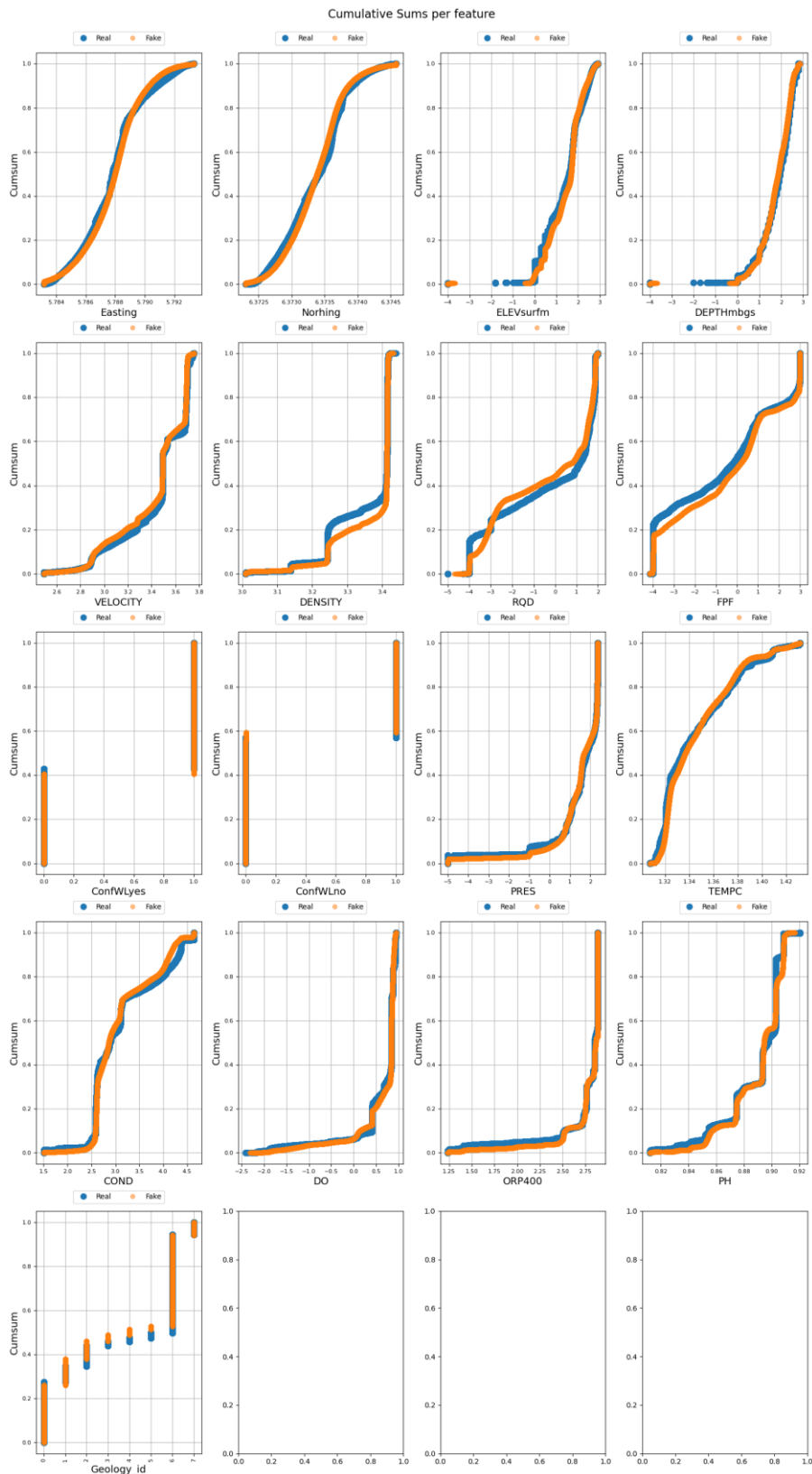


(d) Tabular Gaussian copula - TGC.

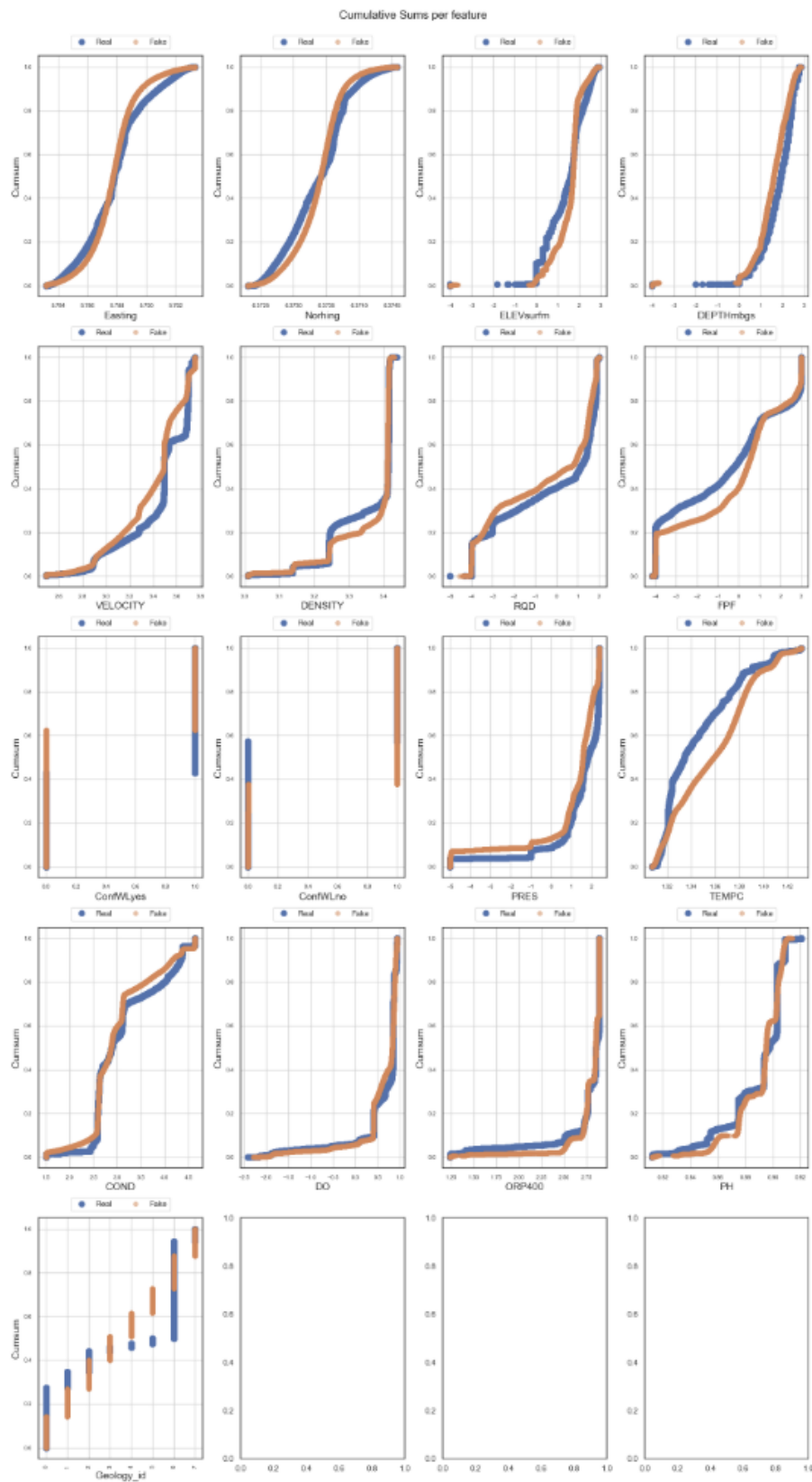
Fig. 7. Distribution functions of numerical and categorical features generated by the generative AI models ($N = 1,000,000$) for the Hālawa–Moanalua aquifer. *Real* denotes observed data extracted from the data cube, whereas *Fake* denotes synthetic observations generated by the respective algorithms. Variables include spatial coordinates, subsurface and engineering properties, hydrogeologic conditions, water-quality parameters, and geological unit classifications (see Table 7 for feature descriptions, units, and categorical encodings). (a) Copula Generative Adversarial Network - CopulaGAN, (b) Tabular Variational Autoencoder - TVAE, (c) Constrained Tabular Generative Adversarial Network – CTGAN; (d) Tabular Gaussian copula – TGC.



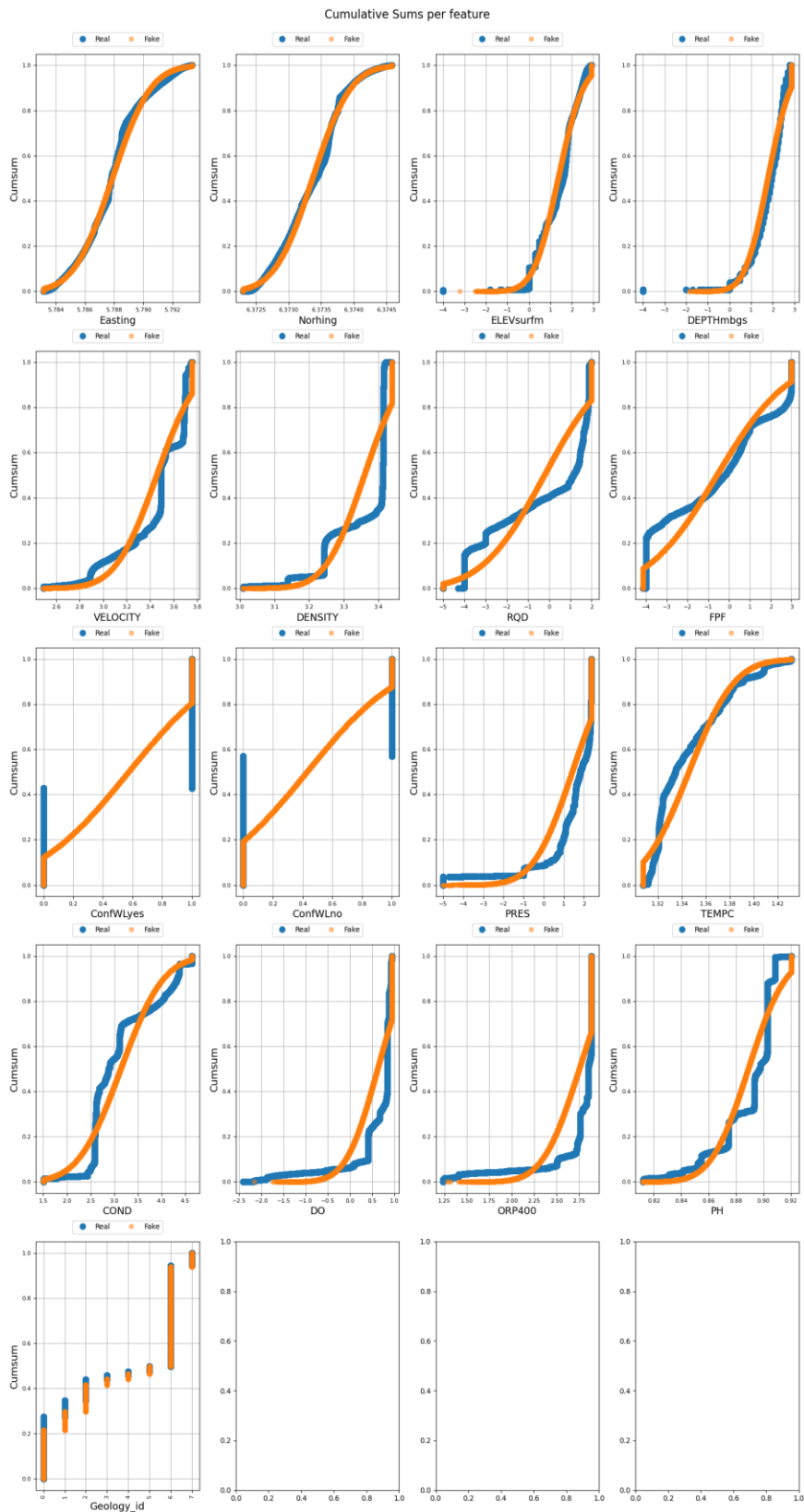
(a) Copula Generative Adversarial Network - Copula GAN



(a) Tabular Variational Autoencoder - TVAE



(b) Constrained Tabular Generative Adversarial Network - CTGAN



(c) Tabular Gaussian copula - TGC.

Fig. 8. Cumulative distribution functions of AI generated (N=1,000,000) numerical and categorical features for the Hālawa-Moanalua aquifer. *Real* denotes observed data extracted from the data cube, whereas *Fake* denotes synthetic observations generated by the respective algorithms. Variables include spatial coordinates, subsurface and engineering properties, hydrogeologic conditions, water-quality parameters, and geological unit classifications (see Table 7 for feature descriptions, units, and categorical encodings). (a) Copula Generative Adversarial Network - CopulaGAN, (b) Tabular Variational Autoencoder - TVAE, (c) Constrained Tabular Generative Adversarial Network – CTGAN; (d) Tabular Gaussian copula – TGC.

3.3.2. Validation of tabular generative algorithms

This section presents results from the application of multiple generative algorithms to the reference model. The results are summarized using tables, cumulative distribution functions, and probability distribution functions. Model performance is evaluated using the column shape score, column pair trends score, and average column score, based on AI-generated ensembles of 1,000,000 synthetic point-cloud values for both categorical and numerical features across the Hālawa–Moanalua aquifer (Table 8). At this scale of analysis, all generative algorithms exhibit broadly comparable performance, with TVAE showing marginally improved scores across the evaluated metrics.

Validation metrics for the synthetic AI generation of point-cloud values representing aquifer characteristics of the Hālawa–Moanalua aquifer are summarized in Table 9. In this analysis, the Kolmogorov–Smirnov (KS) complement metric is used to assess the ability of the generative algorithms to reproduce continuous aquifer properties and categorical aquifer confinement. KS complement values range from 0.66 to 0.96, where 0 indicates no correspondence and 1.0 indicates perfect correspondence; italicized values denote the lowest agreement, and bolded values denote the highest agreement. At this finer level of aquifer characterization, CopulaGAN performs best for the generation of numerical features, followed by TVAE, CTGAN, and TGC. In contrast, for categorical confinement, TVAE shows the strongest performance, followed by CTGAN, TGC, and CopulaGAN. These results indicate that different generative algorithms may be preferable for synthesizing numerical versus categorical aquifer features.

Summary statistics are used to compare numerical aquifer feature values estimated by the two-phase SOM-based deterministic reference model and the CopulaGAN-based stochastic site model (Table 10). Univariate statistics are computed for reference model values at field locations (N = 348,876) and for two CopulaGAN realizations with different numbers of synthetic point-cloud estimates (N = 525,000 and N = 695,000). Statistical measures, including sample size, mean, standard deviation, minimum, quartiles, and maximum, show strong agreement between the reference model and CopulaGAN estimates, indicating high repeatability of the stochastic generation process. The two CopulaGAN realizations exhibit nearly identical statistical characteristics, whereas larger differences between deterministic and stochastic estimates are attributed to uncertainty inherent in the reference model.

Table 8.

Comparison of metrics for AI generation of 1000000 synthetic observations of point cloud values for categorical and continuous features across the sub-regional Hālawa-Moanalua aquifer, Oahu, Hawai'i.

Geneartive AI algorithm	Column shapes	Column pair	Average score	Count
	score (%)	trends (%)	score (%)	
	(%)	(%)	(%)	
Tabular Gaussian Copula	79.0	93.3	86.2	1,000,000
Tabular Variational Autoencoder	86.6	97.2	91.4	1,000,000
Constrained Generative Adversarial Network	79.1	88.5	83.8	1,000,000
Copula Generative Adversarial Network	79.6	96.9	88.4	1,000,000

Table 9.

Validation metrics for synthetic AI generation (1000000 observations) of aquifer features at the Hālawa-Moanalua aquifer. The KS complement metrics range from 0.66 to 0.96 (1.0=perfect) with red values revealing lowest and black bolded revealing highest values. From this table, the order of best to worst algorithm for synthetic generation of continuous feature values are the CopulaGAN (preferred), TVAE, CTGAN and Gaussian copula.

Synthetic observations:		400k	400k	400k	400k	500k	1000k
Algorithm:		Gaussian copula	TVAE	CTGAN	CopulaGAN	CopulaGAN	CopulaGAN
Type	Feature	KS complement (%)					
Numerical	Easting (UTM)	0.93	0.95	0.92	0.96	0.96	0.96
	Northing (UTM)	0.92	0.91	0.87	0.98	0.98	0.98
	Surface elevation (m)	0.90	0.91	0.86	-	-	-
	Depth (m)	0.89	0.93	0.81	0.94	0.94	0.94
	Velocity (m/s)	0.79	0.92	0.84	0.91	0.91	0.91
	Density (kg/m3)	0.66	0.91	0.75	0.92	0.92	0.92
	Rock quality designation	0.76	0.88	0.87	0.89	0.89	0.89
	Fracture rate (count/m)	0.86	0.86	0.87	0.89	0.89	0.89
	Barometric pressure (psi)	0.74	0.89	0.78	0.94	0.94	0.94
	Temperature (C)	0.85	0.86	0.80	0.96	0.96	0.95
	Conductance	0.82	0.92	0.92	0.95	0.95	0.95
	Dissolved Oxygen	0.72	0.86	0.85	0.85	0.85	0.85
Categorical	pH	0.74	0.78	0.86	0.84	0.84	0.84
	Oxygen reduction potential	0.67	0.79	0.71	0.71	0.71	0.71

Table 10.

Statistical comparison of reference model to site model statistics for Hālawa-Moanalua aquifer features. The reference model reflects deterministic model values following application of the two phase self-organizing map to H-M observations from the data cube. The Site model reflects application of the Copula Generative Adversarial Network (CopulaGAN) algorithm to the reference model. The slight differences among the two synthesized CopulaGAN models (realizations) in prediction statistics are associated with uncertainty in the deterministic reference model.

Model	Algorithm					Depth (m)	Velocity (m/s)	Density (kg/m³)	Rock quality designation	Fracture rate (#/m)	Barometric pressure (psi)	Temperature (C)	Conductance (uS/cm)	Oxygen reduction potential (mv)		
		Easting	Northing	Fracture rate (#/m)	Barometric pressure (psi)									Dissolved oxygen (mg/l)	pH	
Reference	Self organizing map	count	348876	348876	348876	348876	348876	348876	348876	348876	348876	348876	348876	348876	348876	348876
		mean	613562.9	2362470.3	58	2844	2288	1	0	25.5	22.2	1361	4.19	164.1	7.74	
		Stdev	1.0	1.0	7	2	1	207	417	33.2	1.1	5	3.64	-397.9	1.05	
		Minimum	606965.3	2356715.9	0	310	1024	0	0	0.0	20.3	32	0.00	-382.8	6.49	
		25%	611671.8	2360596.0	25	2300	1923	0	0	12.2	20.9	400	3.41	179.0	7.49	
		50%	613509.0	2362750.0	90	3100	2590	14	1	65.5	21.6	766	7.00	312.2	7.89	
		75%	614951.6	2364150.7	225	4904	2600	58	47	221.4	23.2	4617	7.50	375.0	8.00	
		Maximum	621336.6	2369077.0	732	5700	2748	100	1000	241.7	27.0	44000	8.78	375.0	8.33	
Site	Copula Generative Adversarial Network	count	525000	525000	525000	525000	525000	525000	525000	525000	525000	525000	525000	525000	525000	525000
		mean	613554.2	2362506.8	67	2922	2289	1	0	27.1	22.2	1384	4.21	179.1	7.75	
		Stdev	1.0	1.0	6	2	1	174	455	31.4	1.1	5	3.83	-398.0	1.05	
		Minimum	606965.3	2356715.9	0	310	1024	0	0	0.0	20.3	32	0.00	-382.8	6.49	
		25%	611557.6	2360682.9	29	2437	1941	0	0	11.9	21.0	403	4.17	178.1	7.50	
		50%	613457.9	2362881.5	98	3105	2587	9	1	68.6	21.7	823	7.00	312.2	7.92	
		75%	614813.6	2364085.5	243	4934	2600	53	101	222.5	23.2	4657	7.49	375.0	8.00	
		Maximum	621336.6	2369077.0	612	5700	2694	100	1000	241.6	27.0	44000	8.77	375.0	8.33	
Site	Copula Generative Adversarial Network	count	695000	695000	695000	695000	695000	695000	695000	695000	695000	695000	695000	695000	695000	695000
		mean	613554.3	2362507.4	68	2922	2290	1	0	27.2	22.2	1383	4.21	178.5	7.75	
		Stdev	1.0	1.0	6	2	1	174	454	31.4	1.1	5	3.83	-398.0	1.05	
		Minimum	606965.3	2356715.9	0	310	1024	0	0	0.0	20.3	32	0.00	-381.6	6.49	
		25%	611567.5	2360681.6	29	2432	1938	0	0	12.0	21.0	403	4.19	177.9	7.50	
		50%	613457.2	2362883.4	98	3105	2587	9	1	69.0	21.7	820	7.00	312.2	7.92	
		75%	614808.7	2364085.2	243	4934	2600	53	102	222.5	23.2	4649	7.49	375.0	8.00	
		Maximum	621336.6	2369077.0	611	5700	2695	100	1000	241.6	27.0	44000	8.77	375.0	8.33	

3.4 Conceptual groundwater model

Based on a review of the validation metrics and summary statistical measures provided in the previous section, the preferred generative AI algorithm for the H-M aquifer is determined to be the CopulaGAN. Although the TVAE is preferred for estimating the confinement or unconfinement of the H-M aquifer. For this reason, the CopulaGAN is used to generate the synthetic set of stochastic H-M aquifer features as point clouds that are mapped to structured grid and called the Conceptual groundwater model. The one exception is for aquifer confinement. In this case, the TVAE is used to generate the synthetic set of stochastic H-M values for aquifer confinement that are mapped separately to the grid.

3.4.1. Mapping synthetic point clouds to the structured model grid

The final step in the AI-assisted workflow involves mapping the set of stochastic *site model* point clouds to nodes of the structured numerical groundwater model grid. The mapping of *site model* point clouds to grid nodes is performed using the two-phase SOM algorithm, resulting in a transdisciplinary representation of continuous and categorical aquifer features at each grid node. The development of a stochastic conceptual groundwater model on the structured grid involves the following workflow.

1. Site model realization: A site model realization is generated by applying the CopulaGAN to the reference model, producing synthetic point clouds of aquifer features.
2. Conceptual groundwater model realization: A self-organizing map (SOM) whose default grid size is applied to the site model realization to map the synthetic point clouds for each aquifer feature onto the nodes of the structured groundwater model grid.
3. Ensemble generation: Steps 1 and 2 are repeated to generate a statistically representative ensemble of conceptual groundwater models (N = 30).

4. Stochastic model construction: Stochastic conceptual groundwater models are produced by aggregating the ensemble results into cumulative distribution functions (CDFs) for each categorical and continuous aquifer feature at every grid node.
5. Feature selection and visualization: Aquifer features are extracted from their CDFs at selected percentiles for visualization, evaluation, and interpretation of individual three-dimensional categorical or continuous properties.

Each synthetic point cloud realization is mapped to the nodes of the structured groundwater model grid ($N=310,500$). Predicted categorical variables range from 0 to 1 (Fig. 9). Where predictions indicate multiple geologic units—reflecting uncertainty due to limited mutual information—the unit with a frequency greater than or equal to 0.5 is assigned, consistent with one-hot encoding. Empirical distribution functions for each aquifer feature are derived from the ensemble of realizations. The resulting CopulaGAN-based predictions provide spatially distributed stochastic representations of geologic units within and across the Hālawa–Moanalua aquifer. Percentile mapped voxels represent feature values extracted from the corresponding cumulative distribution functions computed from the realizations.

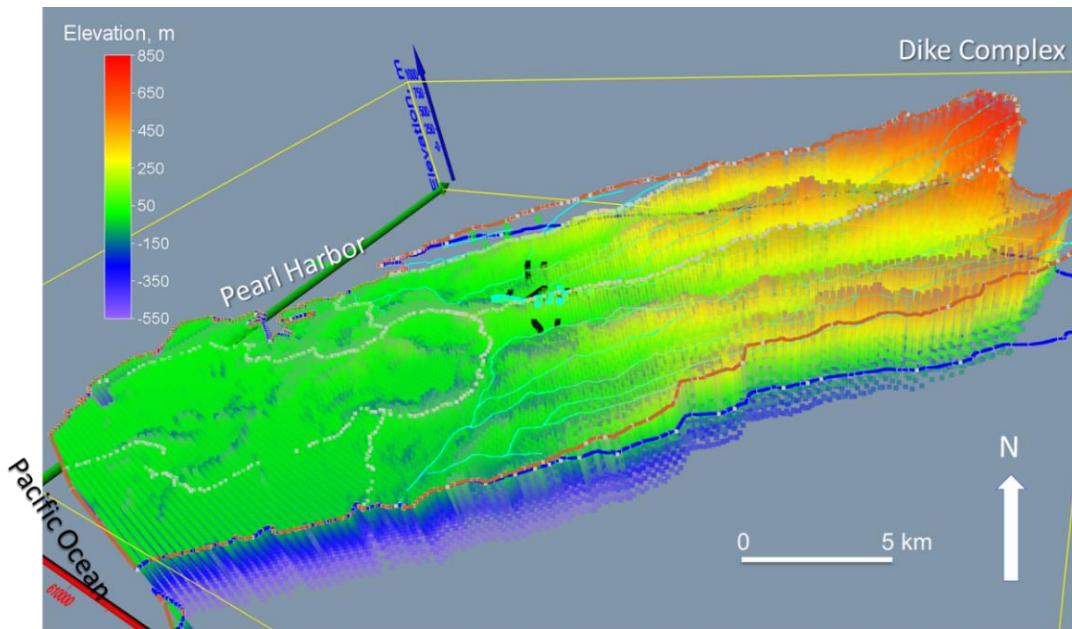


Fig. 9. The structured numerical model grid is constructed with 30 vertical layers and a horizontal resolution of $10\text{ m} \times 10\text{ m}$, resulting in a total of 310,500 nodes. Grid elevations are represented using a color scale, with warmer colors indicating higher elevations and cooler colors indicating lower elevations. The approximate locations of subregional features, including the dike complex, Pearl Harbor, and the Pacific Ocean, are also indicated.

The quality of geologic unit mapping from CopulaGAN-based point clouds to the structured Hālawa–Moanalua aquifer grid nodes are summarized in Table 11. The summary information includes the number of classified predictions by geologic unit (y-axis) as a function of deciles (x-axis). Inspection of this table reveals that the number of classified grid nodes for each geologic unit increases from the 10th percentile (minimum number) to the 90th percentile (maximum number). This behavior is characteristic of the cumulative distribution function meaning that the number of classified geologic units will always

decrease when selecting lesser percentiles. For example, the estimated number of grid nodes classified as pāhoehoe is 133,608 at the 10th percentile and 191,091 at the 90th percentile with a range of prediction uncertainty of 57,483 nodal classifications (difference between 90th and 10th percentiles).

Analysis of the total number of structured grid nodes and the number of classified geologic units at selected percentiles across all nodes provides useful context for assessing the point-cloud-to-grid mapping process. At the 10th, 50th, and 90th percentiles, the total number of classified (unclassified) nodes are 211,378 (99,122 or 32%), 274,918 (35,582 or 11%), and 358,753 (–48,253 or –16%), respectively. The difference in the absolute percentage of unclassified nodes between the 10th and 90th percentiles indicates a slight bias toward a preferred set of feature predictions above the 75th percentile. Negative unclassified values beyond the 75th percentile suggest that multiple classifications are being assigned to one or more grid nodes. This behavior indicates the need to reevaluate in future studies: (1) the one-hot encoding assignment for geologic unit frequency greater than (or equal) to 0.5, and (2) the SOM grid size and processing parameters as the number of generative estimates increases.

Table 11.

CopulaGAN-based stochastic predictions of geologic units across the Hālawa–Moanalua aquifer. Percentiles of geologic units reflect cumulative distributions functions computed from 30 realizations.

Geologic Unit	Percentile									
	10th	20th	30th	40th	50th	60th	70th	80th	90th	Average
Caprock	76540	84472	89159	93093	96500	99872	103603	108079	113904	96189
Saprolite	548	1024	1716	2345	3213	4228	5577	7963	12254	3081
Clinker Loose	0	0	0	0	6	150	374	1873	7956	6
Clinker Welded	1	319	667	1046	1457	1921	2507	3398	4885	1413
‘A‘ā	0	19	170	399	797	1331	2169	3992	6462	756
Pāhoehoe	133608	144598	154558	161928	166594	170810	175382	181056	191091	166399
Tuff	681	1922	3678	4947	6351	8088	10683	15070	22201	6246
Total classified	211378	232354	249948	263758	274918	286400	300295	321431	358753	274090
Total nodes	310500	310500	310500	310500	310500	310500	310500	310500	310500	310500
Unclassified nodes	99122	78146	60552	46742	35582	24100	10205	–10931	–48253	36410
Unclassified fraction	32%	25%	20%	15%	11%	8%	3%	–4%	–16%	12%
Relative classification	under	under	under	under	under	under	under	over	over	under

3.4.2 Stochastic 3D Hālawa–Moanalua aquifer features

In this section, selected aquifer features are evaluated at specified percentile levels and compared with published geologic maps and hydrogeologic observations. Both categorical and continuous variables are examined using values extracted at representative percentiles to assess agreement between sampled observations and model predictions. As an illustrative example, sampled surface geology is compared with geologic units estimated from the conceptual groundwater model (Fig. 10), which contrasts the field-sampled surface geology (Fig. 10a) with the estimated conceptual geologic model at the 70th percentile (Fig. 10b). The field-sampled geologic maps, compiled from Hunt (1996) and Sherrod et al. (2021), are published as aggregated units: the upper section includes pāhoehoe, ‘a‘ā, and alluvium; the middle section includes tuff, caprock, and alluvium; and the lower section includes caprock and fill. Overall, the field-sampled surface geology is broadly consistent with the CopulaGAN-estimated surface geologic units

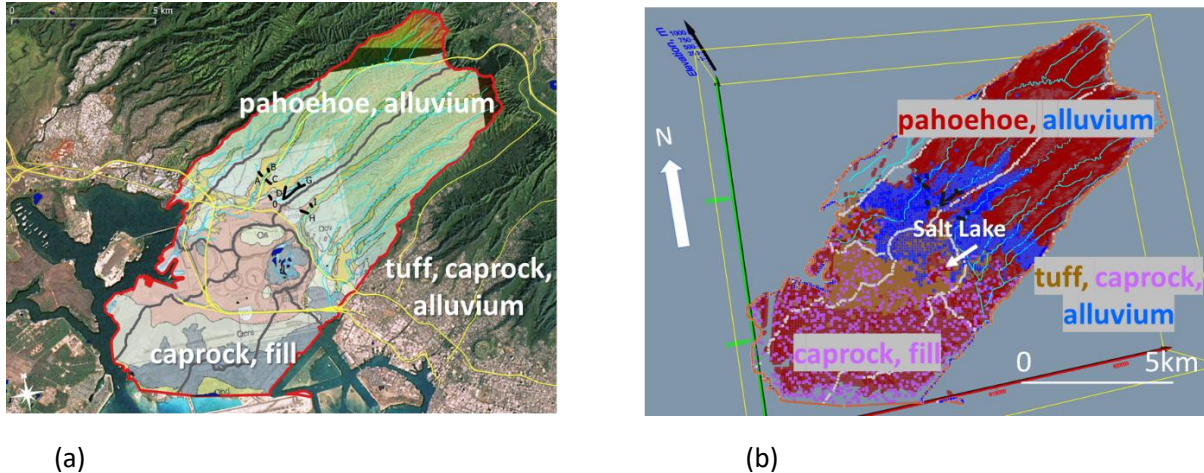


Fig. 10. Comparison of field sampled and estimated surface geologic units at the Hālawa-Moanalua aquifer. (a) Published field sampled surface geologic maps (Hunt, 1996; Sherrod et al., 2021). (b) CopulaGAN estimated surface geologic units (60th percentile). Caprock (magenta) reflects 1% of the available to visualize alluvium (blue), tuff (brown) and pāhoehoe (red).

In a related analysis, CopulaGAN-derived estimates of geologic units across the Hālawa–Moanalua aquifer are shown at the 50th, 60th, 70th, and 80th percentiles (Fig. 11). For clarity, alluvium (royal blue) is excluded, and caprock (magenta) is displayed at a reduced density corresponding to a random 1% subset of the total estimated locations. Visual inspection of these plots suggests a systematic increase in the spatial extent of several geologic units with increasing percentile, most notably saprolite (lime green) and tuff (brown). The expanded spatial extent of tuff at higher percentiles corresponds to delineation of the Salt Lake feature in the eastern portion of the tuff cone. Although the overall locations of the geologic unit features generally appear consistent with existing geologic interpretations, the occurrence of saprolite within the Salt Lake cone deviates from current understanding. This feature becomes more pronounced at the 80th percentile and is therefore interpreted as a modeling artefact, potentially related to limitations in the one-hot encoding assignment and/or the SOM mapping parameters.

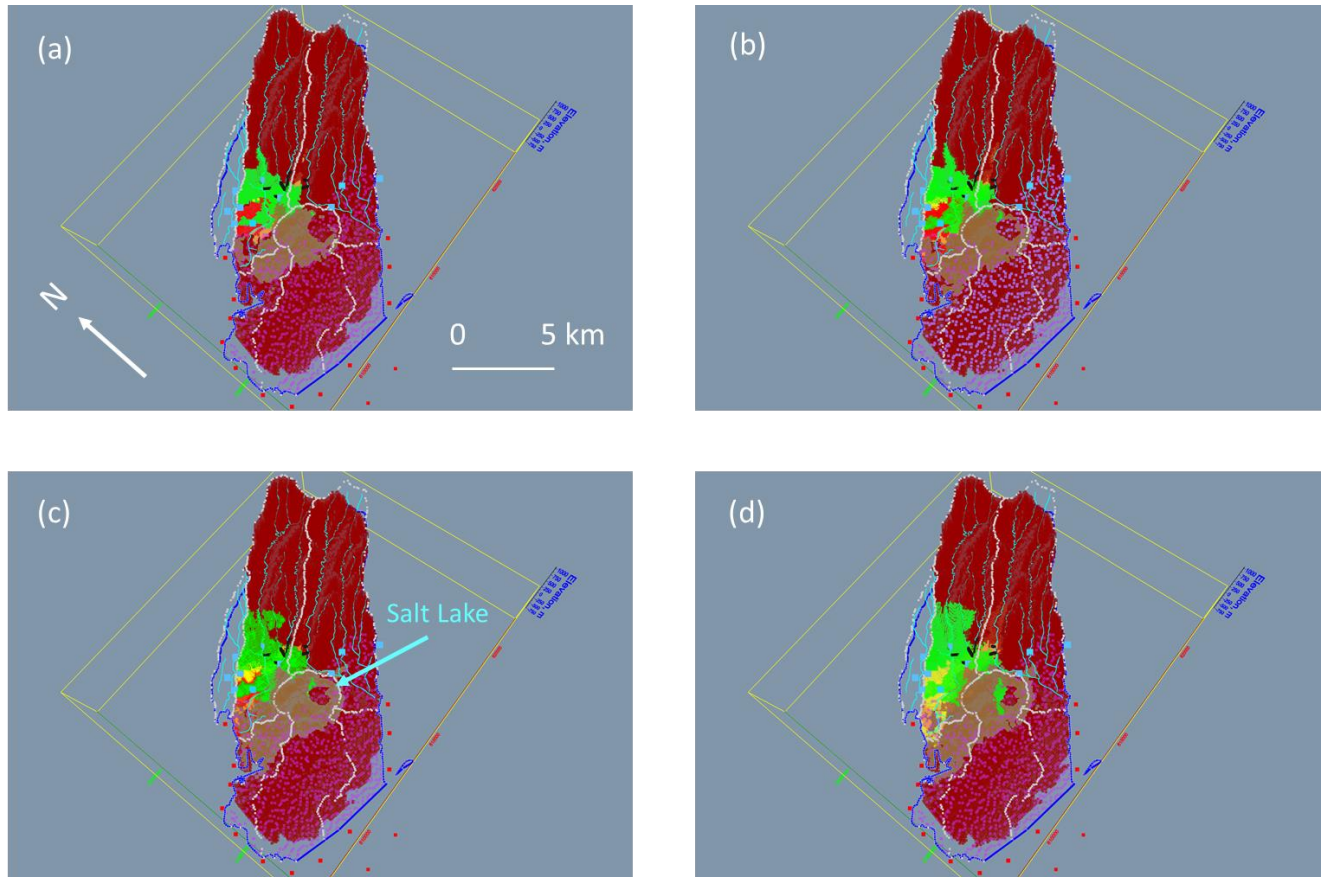
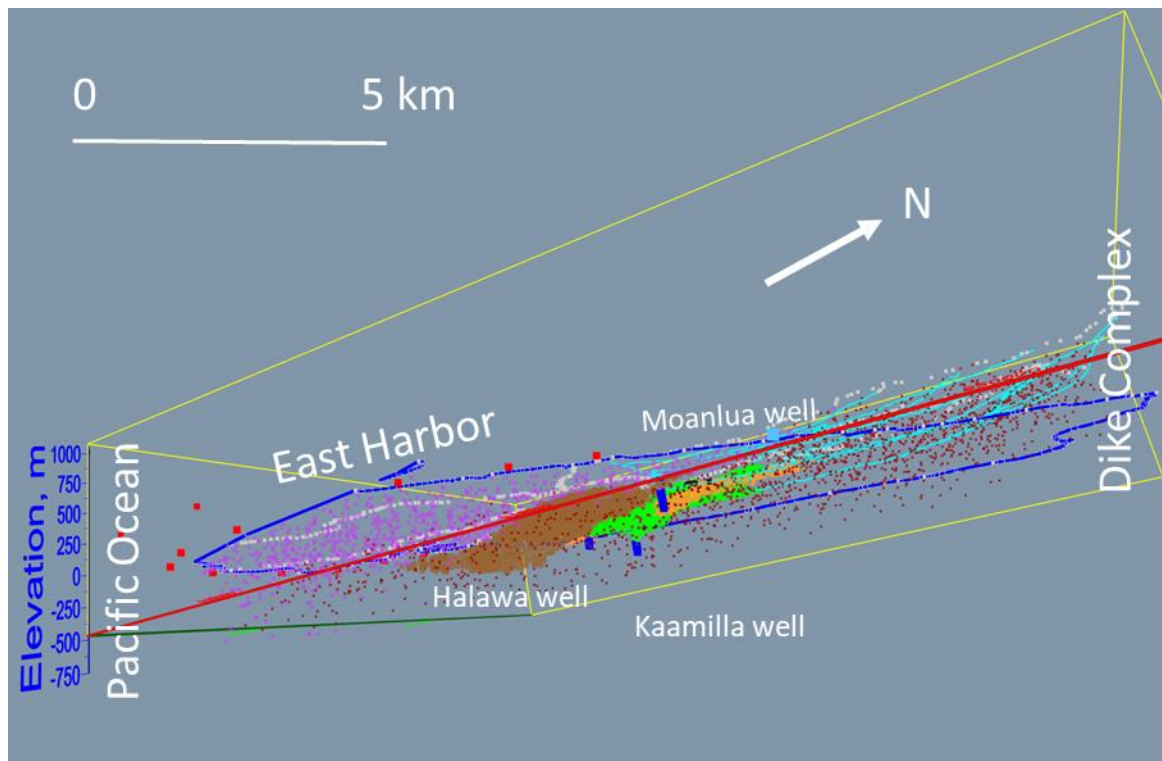
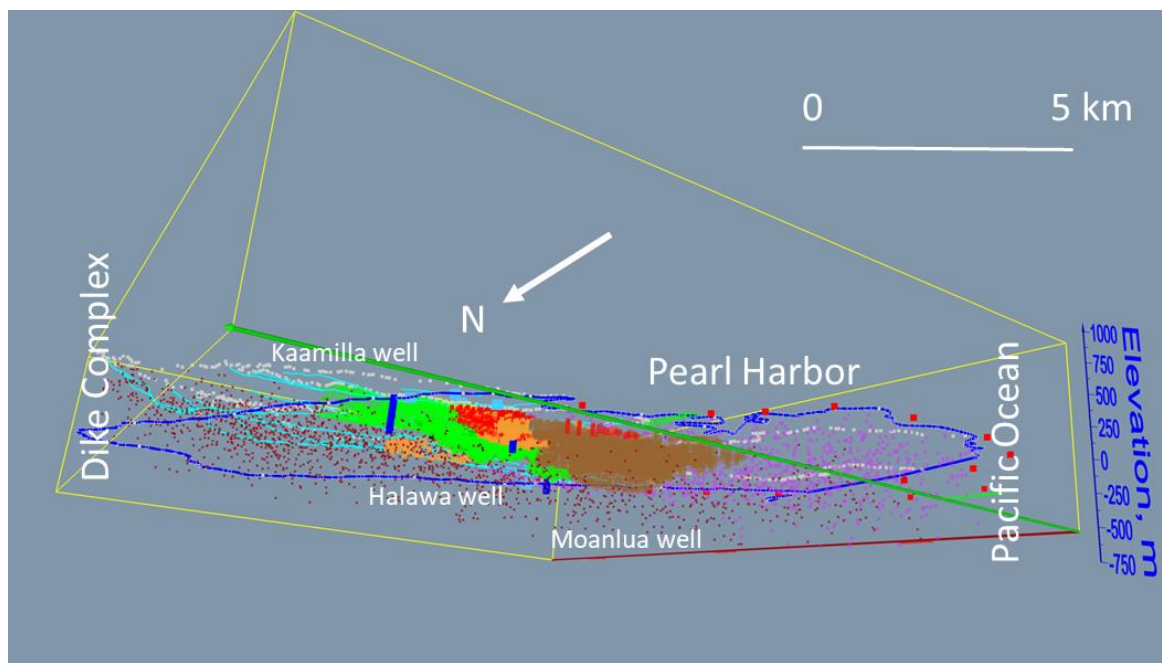


Fig 11. Top view of the CopulaGAN 3D geologic unit estimates (fake) across the Hālawa-Moanalua aquifer. Units: 'a'ā (orange), alluvium (royal blue), caprock - 1% of total (magenta), saprolite (lime green), clinker-loose (yellow), clinker-welded (red), pāhoehoe (brick red), tuff (brown), (a) 50th percentile, (b) 60th percentile, (c) 70th percentile, (d) 80th percentile. Notice that the area of geologic units enlarges with increasing percentile. The alluvium is removed to highlight spatial changes in the geologic unit predictions. The black lines appearing in the saprolite (green) indicate the locations of seismic refraction and reflection profiles, and blue squares are supply wells. The location of Salt Lake appears at the center of the tuff cone directly overlying the undifferentiated pāhoehoe lava.



(a)



(b)

Fig. 12. Side-view perspective looking upward toward the estimated (synthetic) geologic units across the Hālawa–Moanalua aquifer. Geologic units include 'a'a (orange), caprock (magenta; ~1% of total), saprolite (lime green), clinker–loose (yellow), clinker–welded (red), pāhoehoe (brick red, ~1% of total),

and tuff (brown). (a) East–west view. (b) West–east view. Vertical blue lines are deep monitoring wells. Red squares are harbor nodes overlying seawater.

Field-sampled aquifer conditions are compared with TVAE-estimated conditions at the 70th percentile in Fig. 13. This comparison provides an independent assessment of the CGM's ability to reproduce the spatial distribution of the unconfined/unsaturated zone (white) and the confined/saturated zone (dark blue). Reference data include depth-to-water measurements (light blue squares) collected at monitoring well locations (red squares), surface projections of seismic profiles (black lines), and area monitoring wells (red squares). The figure panels include: (a) a plan view showing water-related features (Fig. 13a), (b) a cross-sectional view illustrating water-related features (Fig. 13b), and (c) a plan view combining water and geologic unit features (Fig. 13c), including clinker welded (dark orange), clinker loose (yellow), 'a'a lava (orange), saprolite (bright green), and alluvium overlying the seismic profiles (royal blue).

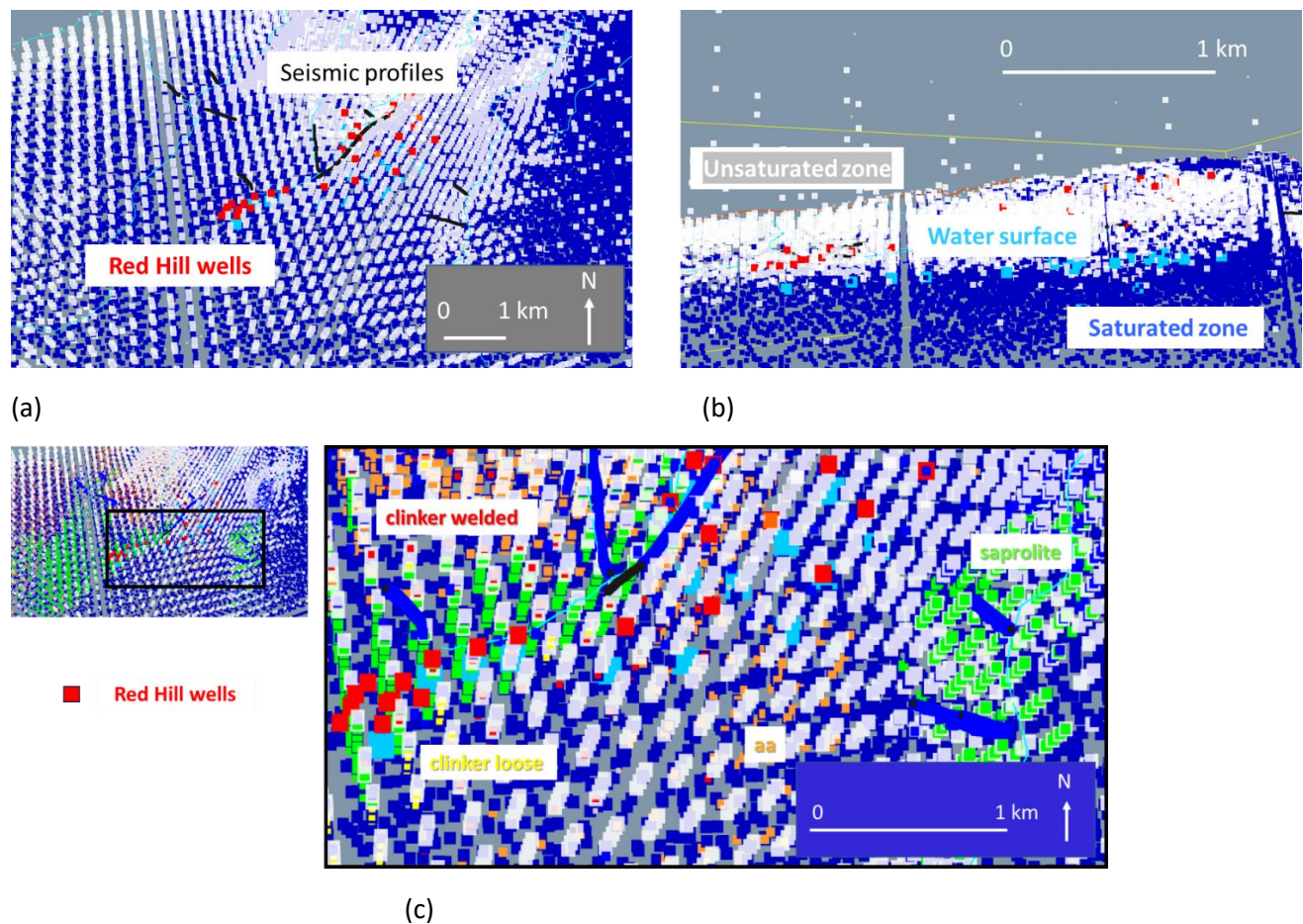


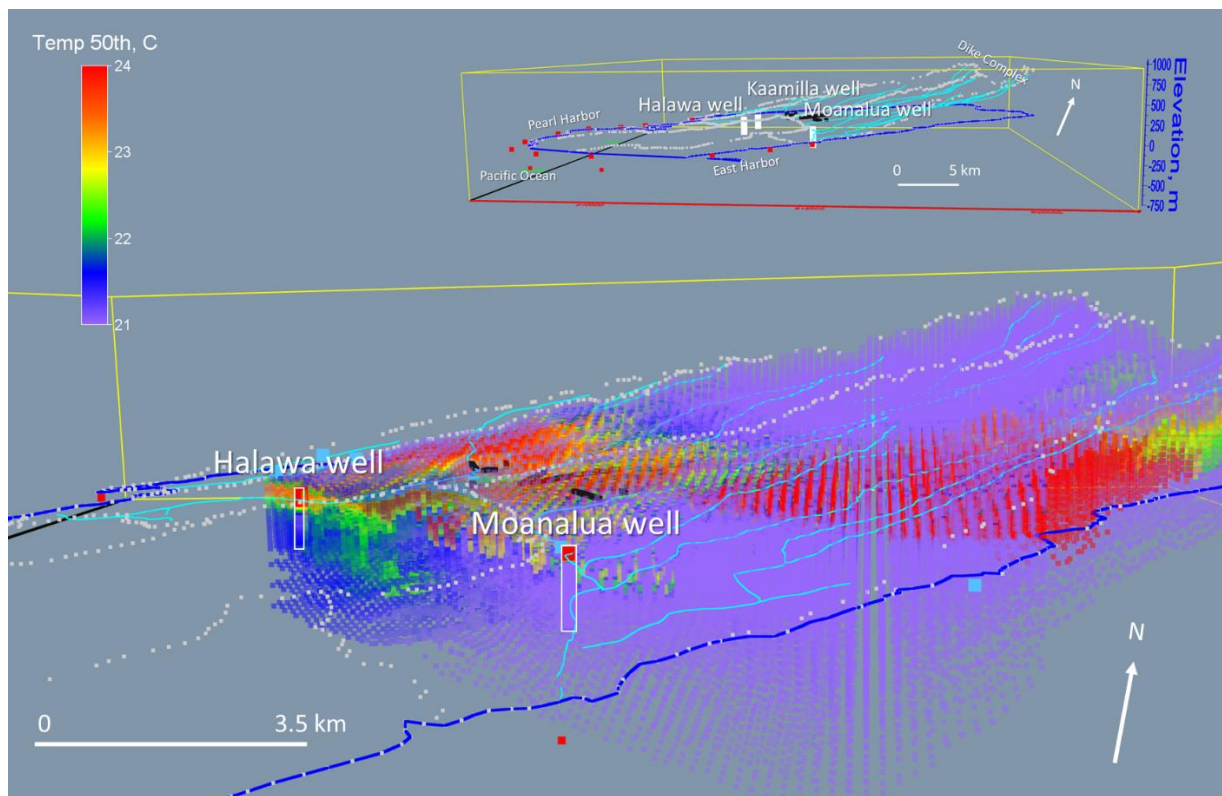
Fig. 13. Comparison of field-sampled aquifer conditions with TVAE-estimated conditions at the 70th percentile. Panels show (a) plan view of unconfined/unsaturated (white) and confined/saturated (dark blue) zones with reference water data, (b) cross-sectional view of water features, and (c) plan view combining water and geologic unit features. Reference data include depth-to-water measurements at monitoring wells (light blue squares), monitoring well locations (red squares), and surface projections of seismic profiles (black lines). Geologic units include clinker welded (dark orange), clinker loose (yellow), 'a'a lava (orange), saprolite (bright green), and alluvium overlying seismic profiles (royal blue).

Next, aquifer temperature and conductance were evaluated at the 50th and 75th percentiles to examine spatial variability and overall model behavior. Overall, the estimated temperature and conductance values show good agreement with observations from the deep Hālawa and Moanalua monitoring wells (Board of Water Supply, 2023). This agreement suggests that the modeled distributions provide a reasonable representation of subsurface conditions across the study area. Differences between percentiles are generally small and localized, indicating limited sensitivity of the model to the chosen percentile.

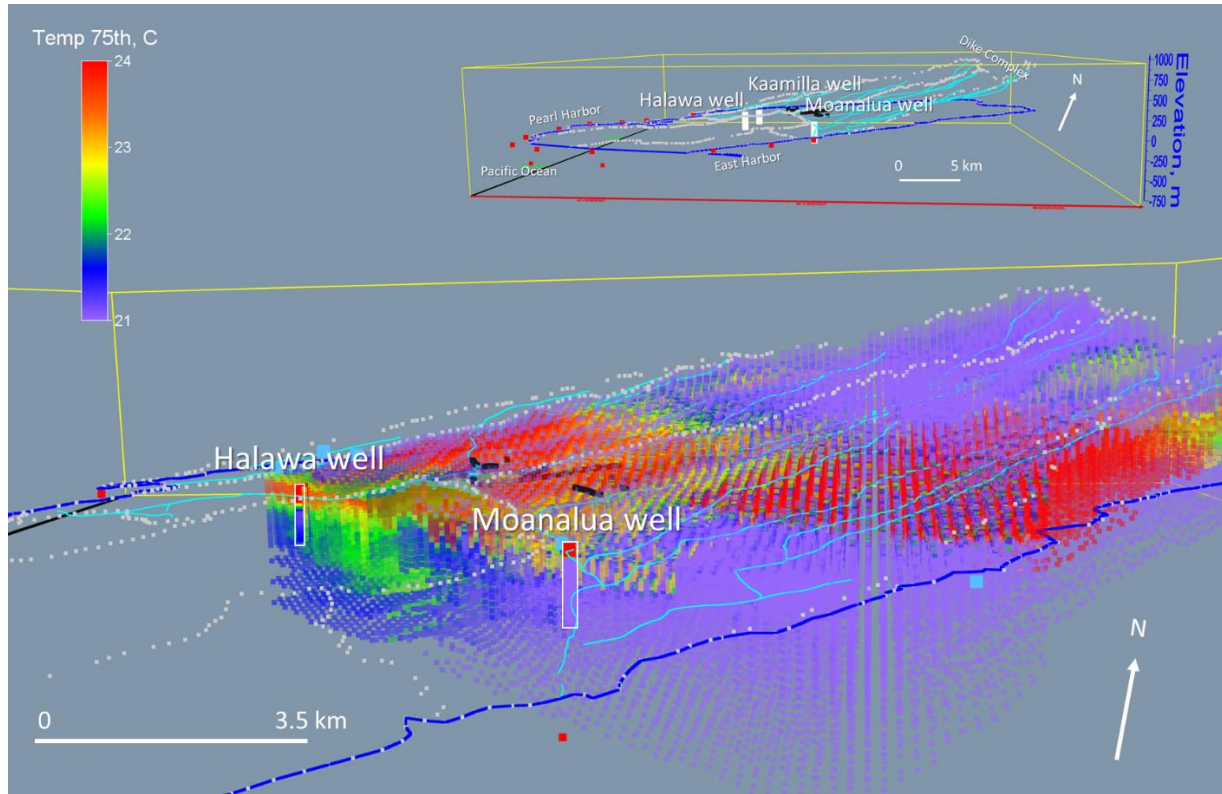
Minor temperature differences between the 50th and 75th percentiles are observed in the lower half of the Hālawa well and extend laterally toward the Moanalua well. These differences correspond to temperature increases of approximately 0.5 °C, as indicated by a color shift from royal blue to green in the percentile comparison plots. Despite these localized variations, the overall temperature structure remains consistent between percentiles, demonstrating stability in the modeled thermal profile across the aquifer.

Similarly, minor changes in conductance are evident between the gridded percentile estimates. Slight increases occur beneath the Hālawa and Moanalua wells and east of the Moanalua well when moving from the 50th to the 75th percentile. Conductance values rise from approximately 5,000 $\mu\text{S}/\text{cm}$, indicative of freshwater, to about 12,500 $\mu\text{S}/\text{cm}$, representative of brackish conditions, with the changes reflected by a color shift from royal blue to green in the plots. These variations are localized but consistent with the overall spatial trends observed in the aquifer.

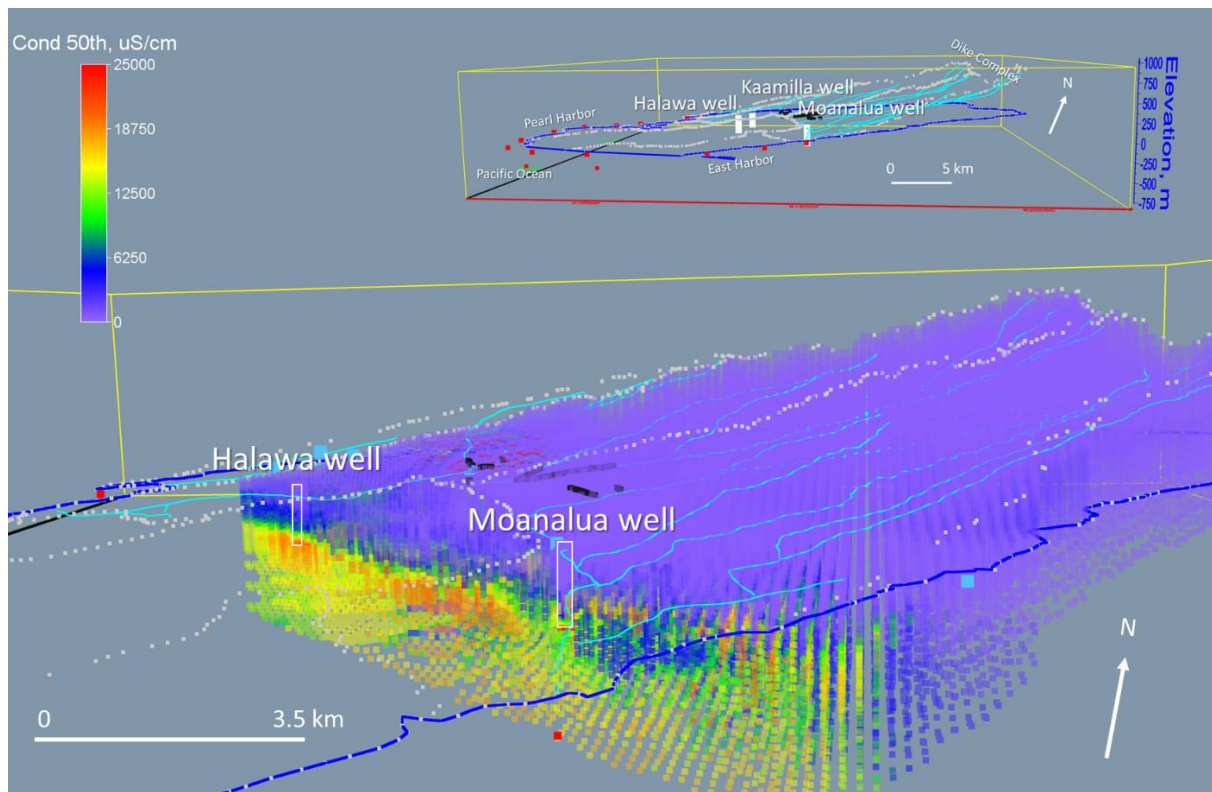
Farther east in the model domain, conductance also increases when comparing the 50th and 75th percentile plots. Overall, the spatial patterns of temperature and conductance remain very similar between percentiles and closely match the estimated conditions surrounding the Hālawa and Moanalua wells. This consistency suggests that the choice of percentile does not substantially alter the interpretation of aquifer conditions. However, because some grid nodes remain unclassified at the 50th percentile while all nodes are classified at the 75th percentile (Table 11), the following section focuses on interpreting three-dimensional conductance plots in the context of freshwater, seawater, and their exchange.



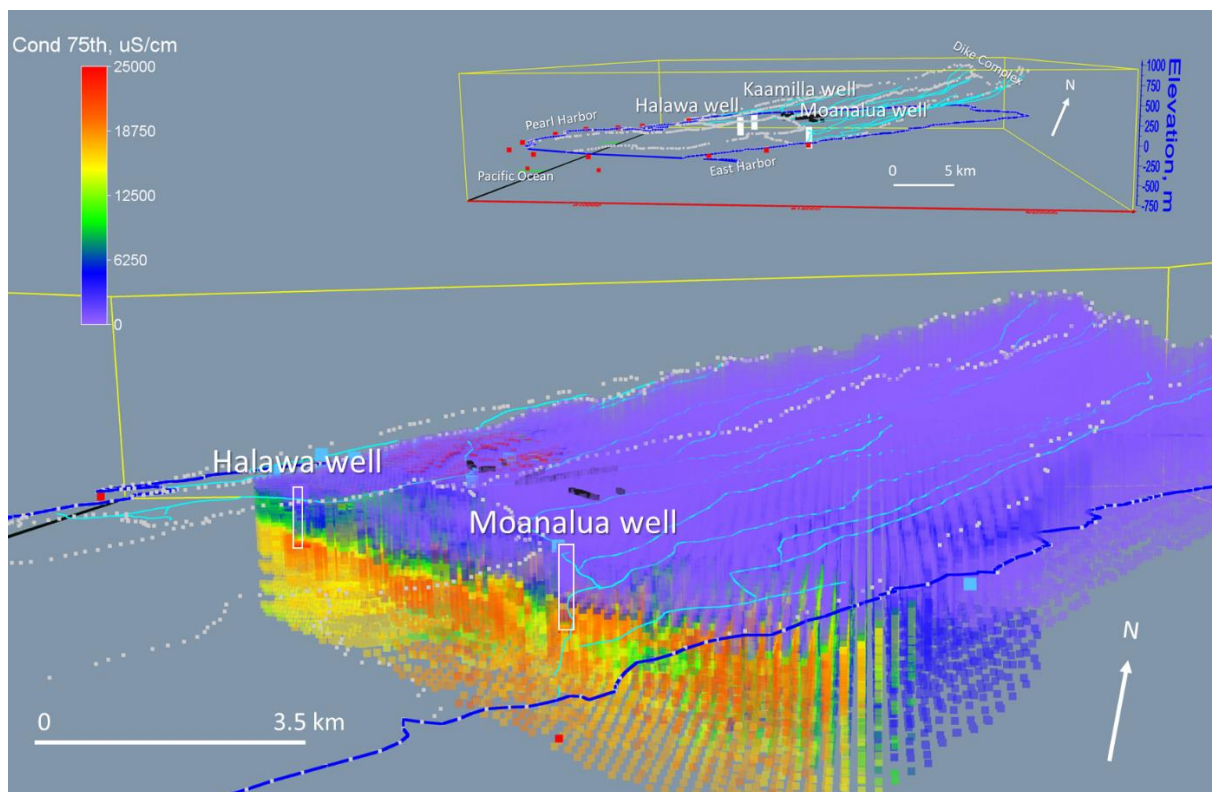
(a)



(b)



(c)



(d)

Fig 14. CopulaGAN-derived estimates of aquifer temperature and conductance compared with measured profiles from the Hālawa and Moanalua deep monitoring wells (outlined in white). Panels show (a) median (50th percentile) temperature, (b) 75th percentile temperature, (c) median (50th percentile) conductance, and (d) 75th percentile conductance. Model grid surface elevations and depths at the Hālawa and Moanalua wells are approximately 18.1 m / 650 m and 10.8 m / 650 m, respectively. The inset shows the locations and depths of the monitoring wells relative to the Hālawa and Moanalua aquifer. Streams are indicated by light blue lines, and ocean nodes by red squares.

The three-dimensional groundwater conductance model is evaluated using the 75th percentile of CopulaGAN continuous-feature estimates. On-land conductance values across the Hālawa–Moanalua aquifer span nearly four orders of magnitude, from \sim 100 $\mu\text{S}/\text{cm}$ (low-conductance freshwater) to \sim 25,000 $\mu\text{S}/\text{cm}$ (high-conductance saline water, \sim 50% of seawater conductivity). This range provides a quantitative basis for delineating freshwater, brackish, and saline zones, as well as areas of freshwater–seawater exchange, reflecting lithologic heterogeneity, structural controls, and hydraulic gradients.

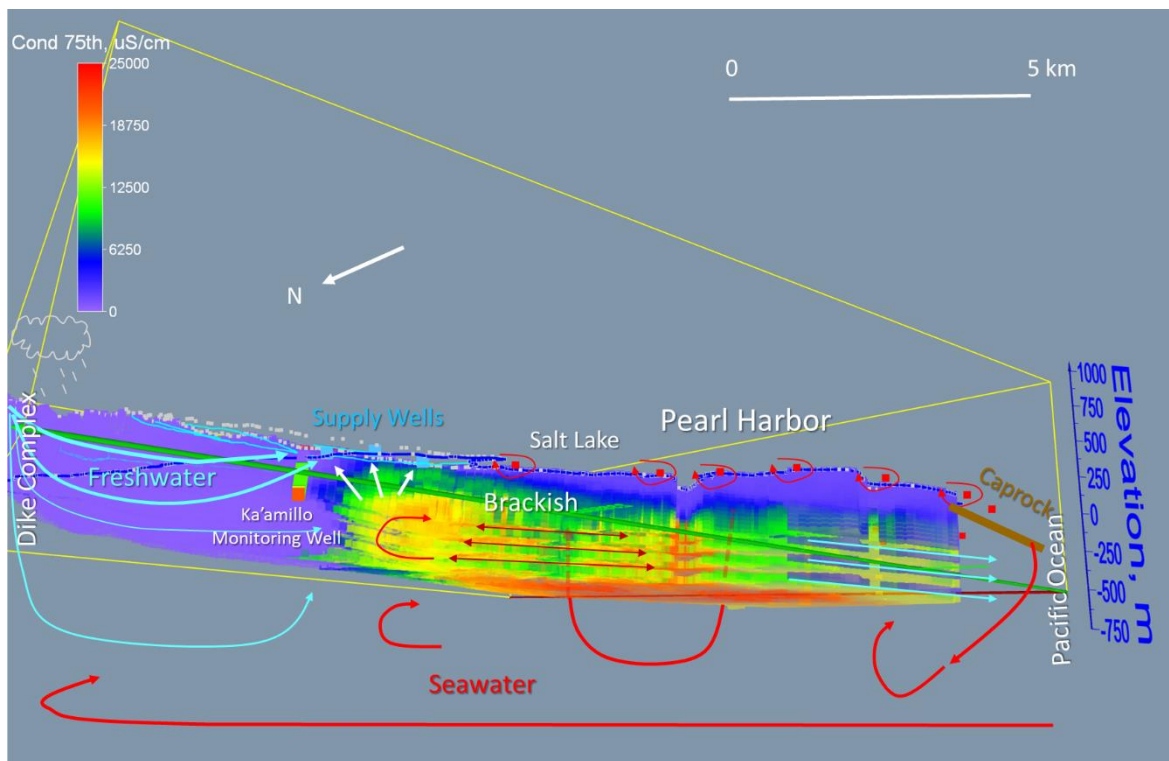
Low-conductance groundwater associated with the northern dike complex flows downgradient toward the major supply wells. Freshwater exhibits density-dependent behavior near the wells, particularly along upslope aquifer margins and north of both harbors (Figs. 15a, c). Pumping appears to capture both dike-derived freshwater and brackish water from adjacent mixing zones, consistent with lateral inflow and vertical density stratification. This suggests that well operations influence local salinity distributions and enhance freshwater–brackish water interactions.

Freshwater discharge is inferred along the western aquifer margin, where preferential pathways through undifferentiated pāhoehoe units appear to convey groundwater directly to the Pacific Ocean below Pearl Harbor (Fig. 15b). These pathways, oriented roughly perpendicular to the coastline, bypass the supply wells and likely represent a previously underrecognized component of the regional water budget. East of this discharge zone, seawater intrusion appears to occur along parallel, depth-dependent pathways, indicating structural or lithologic control on flow.

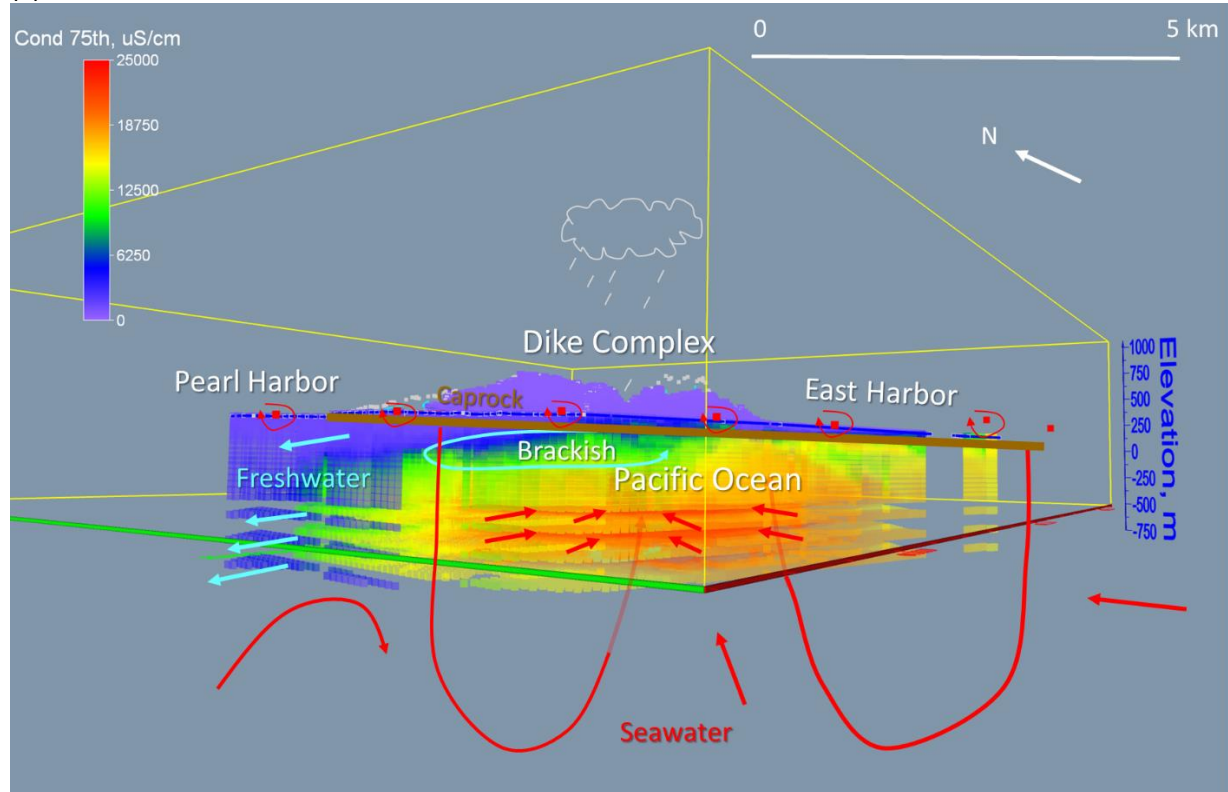
Conductance at the base of the aquifer supports freshwater north of the wells, with values increasing downgradient toward the ocean. The vertical transition from freshwater to brackish and saline water is consistent with coastal mixing processes. Highest conductance occurs beneath the Salt Lake Tuff cone (Fig. 11c), where pāhoehoe replaces the tuff cone center, providing a preferential pathway for seawater intrusion. The spatial coincidence of elevated conductance and lithologic change supports focused seawater transport and discharge.

Across uplands and ridges, conductance varies, but it remains relatively uniform beneath river channels (Fig. 15d), suggesting limited hydraulic connection between rivers and the basal aquifer. Potentiometric surfaces (Fig. 12) further support this interpretation. Conductance values consistent with seawater (\sim 44,000 $\mu\text{S}/\text{cm}$) are observed only at harbor nodes, indicating localized intrusion.

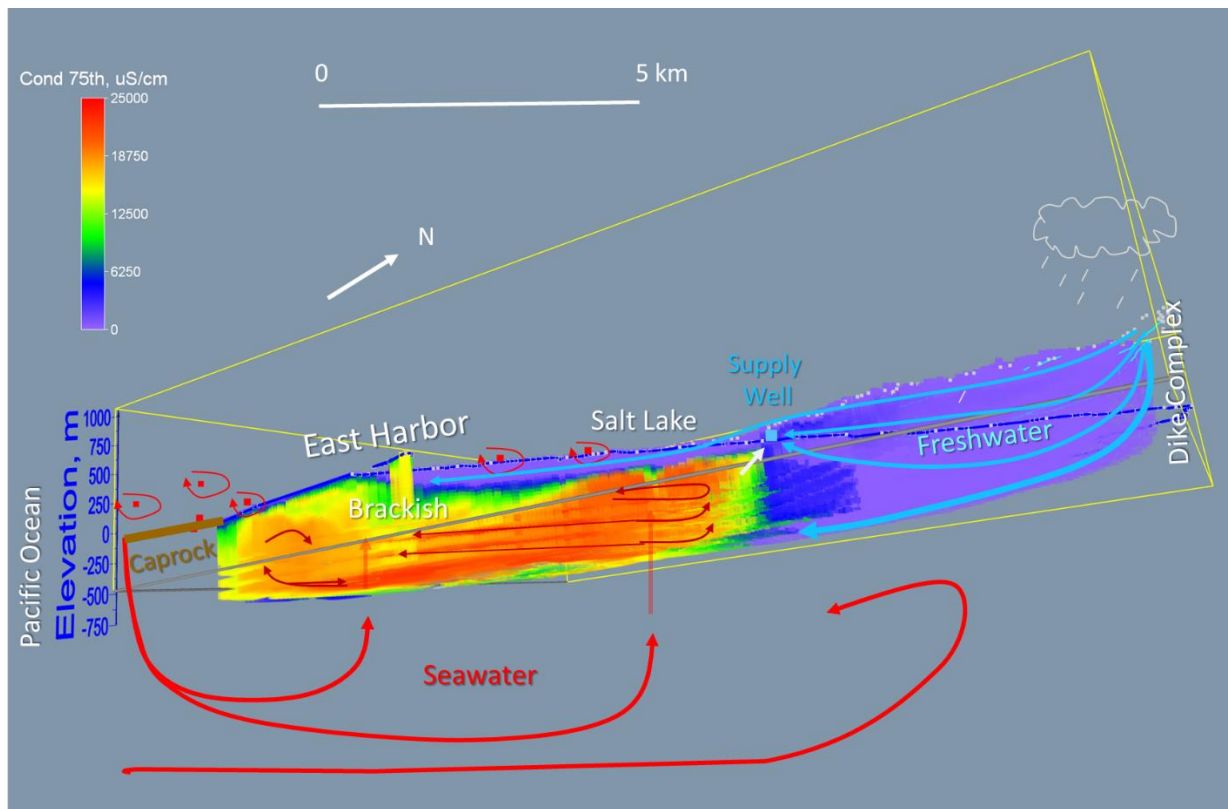
Beyond conductance, the CGM framework can represent additional continuous features, including geophysical (velocity, density), engineering (fracture rate, rock quality), and water-quality parameters (dissolved oxygen, redox potential, pH). Hydraulic properties governing flow (hydraulic conductivity, specific storage, specific yield) and transport (bulk density, dispersivity, porosity) can also be mapped to CGM grid nodes via the SOM. This approach will enable application of boundary conditions and calibration of numerical models for simulating freshwater–seawater exchange within the Hālawa–Moanalua aquifer.



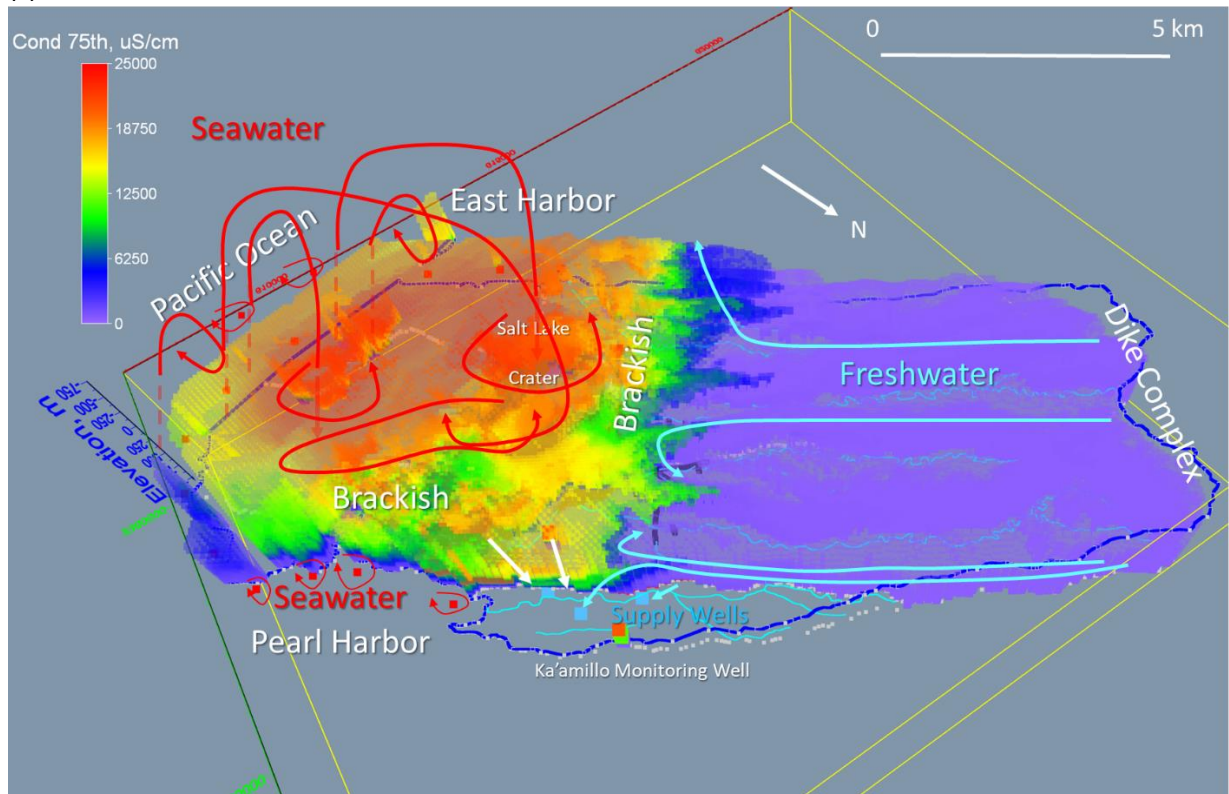
(a)



(b)



(c)



(d)

Fig 15. CopulaGAN estimates of conductance (Cond) revealing freshwater-seawater exchange across the Hālawa-Moanalua aquifer. (a) west to east view, (b) north to south view, (c), east to west view, and (d) bottom to top view (dike complex is along the northern boundary and Pacific Ocean along the southern boundary). The red squares represent nodes located in both harbors and the Pacific Ocean.

4. Conclusions

This study demonstrates that integrating unsupervised machine learning with generative artificial intelligence provides a robust framework for characterizing Pacific volcanic groundwater systems using sparse and highly imbalanced data. Among the methods evaluated, the Copula Generative Adversarial Network (CopulaGAN) was statistically preferred for developing the conceptual groundwater model (CGM) of the Hālawa–Moanalua aquifer, O’ahu, Hawai’i. For groundwater-level estimation, the Tabular Variational Autoencoder (TVAE) performed best, producing geologic unit representations comparable to those generated by CopulaGAN and the Tabular Gaussian Copula. These results highlight the value of applying multiple generative approaches to improve CGM robustness for complex coastal volcanic aquifers.

CopulaGAN-generated three-dimensional aquifer features reproduce published surface geologic maps and show strong agreement with observed conductance, temperature, and barometric pressure profiles. Conductance models indicate groundwater flow and discharge are influenced by regional hydraulic gradients, pumping, and seawater intrusion, as well as preferential pathways for freshwater–seawater exchange. Key hydrogeologic processes captured by the models include freshwater transport from dike complexes through pāhoehoe lava to slope transitions, submarine discharge along linear pathways to the Pacific Ocean, and landward seawater intrusion along southern and deep flow paths toward the Salt Lake crater.

Beyond conductance, the CGM framework can incorporate additional geophysical, engineering, and water-quality parameters, as well as hydraulic and transport properties, enabling future mapping, calibration, and simulation of aquifer dynamics. Overall, the CopulaGAN approach demonstrates strong potential for integrating sparse data, resolving aquifer heterogeneity, and supporting quantitative assessments of freshwater–seawater exchange. These findings provide critical insight for water-resource management, highlighting zones of active mixing, preferential flow, and localized seawater intrusion that may influence both supply-well performance and regional groundwater sustainability. The workflow is transferable to other Pacific-island aquifers and broader subsurface applications in the energy, mineral, and water-resource sectors.

CRediT authorship contribution statement

Michael J. Friedel: Writing – Original draft, Review & editing, Software, Methodology, Conceptualization, and Funding acquisition.

Declaration of competing interest

The authors declare that they have no known competing financial interests or personal relationships that could have appeared to influence the work reported in this paper.

Acknowledgments

This research was supported by a U.S. Navy grant (contract # 6112062-02) during the authors' appointment as Associate Researcher at the Research Corporation of the University of Hawai'i. The author gratefully acknowledges Drs. Donald Thomas, Erin Wallin, Peter Kannberg, and Toomas Parratt for their valuable support and contributions.

Data availability

Data will be made available on request.

References

Adombi, A.D.P., Chesnaux, R., Boucher, M.-A., Braun, M., Lavoie, J. 2024. A causal physics-informed deep learning formulation for groundwater flow modeling and climate change effect analysis. *Journal of Hydrology*, 637, 131370. <https://doi.org/10.1016/j.jhydrol.2024.131370>

Adams, E.E., Gelhar, L.W. 1992. Field study of dispersion in a heterogeneous aquifer: 2. Spatial moments analysis. *Water Resources Research*, 28(12), 3293–3307.

Alshehri, F., Abdelrahman, K. 2022. Groundwater aquifer detection using the time-domain electromagnetic method: A case study in Harrat Ithnayn, northwestern Saudi Arabia. *Journal of King Saud University – Science*, 34(1), 101684. <https://doi.org/10.1016/j.jksus.2021.101684>

Arndt, C., Blakemore, M., Nagler, T. 2020. Dependence modeling in hydrology using copulas. *Journal of Hydrology*, 582, 124521.

Attias, E., Thomas, D., Sherman, D., Ismail, K., Constable, S. 2020. Marine electrical imaging reveals novel freshwater transport mechanism in Hawai'i. *Science Advances*, 6(48), eabd4866. <https://doi.org/10.1126/sciadv.abd4866>

Ahmed, I., Coz, M., Jalludin, M., Sardini, P., Razack, M. 2018. Assessment of groundwater resources in a complex volcanic reservoir with limited data sets in a semi-arid context using a novel stochastic approach: The Goda Volcanic Massif, Republic of Djibouti. *Journal of Water Resource and Protection*, 10, 106–120. <https://doi.org/10.4236/jwarp.2018.101007>

Baud, B., Lachassagne, P., Dumont, M., Toulier, A., Hendrayana, H., Fadillah, A., Dorfliger, N. 2024. Review: Andesitic aquifers—hydrogeological conceptual models and insights relevant to applied hydrogeology. *Hydrogeology Journal*, 32, 1259–1286. <https://doi.org/10.1007/s10040-024-02784-0>

Billy, J., Reninger, P.-A., Raingeard, A., Chaumillon, E., Bouvier, C. 2022. Airborne electromagnetics as a tool to image the land-to-sea sedimentary continuum: A complementary geophysical approach to improve coastal characterization. *Marine Geology*, 454, 106945. <https://doi.org/10.1016/j.margeo.2022.106945>

Bonacci, O., Roje-Bonacci, T. 1997. Sea water intrusion in coastal karst springs: Example of the Blaž spring (Croatia). *Hydrological Sciences Journal*, 42(1), 89–100.

Borzi, I. 2025. Modeling groundwater resources in data-scarce regions for sustainable management: Methodologies and limits. *Hydrology*, 12, 11. <https://doi.org/10.3390/hydrology12010011>

Brandes, H.G., Robertson, I.N., Johnson, G.P. 2011. Soil and rock properties in a young volcanic deposit on the island of Hawai'i. *Journal of Geotechnical and Geoenvironmental Engineering*, 137(6), 597–610.

Bücker, C.J., Cashman, K.V., Planke, S. 1999. Data report: Physical and magnetic characterization of 'Aā and pahoehoe flows: Hole 990A1. In H.C. Larsen, R.A. Duncan, J.F. Allan, K. Brooks (Eds.), *Proceedings of the Ocean Drilling Program, Scientific Results*, Vol. 163. Ocean Drilling Program.

Carrasco-García, J., Porras-Sanchiz, D., Carrasco-García, P., Herrero-Pacheco, J.L., Martín-Nieto, I., Benito-Herrero, J.M., Huerta-Hurtado, P. 2022. Time-domain electromagnetics as a geophysical tool in hydrogeological exploitation projects in Mesozoic formations. *Applied Sciences*, 12(17), 8655. <https://doi.org/10.3390/app12178655>

Comte, J.-C., Wilson, C., Ofterdinger, U., González-Quirós, A. 2017. Effect of volcanic dykes on coastal groundwater flow and saltwater intrusion: A field-scale multiphysics approach and parameter evaluation. *Water Resources Research*, 53, 2171–2198. <https://doi.org/10.1002/2016WR019480>

Custodio, E. 2007. Groundwater in volcanic hard rocks. In *Groundwater in Fractured Rocks*, Taylor & Francis, Milton Park, pp. 95–108.

Custodio, E. 2010. Groundwater development in volcanic rock aquifers. *Hydrogeology Journal*, 18, 301–313.

Dankar, F., et al., 2025. *KS Complement metric for tabular data similarity assessment*. In: SDMetrics – Synthetic Data Metrics Library documentation. <https://docs.sdv.dev/sdmetrics/metrics/quality-metrics/kscomplement> (accessed 7 January 2026).

Dentz, M., le Borgne, T., Englert, A., Bijeljic, B. 2011. Mixing, spreading and reaction in heterogeneous media: A brief review. *Journal of Contaminant Hydrology*, 120, 1–17.

Dumont, M., Reninger, P.A., Aunay, B., Pryet, A., Jougnot, D., Join, J.L., Michon, L., Martelet, G. 2021. Hydrogeophysical characterization in a volcanic context from local to regional scales combining airborne electromagnetism and magnetism. *Geophysical Research Letters*, 48(12), e2020GL092000. <https://doi.org/10.1029/2020GL092000>

El Bilali, A., Taleb, A., Nafii, A., Alabjah, B., Mazigh, N. 2021. Prediction of sodium adsorption ratio and chloride concentration in a coastal aquifer under seawater intrusion using machine learning models. *Environmental Technology & Innovation*, 23, 101641. <https://doi.org/10.1016/j.eti.2021.101641>

Fathani, T.F., Salaamah, A.F., Wilopo, W. 2018. Correlation of P-wave velocity with rock quality designation (RQD) in volcanic rocks. *Journal of Hydrology*, 3(2). <https://doi.org/10.22146/jag.48594>

Finstik, S.A. 1998. Subsurface geology and hydrogeology of downtown Honolulu, Hawai'i, with engineering and environmental implications. Water Resources Project Report PR-99-05. <https://scholarspace.manoa.Hawaii.edu/handle/10125/1989>

Friedel, M.J., Buscema, M. 2023. Multiphysics-decision tree learning for efficient variably saturated subsurface transport parameter estimation with improved accuracy. arXiv:2312.10213.

<https://doi.org/10.48550/arXiv.2312.10213>

Friedel, M.J., Lautz, N., Wallin, E., Gritto, R., Bonneville, A., Buscema, M., Martel, S. 2023. Multimodal machine learning for 3-dimensional characterization of hidden groundwater and geothermal resources: Case study, island of Hawai'i. arXiv:2312.16194. <https://doi.org/10.48550/arXiv.2312.16194>

Friedel, M.J. 2016. Estimation and scaling of hydrostratigraphic units: Application of unsupervised machine learning and multivariate statistical techniques to hydrogeophysical data. *Hydrogeology Journal*, 24, 2103–2122. <https://doi.org/10.1007/s10040-016-1452-5>

Geng, X., Michael, H.A. 2020. Preferential flow enhances pumping-induced saltwater intrusion in volcanic aquifers. *Water Resources Research*, 56, e2019WR026390.

<https://doi.org/10.1029/2019WR026390>

Geng, X., Michael, H.A. 2021. Along-shore movement of groundwater and its effects on seawater-groundwater interactions in heterogeneous coastal aquifers. *Water Resources Research*, 57, e2021WR031056. <https://doi.org/10.1029/2021WR031056>

Gingerich, S.B., Engott, J.A., 2012. Groundwater availability in the Hawai'ian Islands. *U.S. Geological Survey Scientific Investigations Report 2012-5098*, Reston, Virginia, USA.

Goodfellow, I., Pouget-Abadie, J., Mirza, M., et al. (2014). *Generative adversarial nets*. Advances in Neural Information Processing Systems, 27.

Google Developers, 2025. *One-hot encoding*. Available at: <https://developers.google.com/machine-learning/crash-course/categorical-data/one-hot-encoding> [Accessed 17 December 2025].

Ghiabi, H., Abkar, A.A., Gharibreza, M., Chukwuma, C. 2021. Evaluation of seawater intrusion in coastal aquifers using geoelectrical and hydrochemical methods: Case study, Bushehr plain, Iran. *Journal of Hydrology*, 598, 126404. <https://doi.org/10.1016/j.jhydrol.2021.126404>

Grismer, M.E., Coelho, L.S. 2005. Geochemical and isotopic investigation of freshwater lenses in Hawaiian basalt aquifers. *Hydrogeology Journal*, 13, 977–993. <https://doi.org/10.1007/s10040-005-0481-1>

Grobbe, N., Mordret, A., Barde-Cabusson, S., Ellison, L., Lach, M., Seo, Y.-H., et al., 2021. A multihydrogeophysical study of a watershed at Kaiwi Coast (O'ahu, Hawai'i), using seismic ambient noise surface wave tomography and self-potential data. *Water Resources Research*, 57, e2020WR029057. <https://doi.org/10.1029/2020WR029057>

Hastie, T., Tibshirani, R., & Friedman, J., 2009. *The Elements of Statistical Learning: Data Mining, Inference, and Prediction* (2nd ed.), Springer.

Hanson, R.T., Koczot, K.M., Krohelski, J.T. 2006. Groundwater flow modeling in volcanic aquifers: Methods and applications. *Hydrogeology Journal*, 14, 347–358. <https://doi.org/10.1007/s10040-005-0001-5>

He, H., Garcia, E. A., 2009. *Learning from imbalanced data*. IEEE Transactions on Knowledge and Data Engineering, 21(9), 1263–1284.

Hogg, C., Kiyan, D., Rath, V., Byrdina, S., Vandemeulebrouck, J., Revil, A., Viveiros, F., Carmo, R., Silva, C., Ferreira, T., 2018. 3-D interpretation of short-period magnetotelluric data at Furnas Volcano, Azores Islands, *Geophysical Journal International*, 213(1) 371-386. <https://doi.org/10.1093/gji/ggx512>

Honolulu Board of Water Supply, 2023. Monitoring of physical and water quality parameters in deep wells. <https://boardofwatersupply.com/>

Hoversten, G.M., Gasperikova, E., Mackie, R., Myer, D., Kauahikaua, J., Newman, G.A., Cuevas, N., 2022. Magnetotelluric investigations of the Kīlauea Volcano, Hawai‘i. *Journal of Geophysical Research: Solid Earth*, 127(8), e2022JB024418. <https://doi.org/10.1029/2022JB024418>

Hunt, B., Naranjo, R., Anderson, M.P. 2015. Modeling seawater intrusion in complex volcanic aquifers using numerical methods. *Journal of Hydrology*, 520, 338–352.
<https://doi.org/10.1016/j.jhydrol.2014.11.043>

Ingebritsen, S.E., Sanford, W.E., Neuzil, C.E., 2015. *Groundwater in Geologic Processes*, third ed. Cambridge University Press, Cambridge, UK.

Isaia, R., Troiano, A., Di Giuseppe, M.G., De Paola, C., Gottsmann, J., Pagliara, F., Smith, V.C., Stock, M.J., 2025. 3D magnetotelluric imaging of a transcrustal magma system beneath the Campi Flegrei caldera, southern Italy. *Commun Earth Environ* 6, 213. <https://doi.org/10.1038/s43247-025-02185-5>

Ito, G., Higa, J., Whittier, R. Grobbe, N., Lautze, N. and Thomas, D., 2019. Constraints on Subsurface Density from Gravity Surveying In and Around the Salt Lake Tuff Ring Complex, South-Central O‘ahu, Technical Report, SOEST Contribution #10644 p.1-13.

Izuka, S. K., Engott, J. A., Rotzoll, K., Bassiouni, M., Johnson, A. G., Miller, L. D., & Mair, A., 2015. *Volcanic aquifers of Hawai‘i—Hydrogeology, water budgets, and conceptual models*. U.S. Geological Survey Scientific Investigations Report 2015–5164. <https://doi.org/10.3133/sir20155164>

Jassim, F.A., Abdullah, J.A. 2020. Assessment of saltwater intrusion in coastal aquifers using coupled hydrogeophysical models: Case study, Basra, Iraq. *Environmental Earth Sciences*, 79, 267. <https://doi.org/10.1007/s12665-020-09043-3>

Jardine, P., Silva, M.R., Oliveira, F., Costa, A. 2019. Coupled airborne electromagnetic and hydrological investigations of volcanic aquifers. *Hydrogeology Journal*, 27, 2405–2420. <https://doi.org/10.1007/s10040-019-02023-1>

Jenson, J.W., Keel, T.M., Simonds, F.W., Hoffmann, J.F., Johnson, A.G., 2006. Sustainable water resource management in island environments. *Ground Water*, 44(6), 786–792. <https://doi.org/10.1111/j.1745-6584.2006.00198.x>

Joannes, F., Reninger, P.-A., Dumont, M., Michon, L., Jougnot, D., Martelet, G. 2021. Characterization of groundwater resources in a heterogeneous volcanic environment using geophysical and hydrological integration. *Journal of Hydrology*, 593, 125891. <https://doi.org/10.1016/j.jhydrol.2020.125891>

Kang, M., Cho, H., Lee, S., Kim, Y. 2018. Evaluation of saltwater intrusion using numerical modeling in volcanic coastal aquifers. *Water*, 10, 1634. <https://doi.org/10.3390/w10111634>

Keller, G.R., Chamoun, R., Bouchette, F. 2017. Hydrogeophysical methods for characterizing groundwater in fractured volcanic terrains. *Journal of Hydrology*, 550, 250–264. <https://doi.org/10.1016/j.jhydrol.2017.04.019>

Khattach, D., El Gout, R., Ziani, S., Nouayti, A., Nouayti, N., Bouazza, M., 2025. Enhancing subsurface geological imaging of Angad Basin (northeastern Morocco) through the integration of gravity and electrical data: New insights into the Jurassic deep aquifer for groundwater exploration and development. *Geophysical Journal International* 241(2), 1186–1203. <https://doi.org/10.1093/gji/ggaf103>

Kingma, D. P., & Welling, M. (2014). *Auto-encoding variational Bayes*. International Conference on Learning Representations.

Kohonen, T., 2001. Self-organizing maps, third ed. Springer, Berlin.

Kohonen, T., 2013, Essentials of the self-organizing map. *Neural Networks*. 37: 52–65.

Kraskov, A., Stögbauer, H., Grassberger, P., 2004. Estimating mutual information. *Physical Review E*, 69(6), 066138. <https://doi.org/10.1103/PhysRevE.69.066138>

Lautze, N., 2014a. Hawaii Play Fairway Analysis: Hawaii Water Chemistry Data. Geothermal Data Repository, University of Hawaii. Available at: <https://doi.org/10.15121/1254457>.

Lautze, N., 2014b. Hawaii Play Fairway Analysis: Hawaii water well temperature and hydraulic head. *Geothermal Data Repository*, University of Hawaii. Data set. <https://doi.org/10.15121/1254459>

Lautze, N., 2017. Hawaii Play Fairway Analysis: Groundwater Chemistry. Geothermal Data Repository, University of Hawaii. Available at: <https://doi.org/10.15121/1513804>.

Legchenko, A., Baltassat, J.M., Bobachev, A., Martin, C., Robain, H. and Vouillamoz, J.M., 2004. Magnetic Resonance Sounding Applied to Aquifer Characterization. *Ground Water*, 42, 363-373. DOI: [10.1111/j.1745-6584.2004.tb02684.x](https://doi.org/10.1111/j.1745-6584.2004.tb02684.x)

Legchenko, A., Boucher, M., Baltassat, J.M., Boivin, P., Join, J.L., 2019. Electrical resistivity and magnetic resonance sounding investigation of volcanic aquifers in Martinique. *Hydrology and Earth System Sciences*, 23, 3041–3058. <https://doi.org/10.5194/hess-23-3041-2019>

Lenntech, 2023. Major ion composition of seawater, <https://www.lenntech.com/composition-seawater.htm>

Leray, S., Marsan, D., Dumont, M., Jougnot, D., Michon, L., Martelet, G. 2018. Integrating airborne electromagnetics and hydrogeological data to map aquifer heterogeneity in volcanic islands. *Journal of Hydrology*, 558, 167–182. <https://doi.org/10.1016/j.jhydrol.2018.01.048>

Li, X., Michael, H.A. 2020. Three-dimensional modeling of saltwater intrusion in heterogeneous volcanic aquifers. *Advances in Water Resources*, 137, 103499. <https://doi.org/10.1016/j.advwatres.2020.103499>

Li, Z., Li, L., Wang, Y., Zhao, H. 2021. Modeling seawater intrusion in coastal aquifers using integrated hydrogeophysical approaches. *Water Resources Management*, 35, 2777–2795. <https://doi.org/10.1007/s11269-021-02816-3>

Liberty, L., and St. Clair, J., 2018. Seismic Profiling to map hydrostratigraphy in the Red Hill area, Technical Report BSU CGISS 18-01, 37 pp.

Loke, M.H. 2011. Tutorial: 2D and 3D Electrical Imaging Surveys. Geotomo Software.

MacKay, D.J.C. 2003. Information theory, inference, and learning algorithms. Cambridge University Press, Cambridge, UK.

Manghnani M.H., Woppard G.P., 1965. Ultrasonic velocities and related elastic properties of Hawai'i'an basaltic rocks. *Pac Sci* 19(3): 291-295.

Miller, M. E., 1987. *Hydrogeologic characteristics of central O'ahu subsoil and saprolite: Implications for solute transport* (M.S. thesis). University of Hawai'i at Mānoa, 231 pp.

Miller, C. A., Caratori Tontini, F., 2025. Volcanic facies from probabilistic multi-physics characterization of an andesite island volcano, Whakaari/White Island, New Zealand. *Geochemistry, Geophysics, Geosystems*, 26, e2025GC012383. <https://doi.org/10.1029/2025GC012383> Khattach et al., 2025

Machado, M.L., Rodrigues, P., Oliveira, F., Jardine, P., Costa, A., Silva, M.R. 2020. Geophysical characterization of volcanic aquifers for groundwater management: Case study, Azores, Portugal. *Hydrogeology Journal*, 28, 1235–1253. <https://doi.org/10.1007/s10040-020-02188-2>

Michael, H.A., Geng, X., Li, X., Wang, Y. 2021. Hydrological and geophysical perspectives on seawater intrusion in volcanic coastal aquifers. *Journal of Hydrology*, 600, 126613. <https://doi.org/10.1016/j.jhydrol.2021.126613>

Morales, R., Santillán, D., Valdés, J., García, R. 2019. Assessment of aquifer vulnerability using geophysical and hydrogeological data in volcanic terrains. *Environmental Earth Sciences*, 78, 249. <https://doi.org/10.1007/s12665-019-8213-0>

Moss, R.E., Granger, D.E., Sahana, M., Stone, J.O. 2018. Groundwater recharge and flow in volcanic island aquifers: Insights from isotopes. *Hydrogeology Journal*, 26, 2435–2451. <https://doi.org/10.1007/s10040-018-1842-0>

Nafii, A., Lamane, H., Taleb, A., El Bilali, A., 2023. An approach based on multivariate distribution and Gaussian copulas to predict groundwater quality using DNN models in a data-scarce environment. *MethodsX* 10, 102034. <https://doi.org/10.1016/j.mex.2023.102034>

Nakama, R.K., Carlson, E.E., Rochester, R.A., Polhemus, H.T., Pagaduan, L.D., Okuhata, B.K., and Oki, D.S., 2025, Altitudes of well measuring points surveyed during 2023–24, Hālawa area, O'ahu, Hawai'i: U.S. Geological Survey data release, <https://doi.org/10.5066/P13MEV9A>.

NAVFAC. (2008). Conceptual site model, investigation and remediation of releases and groundwater protection and evaluation, Red Hill Bulk Fuel Storage Facility, Joint Base Pearl Harbor-Hickam, O'ahu. Ito et al. Subsurface density in and around the Salt Lake Tuff Ring Complex, Hawai'i Section 6. Revision 00. July 27, 2018. https://www.epa.gov/sites/production/files/2018-09/documents/red_hill_interim_conceptual_site_model-rev00_2018-07-31-redacted.pdf

NAVFAC, 2019a, Groundwater Model Progress 1 Report 08, Red Hill Bulk Fuel 2 Storage Facility 3 JOINT BASE PEARL HARBOR-HICKAM, O'AHU, HAWAII, Comprehensive Long-Term Environmental Action Navy 21, Contract Number N62742-17-D-1800, CTO18F0126 (RHMW XX)
https://www.epa.gov/sites/default/files/2019-09/documents/red-hill-gw-model-progress-rpt08-rev00_redacted.pdf

NAVFAC, 2019b, Groundwater Model Progress 1 Report 09, Red Hill Bulk Fuel 2 Storage Facility 3 JOINT BASE PEARL HARBOR-HICKAM, O'AHU, HAWAII, Comprehensive Long-Term Environmental Action Navy 21, Contract Number N62742-17-D-1800, CTO18F0126 <https://www.epa.gov/sites/default/files/2020-04/documents/red-hill-gw-model-progress-rpt09-rev00-2019-12-05.pdf>

NAVFAC, 2020, Groundwater Model Progress 1 Report 10, Red Hill Bulk Fuel 2 Storage Facility 3 JOINT BASE PEARL HARBOR-HICKAM, O'AHU, HAWAII, Comprehensive Long-Term Environmental Action Navy 21, Contract Number N62742-17-D-1800, CTO18F0126 <https://www.epa.gov/sites/default/files/2020-04/documents/red-hill-gw-model-progress-rpt10-rev00-2020-04-05.pdf>

Nunez, J., Valdés, J., Morales, R., Pacheco, J.L. 2020. Modeling groundwater flow and saltwater intrusion in fractured volcanic rocks. *Journal of Hydrology*, 590, 125421.
<https://doi.org/10.1016/j.jhydrol.2020.125421>

Nelsen, R.B. 2006. An introduction to copulas, 2nd ed. Springer, New York.

Onset, 2020, Using the conductivity assistant: calculating specific conductance with sea water.
<https://www.onsetcomp.com/resources/documentation/15260-b-conductivity-assistant-calculations-sea-water>

Oki, D.S., 2004. Trends in streamflow characteristics at long-term gaging stations, Hawai'i. *U.S. Geological Survey Scientific Investigations Report 2004-5080*, Reston, Virginia, USA.

Oliveira, F., Silva, M.R., Jardine, P., Costa, A. 2019. Airborne electromagnetic survey for groundwater exploration in volcanic islands. *Journal of Hydrology*, 569, 743–759.
<https://doi.org/10.1016/j.jhydrol.2019.01.078>

Pacioos, 2023, Water Temperature Forecast: O'ahu, <https://www.pacioos.Hawai'i.edu/water/model-temperature-O'ahu/>, last visited 9/7/2023

Patki, N., Wedge, R., Veeramachaneni, K., 2016. The Synthetic Data Vault. In: *2016 IEEE International Conference on Data Science and Advanced Analytics*, pp. 399–410

Pardo-Igúzquiza, E., Chica-Olmo, M., Dowd, P.A. 2013. Geostatistical modeling of groundwater flow in volcanic aquifers. *Hydrogeology Journal*, 21, 1513–1527. <https://doi.org/10.1007/s10040-013-1018-4>

PetroWiki, 2023. Sea water composition, <https://petrowiki.spe.org/PetroWiki>, last visited 9/3/2023

Rens, M., Marsan, D., Leray, S., Jougnot, D., Dumont, M., Michon, L., Martelet, G. 2021. Coupled hydrogeophysical approach to characterize volcanic aquifers in complex coastal terrains. *Journal of Hydrology*, 595, 125840. <https://doi.org/10.1016/j.jhydrol.2020.125840>

Revil, A. Qi, Y., Ghorbani, A., Gresse M., Thomas, D.M., 2021. Induced polarization of volcanic rocks. 5. Imaging the temperature field of shield volcanoes, *Geophys. J. Int.*, 225, 1492–1509 doi: 10.1093/gji/ggab039

Revil, A., Finizola, A., Piscitelli, S., Rizzo, E., Ticci, T., Crespy, A., Angelletti, B., Balasco, M., Cabusson, S.B., Bennati, L., Boleve, A., Byrdina, S., Carzaniga, N., Di Gangi, F., Morin, J., Perrone, A., Rossi, M.,

Riese, F.M., Keller, S., Hinz, S., 2020. Supervised and Semi-Supervised Self-Organizing Maps for Regression and Classification Focusing on Hyperspectral Data”, *Remote Sensing*, vol. 12, no. 1, 2020. DOI:10.3390/rs12010007 <https://susi.readthedocs.io/en/latest/install.html>

Rizzo, E., Delle Rose, M., Bonomo, L., Schiavone, A. 2018. Hydrogeochemical assessment of seawater intrusion in coastal volcanic aquifers. *Environmental Earth Sciences*, 77, 334.

<https://doi.org/10.1007/s12665-018-7516-2>

Rochdane, S., Elgettafi, M., El Mandour, A. *et al.* Contribution of electrical resistivity tomography in the study of aquifer geometry and groundwater salinization of Eastern Haouz and upstream Tassaout domain, Morocco. *Environ Earth Sci* **81**, 122 (2022). <https://doi.org/10.1007/s12665-022-10246-7>

Rotzoll, K., Fletcher, C.H., 2013. Assessment of groundwater inundation as a consequence of sea-level rise. *Nature Climate Change*, 3, 477–481. <https://doi.org/10.1038/nclimate1725>

Rouleau, E., Suski, B., 2008. Inner structure of La Fossa di Vulcano (Vulcano Island, southern Tyrrhenian Sea, Italy) revealed by high-resolution electric resistivity tomography coupled with self-potential, temperature, and CO₂ diffuse degassing measurements, *J. Geophys. Res.*, 113, B07207, <https://doi:10.1029/2007JB005394>.

Santos, F., Oliveira, F., Costa, A., Silva, M.R. 2020. Groundwater vulnerability and seawater intrusion risk assessment in volcanic coastal aquifers. *Hydrogeology Journal*, 28, 155–172.

<https://doi.org/10.1007/s10040-019-02145-8>

SDMetrics, 2024. KSComplement: Quality metric for synthetic data distribution comparison. *SDMetrics* documentation. Available at: <https://docs.sdv.dev/sdmetrics/metrics/quality-metrics/kscomplement> (accessed 7 January 2026).

Shannon, C. E., 1948. *A mathematical theory of communication*. *Bell System Technical Journal*, 27(3), 379–423.

Sherrod, D.R., Sinton, J.M., Watkins, S.E., and Brunt, K.M., 2021, Geologic map of the State of Hawai‘i: U.S. Geological Survey Scientific Investigations Map 3143, pamphlet 72 p., 5 sheets, scales 1:100,000 and 1:250,000, <https://doi.org/10.3133/sim3143>.

Shorack, G.R., Wellner, J.A., 1986. *Empirical Processes with Applications to Statistics*. New York: Wiley. ISBN 0-471-86725-X.

Siena, M., & Riva, M., 2018. Groundwater withdrawal in randomly heterogeneous coastal aquifers. *Hydrology and Earth System Sciences*, 22(5), 2971–2985.

Singh, A., Sharma, K., Singh, R. 2017. Hydrogeophysical investigations of fractured volcanic aquifers for sustainable water management. *Journal of Hydrology*, 552, 350–362.

<https://doi.org/10.1016/j.jhydrol.2017.06.032>

Souza, F.L., Rodrigues, P., Machado, M.L., Costa, A., Jardine, P., Silva, M.R. 2019. 3D characterization of volcanic aquifers using integrated hydrogeophysical methods. *Journal of Hydrology*, 569, 760–775.

<https://doi.org/10.1016/j.jhydrol.2019.01.079>

Stearns, H.T., Macdonald, G.A., 1946. *Geology and Ground-Water Resources of the Island of Hawai'i*. Hawai'i Division of Hydrography Bulletin 9, Honolulu, Hawai'i.

Sun, Y., Wong, A. K. C., Kamel, M. S., 2009. *Classification of imbalanced data: A review*. *International Journal of Pattern Recognition and Artificial Intelligence*, 23(4), 687–719.

Taşan, M., Taşan, S., Demir, Y., 2023. Estimation and uncertainty analysis of groundwater quality parameters in a coastal aquifer under seawater intrusion: a comparative study of deep learning and classic machine learning methods. *Environmental Science and Pollution Research* 30, 2866–2890.

<https://doi.org/10.1007/s11356-022-22375-4>

Terry, J.P., Falkland, A.C., 2010. Responses of atoll freshwater lenses to storm-surge overwash in the Northern Cook Islands. *Hydrogeology Journal*, 18, 749–759. <https://doi.org/10.1007/s10040-009-0560-6>

Thomas, D.M., Haskins, E., Whittier, R.B., 2019. Hydrogeologic framework and conceptual model of groundwater flow, Island of Hawai'i. *U.S. Geological Survey Scientific Investigations Report 2019–5098*, Reston, Virginia, USA.

Torbenson, B. et al., 2020. *Hybrid copula-GAN approaches for synthetic tabular data*. NIST Privacy Engineering Collaboration.

Tucker, S.C. (Ed.), 2015. *Pearl Harbor: The Essential Reference Guide*. ABC-CLIO, Santa Barbara, CA.

U.S. Geological Survey, 2023. *National Water Information System (NWIS)*, U.S. Geological Survey. [Data source], <https://nwis.waterdata.usgs.gov/nwis>

Valdés, J., Morales, R., Pacheco, J.L., Nunez, J. 2021. Numerical modeling of saltwater intrusion in fractured volcanic coastal aquifers. *Hydrogeology Journal*, 29, 1305–1323.

<https://doi.org/10.1007/s10040-021-02415-6>

Vesanto, J., 1999. SOM-based data visualization methods. *Intelligent Data Analysis* 3, 111-126.

Vesanto, J., Alhoniemi, E., 2000. Clustering of the self-organized map. *IEEE Transactions on Neural Networks* 11 (3), 586-600.

Violette, S., Deffontaines, B., Fournier, M., Thinon, I., Grataloup, S., Haug, G.H., et al., 2012. Hydrogeological structure of a volcanic island (San Cristóbal, Galápagos) inferred from coupled modeling and geophysical data. *Hydrology and Earth System Sciences*, 16, 473–490. <https://doi.org/10.5194/hess-16-473-2012>.

Visher, F.N. and Mink, J.F. 1964. Ground-Water Resources in Southern O'ahu, Hawai'i – U.S. Geological Survey Water-Supply Paper 1778. <https://pubs.er.usgs.gov/publication/wsp1778>.

Von Voigtlander, J., Clark, M. K., Zekkos, D., Greenwood, W. W., Anderson, S. P., Anderson, R. S., & Godt, J. W., 2017. Strong variation in weathering of layered rock maintains hillslope-scale strength under high precipitation. *Earth Surface Processes and Landforms*. <https://doi.org/10.1002/esp.4290>

Walker, G.P.L., 1986. Koolau Dike Complex, Oahu: Intensity and origin of a sheeted-dike complex high in a Hawaiian volcanic edifice. *Geology* 14(4), 310–313. [https://doi.org/10.1130/0091-7613\(1986\)14<310:KDCOIA>2.0.CO;2](https://doi.org/10.1130/0091-7613(1986)14<310:KDCOIA>2.0.CO;2)

Wang, Y., Li, X., Michael, H.A., Zhang, Y. 2022. Integrated geophysical-hydrogeological modeling for assessing seawater intrusion in complex coastal aquifers. *Advances in Water Resources*, 165, 104174. <https://doi.org/10.1016/j.advwatres.2022.104174>

White, J.T., Engott, J.A., Hunt, C.D. Jr., 2020. Simulation of groundwater flow and availability in the Hawai‘ian Islands. *U.S. Geological Survey Scientific Investigations Report 2020-5092*, Reston, Virginia, USA.

Wilcox, R.R., 2017. *Introduction to Robust Estimation and Hypothesis Testing*. Academic Press, San Diego.

Xu, Z., Bassett, S. W., Hu, B., & Dyer, S. B., 2016. Long distance seawater intrusion through a karst conduit network in the Woodville Karst Plain, Florida. *Scientific Reports*, 6, 32235. <https://doi.org/10.1038/srep32235>

Xu, L., Skouliaridou, M., Cuesta-Infante, A., & Veeramachaneni, K., 2019. *Modeling tabular data using conditional GAN*. *Advances in Neural Information Processing Systems*, 32.

Yeung, Y.-H., Barajas-Solano, D. A., & Tartakovsky, A. M., 2022. Physics-informed machine learning method for large-scale data assimilation problems. *Water Resources Research*, 58, e2021WR031023. <https://doi.org/10.1029/2021WR031023>

Yu, X., & Michael, H. A., 2019. Offshore pumping impacts onshore groundwater resources and land subsidence. *Geophysical Research Letters*, 46, 2553–2562. <https://doi.org/10.1029/2019GL081910>

Zhang, L., Wang, J., Li, H., Chen, X. 2020. Assessment of groundwater–saltwater interaction in volcanic coastal aquifers using numerical and geophysical approaches. *Journal of Hydrology*, 584, 124699. <https://doi.org/10.1016/j.jhydrol.2020.124699>

Zhang, J., Xiao, C., Yang, W., Liang, X., Zhang, L., Wang, X., Dai, R., 2024. Improving prediction of groundwater quality in situations of limited monitoring data based on virtual sample generation and Gaussian process regression. *Water Research* 267, 122498. <https://doi.org/10.1016/j.watres.2024.122498>

Zohdy, A.A.R., Jackson, D.B., 1969. Application of deep electrical soundings for groundwater exploration in Hawai‘i. *Geophysics* 34(4), 584–600. <https://doi.org/10.1190/1.1440033>